Low temperature silicon epitaxy: Defects and electronic properties

Von der Fakultät Informatik, Elektrotechnik und
Informationstechnik der Universität Stuttgart zur Erlangung der
Würde eines Doktor-Ingenieurs (Dr.-Ing.) genehmigte Abhandlung

Vorgelegt von
Thomas A. Wagner
aus Nürnberg

Hauptberichter: Prof. Dr. rer. nat. habil. J. H. Werner

Mitberichter: Prof. Dr. rer. nat. habil. J. Weber

Tag der Einreichung: 29.01.2003

Tag der mündlichen Prüfung: 13.06.2003

Institut für Physikalische Elektronik der Universität Stuttgart

2003

Contents

i

Summary

The present work investigates the electronic properties of thin epitaxial silicon films and their suitability for microelectronic and photovoltaic applications. The films are grown by ion-assisted deposition (IAD), a molecular beam epitaxy (MBE) method that uses a small fraction of accelerated Si^+-ions in the molecular beam, allowing for additional kinetic energy transfer to the substrate during low temperature epitaxy.

This work concentrates on films grown at low deposition temperatures T_{dep} in the range of $T_{dep} = 450°C$ to $750°C$ with deposition rates r_{dep} in the range of $r_{dep} = 0.1$ to 0.5 μm/min. As substrate materials, either monocrystalline (100)-, (111)-, (110)-, and (113)-oriented Si-wafers or block-cast polycrystalline Si-wafers are used.

This work shows that the structural and electronic properties of epitaxial films deposited at low temperatures depend significantly on the substrate orientation. The number of extended defects in (100)-oriented films, i.e. dislocations and stacking faults, is significantly lower than in non-(100)-oriented films. The etch pit density n_{ep}, as deduced by anisotropic defect etching, is below $n_{ep} = 1 \times 10^3$ cm^2 for (100)-oriented films, independent of deposition temperature and rate. This low number of *extended* defects ensures that the electronic properties of (100)-oriented films are dominated by *point defects*.

Photoluminescence and deep level transient spectroscopy (DLTS) serve to characterize defects in the (100)-oriented films. A broad defect luminescence band, located at photon energies around $h\nu = 0.8$ eV, appears in all films deposited at $T_{dep} = 460°C$. When accelerated silicon ions are used to deposit the films, additional defect peaks appear at $h\nu = 0.767$ eV and below. These defects are correlated to thermal donors, that are typically observed in oxygen rich silicon after thermal treatment at $450°C$.

Several broad defect bands in the band gap are identified by DLTS-measurements, the most prominent at trap levels $E_t = 0.2$ eV and 0.25 eV above the valence band.

The defect density is of the order of 1×10^{13} cm^{-3} and shows a minimum for $r_{dep} = 0.3$ μm/min. For deposition temperatures $T_{dep} > 550$°C, no defects are observed with either photoluminescence or DLTS, but the minority carrier diffusion length of the films increases with T_{dep}. The use of the minority carrier diffusion length as a sensitive measure for the density of electrically active defects reveals an exponential decay of the defect density with rising deposition temperature.

Ion-bombardment with Si$^+$-ions during deposition at low temperatures has an important influence on the electronic properties of the films: At $T_{dep} = 460$°C and 650°C, the use of accelerated silicon ions in ion-assisted deposition leads to an increase of the minority carrier diffusion length L for moderate acceleration voltages up to 100 V. At higher deposition temperatures, ion-bombardment did not result in a measurable difference of the electronic properties: Thin film solar cells, deposited at $T_{dep} = 750$°C with and without accelerated silicon ions showed identical conversion efficiencies of 13.8%.

Despite the variety of defects detected in low temperature epitaxial films, Photoluminescence and DLTS did not allow to identify the dominant recombination mechanism that is responsible for the poor photovoltaic properties of the films deposited at $T_{dep} \leq$ 650°C. Therefore, a new lifetime spectroscopy method is developed in this work, that is compatible with thin films and fully processed devices: Temperature dependent quantum efficiency (TQE). Using the TQE method for analysis of thin film solar cells deposited by IAD at $T_{dep} = 460$°C and 510°C revealed the presence of two dominant defect centers, active at different temperatures. Applying a multilevel model for the lifetime to the TQE data allows for the identification of a defect center with an activation energy $E_a = 0.2$ eV as the dominant recombination center at room temperature and a center with $E_a = 0.07$ eV being active at temperatures below 150 K. The TQE results are in good agreement with DLTS experiments, where comparable defect levels are determined in the same films.

Growth on non-(100)-oriented substrates, such as Si(111), Si(110), and Si(113), is dominated by the formation of high densities of extended defects, in particular stacking faults, resulting in significantly lower electronic quality of the films. Light beam induced current investigations of films deposited on polycrystalline substrates with randomly oriented grains show highly differing electronic quality of the grains. As a consequence, this work classifies the suitability of surface orientations for epitaxy according to the result-

ing electronic quality of the deposited films as follows: Type A)(100)-oriented surfaces result in the highest electronic quality. Type B) singular (stable) surfaces (e.g. (111), (110)) result in medium electronic quality. Type C) facetted surfaces result in the poorest structural and electronic quality.

This work gives a detailed analysis of defects in low temperature epitaxial films with their dependence on deposition temperature, deposition rate, and substrate orientation, allowing for a profound judgement of the possibilities and restrictions of low temperature epitaxial films for photovoltaic and microelectronic applications. In most cases, the high number of extended defects and the inferior electronic properties will exclude deposition on non-(100)-oriented substrates. Especially in the case of photovoltaic devices, only epitaxy on (100)-oriented substrates at deposition temperatures above 650°C results in sufficiently high minority carrier diffusion lengths for effective thin film solar cells.

Zusammenfassung

Die vorliegende Arbeit untersucht die elektronischen Eigenschaften von epitaktischen Si-Dünnschichten und deren Eignung für mikroelektronische und photovoltaische Anwendungen. Die Schichten wurden mittels ionenassistierter Deposition (IAD) abgeschieden, eine Molekularstrahl-Epitaxie (MBE) Methode, bei der ein Teil der Si-Atome im Molekularstrahl (ca. 1%) ionisiert wird. Durch eine am Substrat angelegte Spannung ermöglicht der Ionenanteil einen zusätzlichen, exakt kontrollierbaren Energieübertrag auf das Substrat.

Die im Rahmen dieser Arbeit untersuchten Epitaxieschichten wurden bei Depositionstemperaturen T_{dep} im Bereich von $T_{dep} = 450°C$ bis $750°C$ und typischen Abscheideraten r_{dep} im Bereich von $r_{dep} = 0{,}1$ bis $0{,}5$ μm/min abgeschieden. Die Abscheidung erfolgte zum größten Teil auf monokristallinen Si-Substraten mit (100)- , (110)-, (111)-, oder (113)-Orientierung, aber auch Epitaxie auf polykristallinen Block-gegossenen Substraten wurde untersucht.

Die hier vorgestellten Ergebnisse zeigen, dass die strukturellen und elektronischen Eigenschaften der Epitaxieschichten wesentlich von der kristallographischen Orientierung des Substrats abhängen. Die Zahl der ausgedehnten Defekte, d.h. Versetzungen und Stapelfehler, in (100)-orientierten Schichten is deutlich niedriger als in Schichten die auf anderen Substrat-Orientierungen abgeschieden wurden. Die Ätzgrubendichte n_{ep} in (100)-orientierten Schichten, die mittels anisotroper Defektätze ermittelt wird, liegt unter $n_{ep} = 1 \times 10^3$ cm², unabhängig von der Depositionstemperatur und -rate. Diese niedrige Zahl an ausgedehnten Defekten erlaubt die Schlussfolgerung, dass die elektronischen Eigenschaften der (100)-orientierten Epitaxieschichten im wesentlichen von Punktdefekten bestimmt werden.

Photolumineszenz (PL) und *Deep Level Transient Spectroscopy* (DLTS) Messungen

dienen in dieser Arbeit als Methoden zur Charakterisierung von Punktdefekten in (100)-orientierten Schichten. Alle Epitaxieschichten, die bei niedrigen Depositionstemperaturen von $T_{dep} = 460°C$ abgeschieden wurden, zeigen in PL-Messungen ein breites Defektband zentriert um Photonenenergien $h\nu = 0,8$ eV. Bei Verwendung von beschleunigten Si-Ionen während der Abscheidung treten mehrere zusätzliche scharfe PL-Linien unterhalb von $h\nu = 0,767$ eV auf. Diese konnten als thermische Donatoren identifiziert werden, die häufig in Sauerstoffreichen Silizium-Wafern nach einer Temperbehandlung bei Temperaturen um 450°C beobachtet werden.

Mehrere breite Defektbänder in der Bandlücke von Silizium konnten mit DLTS Messungen nachgewiesen werden. Besonders hohe Defektdichten von $N_t \approx 1 \times 10^{13}$ cm^{-3} ergaben sich bei $T_{dep} = 460°C$ und $r_{dep} = 0,3$ μm/min für Defekte im Energiebereich von $E_t - E_V = 0,2$ eV und 0,25 eV. In Epitaxieschichten die bei Temperaturen oberhalb von $T_{dep} = 550°C$ abgeschieden wurden lassen sich keine Punktdefekte mehr mit PL oder DLTS nachweisen. Jedoch steigt die Minoritätsträgerdiffusionslänge L mit zunehmender Depositionstemperatur an. Unter Verwendung von L als Indikator für die Dichte rekombinationsaktiver Defekte, lässt sich ein exponentieller Abfall der Defektdichte mit zunehmender Depositionstemperatur ableiten.

Der Einsatz von Ionen mit moderaten Beschleunigungsspannungen bis zu 100 V während der Abscheidung hat deutlichen Einfluss auf die elektronischen Eigenschaften der Schichten. Bei Depositionstemperaturen von 460°C und 650°C führt der Ionen-Beschuss zu einer Erhöhung der Minoritätsträgerdiffusionslänge. Jedoch konnte bei höheren Depositionstemperaturen von $T_{dep} = 750°C$ kein Einfluss der beschleunigten Ionen auf die Schichtqualität nachgewiesen werden. Dünnschicht-Solarzellen, die bei dieser Temperatur hergestellt wurden erreichen unabhängig vom Ionenbeschuss Wirkungsgrade von 13,8%.

Obwohl eine Vielzahl von Defekten mit PL und DLTS in den Schichten nachgewiesen wurde, konnte der dominierende Rekombinationsmechanismus nicht durch diese Methoden bestimmt werden. Daher wurde in dieser Arbeit mit der *temperaturabhängigen Quantenausbeute* (TQE) eine neue Methode der Lebensdauerspektroskopie entwickelt, die auch auf dünne Halbleiterschichten oder fertig prozessierte Solarzellen angewandt werden kann. Durch die Anpassung eines Models mit mehreren Defektniveaus an gemessene TQE-Daten konnten zwei relativ flache Defekte mit Aktivierungsenergien von $E_a = 0,2$

eV und 0,07 eV als dominierende Rekombinationszentren bei Raumtemperatur und bei 150 K bestimmt werden. Die mit der TQE-Methode ermittelten Aktivierungsenergien sind in guter Übereinstimmung mit Defektniveaus die mittels DLTS an den gleichen Filmen gemessen wurden.

Epitaktisches Wachstum auf Oberflächen mit anderer Orientierung als Si(100), wie Si(111), Si(110) oder Si(113), führt zu einer deutlich höheren Dichte an ausgedehnten Defekten, welche auch die elektronischen Eigenschaften negativ beeinflussen. Ortsaufgelöste Kurzschlussstrommessungen von Solarzellen, die auf polykristallinen Substraten abgeschieden wurden, zeigen stark unterschiedliche elektronische Qualität der einzelnen Körner in Abhängigkeit von deren Oberflächenorientierung. Diese Arbeit klassifiziert daher die Eignung von Oberflächen-Orientierungen für epitaktische Anwendungen anhand der resultierenden elektronischen Qualität der Schicht: Typ A) (100)-orientierte Schichten – höchste elektronische Qualität. Typ B) Singuläre Oberflächen (z. B. Si(111), Si(110)) – mittlere elektronische Qualität. Typ C) Facettierte Oberflächen – niedrigste elektronische Qualität.

Die in dieser Arbeit vorgestellte detaillierte Analyse von Defekten in Niedertemperaturepitaxie-Schichten in Abhängigkeit von Depositionstemperatur, Depositionsrate und Substrat-Orientierung erlaubt eine fundierte Bewertung der Eignung solcher Schichten für mikroelektronische und photovoltaische Anwendungen. Die hohe Dichte an ausgedehnten Defekten und die schlechten elektronischen Eigenschaften der Schichten werden Epitaxie auf nicht-(100)-orientierten Substraten für viele Anwendungen ausschließen. Speziell im Fall von epitaktischen Solarzellen ist nur für Schichten, die auf Si(100) bei Temperaturen oberhalb von 650°C abgeschieden wurden, die Minoritätsträgerdiffusionslänge ausreichend für eine Anwendung in Dünnschichtzellen.

Chapter 1

Introduction

Silicon homoepitaxy at high deposition temperatures $T_{dep} \approx 1000°C$ is widely used in semiconductor industry and provides high quality silicon films for microelectronic and photovoltaic devices [1]. However, many applications such as the formation of abrupt homojunctions or the need to use foreign substrates require a low thermal budget during processing, thus limiting the deposition temperature to a much lower regime.

In the field of microelectronics, the application of low temperatures during epitaxy enables the suppression of thermally activated processes, such as dopant diffusion and segregation. Therefore, precise control of the dopant profiles in the devices, e.g. for opto-electronics [2] and high electron mobility transistors [3], is obtained.

For crystalline silicon solar cells, thin film technologies allow for a significant cost reduction, as only the photovoltaicly active layer, typically several tens of micrometers, is made from crystalline silicon supported by a low cost substrate [4]. However, the application of epitaxy to solar cell mass production requires high electronic quality of the films at high growth rates. Additionally, a low cost substrate, such as glass, sets the upper limit for the deposition temperature to $T_{dep} \approx 650°C$.

The motivation for this work is the concept of fabricating crystalline silicon thin film solar cells by epitaxial thickening of a laser crystallized seed layer on a glass substrate [5]. Despite increasing interest during the last decade in epitaxial thin film silicon cells on low cost substrates, the electronic properties, and consequently the solar cell performance, of

such films remained poor. Therefore, the question arises whether the electronic properties of such films are limited by technological or fundamental physical problems. In order to improve the electronic properties of the films, a profound understanding of the formation of defects in the films under the constraints of low deposition temperatures, high deposition rates, and arbitrarily oriented substrates is necessary.

Although low temperature epitaxy of silicon, and especially of SiGe, has numerous applications in the semiconductor industry, the formation of defects during low temperature epitaxy is not understood in detail. This is mostly due to the fact, that the deposited films for microelectronics are rather thin (below one μm), and direct defect characterization methods are not applicable. The deposition of several micrometer thick silicon films allows the use of direct defect-characterization methods such as photoluminescence, deep level spectroscopy (DLTS), and preferential wet chemical etching.

Ion-assisted deposition (IAD) was developed some ten years ago by Oelting *et al.* [6] in order to provide a method that allows for high deposition rates at low substrate temperatures. Basically a molecular beam epitaxy method, IAD uses a small fraction of accelerated Si ions in the beam, that provide additional energy for film growth at low temperatures, i.e. 650°C and below. The ions are generated by a toroid shaped ionization stage located in between the electron beam evaporator and the substrate. Without activated ionization stage, the deposition conditions in the IAD-reactor correspond to standard MBE-conditions. The ion energy in IAD is controlled in the range of 0 eV to 1000 eV.

This work investigates the formation of defects during Si-deposition by molecular beam epitaxy and ion assisted deposition at low substrate temperatures. In particular the influence of the deposition parameters temperature and rate as well as the influence of ion bombardment during deposition are investigated. In order to identify the dominant recombination centers in the films, the results from defect characterization are compared to the electronic properties of the films. For the application of low temperature epitaxy to polycrystalline substrates the influence of the substrate orientation on the type and density of defects in correlation to the electronic properties is studied.

This work is organized as follows:

Chapter 2 depicts the fundamentals of low temperature deposition and gives a short overview over defects in silicon.

Chapter 3 gives the technical details of the ion-assisted deposition process and describes the applied characterization techniques photoluminescence, DLTS, internal quantum efficiency, defect etching, and light beam induced current.

Chapter 4 gives an insight on the defects formed in (100)-oriented films in dependence of the deposition temperature and rate and the ion-bombardment, using photoluminescence and DLTS. The influence of the defects on the electronic quality of the films is discussed by comparing the results from defect characterization to the minority carrier diffusion length of the films.

Chapter 5 introduces temperature dependent quantum efficiency measurements as a new method for lifetime spectroscopy. This method allows for the determination of the dominant recombination mechanisms in processed thin film solar cells. For that purpose, a simple model for the carrier lifetime is developed, based on a superposition of several defect levels obeying Shockley-Read-Hall statistics.

Chapter 6 shows the investigations of monocrystalline films deposited on (111)-, (110)-, and (113)-oriented substrates. A classification of the suitability of silicon surfaces for low temperature epitaxy, deduced from distribution of the electronic properties in the grains of polycrystalline epitaxial films, is given.

Chapter 2

Fundamentals

2.1 Low temperature silicon epitaxy

2.1.1 Growth techniques

Various deposition techniques are used for epitaxial growth of silicon at low temperatures (here $T_{dep} \leq 650°C$). Based on the underlying physical processes during deposition, they can be divided in four different categories [7]: Chemical vapor deposition (CVD), physical vapor deposition (PVD), liquid phase epitaxy (LPE) [8], and solid phase epitaxy (SPE) [9]. The latter two deposition techniques are not regarded in detail here, as they are only of minor importance at $T_{dep} \leq 650°C$, compared to CVD and MBE processes.

Chemical vapor deposition

The decomposition of a gaseous silicon source, such as SiH_4 or $SiHCl_3$, is the basic principle of all CVD-processes. In the simplest case, this decomposition is achieved by the thermal energy of the substrate. This thermal CVD is a commonly applied technique in semiconductor industry and results in high quality silicon films with acceptable high deposition rates, when high deposition temperatures $T_{dep} \geq 1000°C$ are applied. With decreasing temperature, the deposition rate decreases significantly. Therefore at low temperatures, a wide variety of excitation methods for the decomposition of the gases is in

use, e.g. plasma enhanced CVD (PECVD), hot wire CVD (HWCVD), and electron cyclotron resonance CVD (ECR-CVD). Growth processes in CVD include the formation of precursors, consisting of e.g. SiH_x- or Si-radicals in the case of SiH_4 as source material. Subsequently, these precursors are physisorbed on the surface, followed by a chemisorption of the silicon atom and eventually the evaporation of the remaining hydrogen atoms. However, the surface reactions of the precursors is common to all CVD processes, unless they generate a high amount of Si-radicals, that may be directly physisorbed. This surface reactions are thermally activated by the substrate temperature, and consequently, the deposition rate of CVD-reactions is limited by the substrate temperature. Principles of CVD-deposition are given in Ref. [10], an overview of literature data on deposition rates versus the deposition temperature for various growth techniques is given in Ref. [11].

Physical vapor deposition

In PVD processes, elementary silicon is used for growth. Therefore, the substrate temperature has no influence on the growth rate, which is in PVD only dependent on the rate of silicon atoms or ions that impinge on the substrate surface. Molecular beam epitaxy (MBE), sputter deposition, ion-assisted deposition (IAD), or ion-beam deposition (IBD) are the most important PVD processes. Among these, MBE is the most commonly used. In order to ensure a high mean free path of the particles and to avoid contaminations from the gas phase, ultra high vacuum (UHV) conditions are employed.

A wide range of materials systems are grown epitaxially by MBE, e.g GaAs for optoelectronics and SiGe for heterobipolar transistors. Exact control of the growth process, e.g the formation of shallow junctions, require low temperatures and low growth rates in the range of $1 \ldots 10$ Å/s. In the case of silicon homoepitaxy by MBE, ultra pure polycrystalline silicon is evaporated, commonly by an electron beam. An overview on MBE is given in Ref. [12].

For sputter deposition processes, a Si-target is bombarded with an ion beam, e.g. Ar^+-ions. Silicon atoms and ions are sputtered from the target and reach eventually the substrate. Application of a substrate bias voltage or glow discharge plasma allows for

control over additional deposition parameters, such as the ion energy in sputter processes.

Ion-beam deposition (IBD) uses only Si-ions for film growth. Special ion beam sources allow for a precise control of the ion mass and energy. However, only low deposition rates of the order of 1 Å/s are obtained by IBD due to low effectivity of the sources [13].

Ion-assisted deposition (IAD) is an intermediate method in between MBE and IBD. An additional ionization stage is installed in a MBE-system [6], that allows for the generation of about 1% of Si^+-atoms in the molecular beam. The ions are accelerated towards the substrate by a bias voltage V_{acc} of up to $V_{acc} = 1000$ V. For IAD, high growth rates of up to 133 Å/s $= 0.8$ μm/min are reported [14].

Although in MBE a small fraction of the silicon atoms is ionized by the electron beam, it is not essentially an ion-assisted deposition technique, as generally the substrate is kept at mass potential. Therefore the ions are not accelerated and focused towards the substrate. Nevertheless, if sufficiently high deposition rates and acceleration voltages are applied, there is a significant ion flux to the substrate, that may be used to alter the film properties [15].

2.1.2   Influence of ion-bombardment

In order to tailor the properties of thin films, low-energy bombardment during growth has found wide spread application. The bombardment allows for the alternation of numerous film properties, such as the state of stress, the chemical composition, surface chemical reactions, and the incorporation probability of dopant atoms [16].

The bombardment may influence the nucleation kinetics as well as the film properties during growth. The effects are determined by the materials system of the deposited film and the substrate, the deposition temperature and rate, the mass and energy of the active ions, and the ion-flux.

The principle reactions of accelerated particles with the surface and bulk material are not understood in detail. Monte Carlo simulations [17] and molecular dynamic simulations [18] provide more a qualitative idea of the processes than describe the physical reality. For silicon homoepitaxy, using accelerated Si-ions, the interactions basically may

be discussed according to the ion-energy. Even without additional kinetic energy, a neutral atom bonding to the lattice, releases about 4 eV, depending on the number of bonds made in the condensation step [13]. This condensation energy is transferred to the phononic system of the bulk. A slow Si^+-ion reacts with the surface electrons prior to impact on the surface and introduces its ionization energy of 8 eV to the electronic system. Sputtering processes on the surface, i.e. chemical sputtering (inelastic via excitation of surface atoms) and physical sputtering (elastic, direct recoil) take place once the ion energy exceeds the binding energy of the target atom. In the case of atoms that are not bound to a lattice site with low potential energy, this binding energy might be in the range of only several eV. Subplantation of Si-ions in the bulk starts at ion energies $E_{ion} \approx 8$ eV, the formation of Frenkel-pairs (interstitial – vacancy) at $E_{ion} \approx 20$ eV [19]. Boyd *et al.* assume a linear increase of the density of Frenkel-pairs with the ion energy [20]. Another effect is the increase of the adatom mobility either by chemical sputtering of weakly bound atoms [17], the direct recoil of adatoms [21] or the local excitation of the electronic system due to the interaction of the ions with the lattice.

In literature, most authors report beneficial effects from low energy ion bombardment with ion energies around 20 eV during film growth. Shindo and Ohmi [22] investigated the influence of low energy ion bombardment using Xe and Ar ions during low temperature (T_{dep}= 300°C . . . 350°C) epitaxy in a sputtering system. They found that low energy ($<$ 25 eV), high flux (ratio of ions to atoms $>$ 5), large mass ion bombardment can compensate for lower deposition temperatures with respect to the epitaxial quality of the films. Ion-beam sputter deposition (IBSD) provides a Si-ion growth flux with an average energy of 18 eV [23]. At low deposition temperatures $T_{dep} < 400$°C, IBSD allows for a critical epitaxial thickness up to one order of magnitude higher than in comparable MBE films. For deposition temperatures above 400°C no evidence of ion induced lattice damage was found by transmission electron microscope (TEM) analysis. Also for ion-beam and ion-assisted deposition the optimum ion energy was found in the range of $E_{ion} = 20 \pm 10$ eV [7,13].

Oberbeck [7] provided a model for the beneficial effects of low energy ions in low temperature ion-assisted epitaxy, based on the diffusivity of adatoms and interstitials. Accordingly, the epitaxial growth at deposition temperatures $T_{dep} > 400°$C is dominated by the adatom mobility and for $T_{dep} < 400°$C by the diffusion of interstitials. In the first case, the adatom mobility is increased by the Si$^+$-ions compared to MBE, in the second case the subplantation and the generation of Frenkel-pairs by the ion bombardment enables enhanced diffusion of interstitials to vacancies in the bulk or to the surface.

2.1.3   Growth modes

Atoms impinging on the substrate surface are adsorbed and then they migrate on the surface as so called adatoms (or addimers). At substrate temperatures $T_{dep} \leq 800°$C no desorption of the adatoms occurs, i.e. the sticking probability is close to one and all atoms remain on the substrate [24]. Incorporation of the adatoms occurs at kinks in step edges due to the high coordination of these sites. In physical vapor deposition processes, growth is dominated by the adatom mobility and the deposition rate, i.e. the number of atoms impinging on the surface per time unit. These two factors determine the mean free path time of the adatom before it reaches either a surface step, where it is attached and migrate to a kink, or collides with other adatoms and forms a cluster which may result in the nucleation of a new terrace on the surface. A simplified model of the behavior of adatoms at step edges is given in figure 2.1. The potential energy of the adatoms determines the migration and incorporation probabilities. The most favorable site for incorporation of an adatom on the lower terrace is a kink in the step edge. Here the potential energy shows a minimum, as the atom has the most neighbors satisfying dangling bonds. For an adatom on the upper terrace, the step edge might form a so called positive Schwoebel barrier [25]. If the kinetic energy of the adatom is lower than the barrier height, the atom will be reflected and the motion down the step is impeded. It is noted, that the incorporation probability and the existence of a Schwoebel barrier depend on the substrate orientation and the surface reconstruction (see also chapter 2.3).

At low deposition temperatures three different growth modes are distinguished in
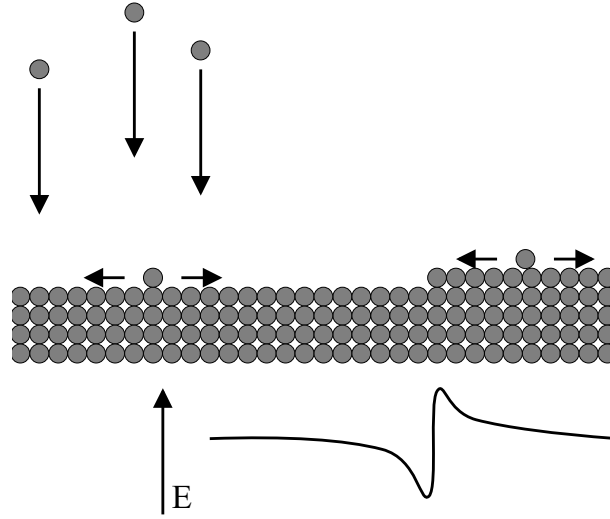
Figure 2.1: At deposition temperatures $T_{dep} \leq 800°C$ all impinging Si-atoms are adsorbed on the surface. Due to miscut, the surfaces consist of terraces and steps. The motion and incorporation of the adatoms is determined by the potential energy of the adatom, as illustrated in the lower half of the picture. At step edges, a minimum of the potential energy is found. The most favorable site for incorporation of the adatom in the crystal-lattice is then a kink in the step edge. However, adatoms migrating on the upper terrace and reaching the step might see a so called Schwoebel barrier. If the kinetic energy of the adatom is lower than the barrier height, the atom will be reflected and the motion down the step is impeded.

homoepitaxial growth as illustrated in figure 2.2 [26]: i) *island growth* at very low temperatures up to $T_{dep} \approx 150°C$, ii) *layer by layer growth* in the range of $T_{dep} \approx 150°C$ to $T_{dep} \approx 450°C$, and *step flow growth* for deposition temperatures above $T_{dep} \approx 450°C$. Note, that these temperatures may vary with the type of growth technique, the deposition rate and the materials system.

In *random or island growth mode*, the substrate temperature, and therefore the adatom mobility, is so low, that the probability of clustering of adatoms is significantly higher than for the incorporation at a step edge. In consequence, a high number of islands form on the surface, which coalesce during progressing growth. Nevertheless, new islands are formed
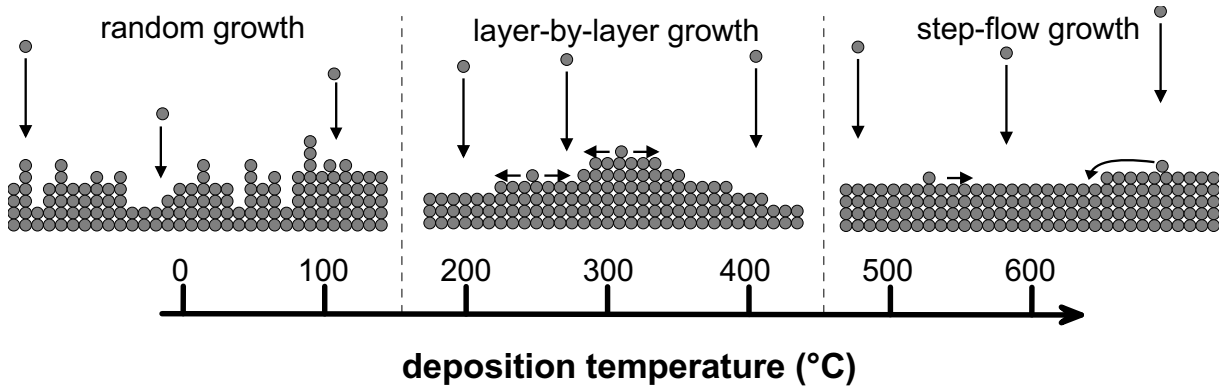
Figure 2.2: Growth modes at low temperatures [26].

on top while coalescence of the lower layer is incomplete, resulting in high densities of point defects and surface roughening.

Once the adatom mobility is high enough that the adatoms can migrate on the surface, *layer by layer growth* mode is reached. Incorporation of adatoms in this mode occurs mostly at step edges. However, if the mean free path of the adatoms is significantly lower than the step distance (terrace width), new terraces nucleate by collision of adatoms. If a Schwoebel barrier at surface steps exist, surface roughening is enhanced, as adatoms on a terrace may not fill up vacant places at lower atomic layers due to the barrier.

In *step flow growth* mode, the mobility of the adatoms is so high, that nucleation takes place on the surface and growth only occurs at step edges. I.e. one monolayer is filled up before the next terrace is formed. However, surface roughening due to kinetically limited growth conditions is also observed in the temperature range of $T_{dep} = 450...625°C$ for deposition on Si(100)-substrates with miscut angles of $0.2...4°$ [27].

2.1.4   Limited epitaxial thickness

The growth modes discussed in the previous chapter have an important consequence for the maximum epitaxial thickness of the films. In principle, epitaxial growth is possible even at very low deposition temperatures down to room temperature [28]. However, at low deposition temperatures, the maximum thickness of the epitaxial films is limited.

Jorke *et al.* [29] and Eaglesham *et al.* [30] showed the existence of a critical epitaxial thickness h_{epi} in MBE-epitaxy, beyond which the growth mode turns from crystalline to amorphous. This effect sets a fundamental limit to the thickness of epitaxial films grown at low temperatures, and has been shown to exist for ECR-CVD [31], ion-beam sputter deposition (IBS) [32] and MBE methods [33–37]. The effective h_{epi} depends on the materials system, the deposition method, and the deposition conditions. After Eaglesham [30], the critical epitaxial thickness h_{epi} has an exponential dependence on the deposition temperature and is given by

$$h_{epi} = h_0 \exp(-E_{act}/k_B T_{dep}), \tag{2.1}$$

where h_0 is a prefactor that depends on the deposition rate and E_{act} is the activation energy. For the homoepitaxy of Si on Si(100) substrates, an activation energy of 0.45 ± 0.10 eV is found.

The critical epitaxial thickness and the activation energy strongly depends on the substrate orientation [7]. Figure 2.3 shows the dependence of the critical epitaxial thickness on the deposition temperature for thin films deposited on Si(100), Si(113), Si(110), and Si(111) by ion assisted deposition [38]. Analysis of the slope in Arrhenius representation reveals activation energies of 0.6 eV, 1.2 eV, 1.4 eV and 2.1 eV for deposition on Si(001), Si(011), Si(111) and Si(113) respectively. Also, the transition temperature from limited epitaxial growth to unlimited epitaxy depends on the substrate orientation. For deposition on Si(100), this temperature is in the range of $T_{dep} = 390\ldots420°C$, whereas for deposition on Si(110), Si(113), and Si(111) this transition occurs at temperatures $T_{dep} \leq 450°C$.

Platen et al. demonstrated low temperature epitaxy using electron cyclotron resonance chemical vapor deposition at temperatures of $325°C$ [39]. They also found a limited epitaxial thickness with $h_{epi}(100) > (311) > (111) > (110)$.

Several models are proposed in the literature to explain the limited epitaxial thickness. Jorke *et al.* explained the effect by a temperature dependent accumulation of defects in the films [29], although this model does not predict the observed Arrhenius temperature dependence. Thiesen *et al.* suggested a model based on the segregation of impurities, mainly hydrogen, on the surface [40]. This model reproduces the exponential temperature
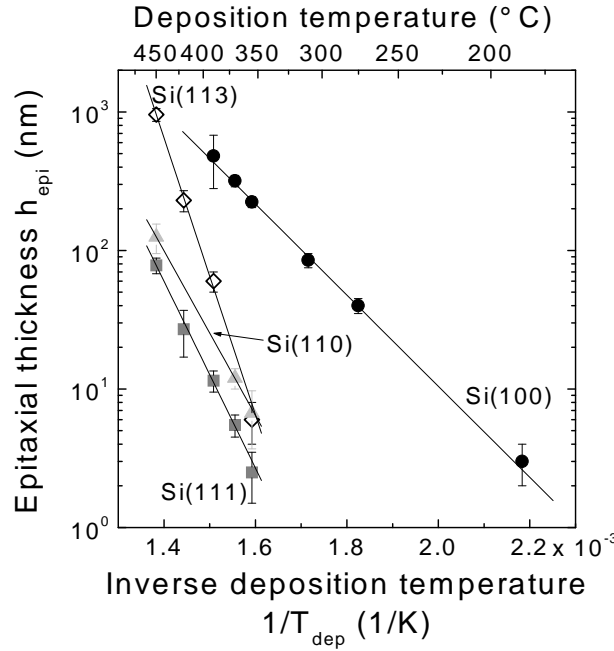
Figure 2.3: The exponential dependence of the epitaxial thickness on the deposition temperature unveils activation energies of 0.6 eV, 1.2 eV, 1.4 eV and 2.1 eV for deposition on Si(001), Si(011), Si(111) and Si(113) respectively.

dependence, however, there is no evidence for the presence of the high amounts of hydrogen necessary for the breakdown of epitaxy in MBE or IAD. Additionally, the activation energy of 0.48 eV for the diffusion of hydrogen in silicon [41] is only for deposition on Si(100) in the range of the activation energy of 0.6 eV for the limited epitaxial thickness. The activation energy for deposition on Si(110), Si(113), and Si(111) are significantly higher and therefore, hydrogen diffusion is very unlikely to be the limiting factor for those substrate orientations.

The most probable explanation is a kinetic surface roughening due to limited adatom mobility and step diffusion barriers, as proposed by Eaglesham [33]. The transition from defect free epitaxial growth to amorphous or nanocrystalline growth occurs via a phase of surface roughening. Subsequently {111}-facets are formed, followed by the nucleation of stacking faults and twin lamellae on the {111}-planes [38,42]. This behavior is illustrated in figure 2.4 for the deposition on Si(100) at $T_{dep} = 270°C$ by IAD, but similar results are
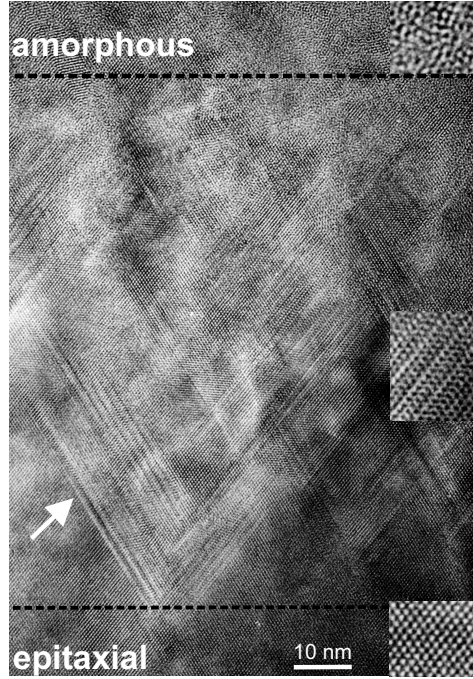
Figure 2.4: High resolution transmission electron micrograph (cross section) of a IAD-film deposited at $T_{dep} = 270°C$ in [110]-projection. The transition from epitaxial defect free growth to amorphous growth occurs via a {111}-facetting and subsequent formation of high densities of stacking faults (white arrow). The small inserts on the right show details of the three sections. [38]

found for other substrate orientations. The activation energies for the limited epitaxial thickness are in good agreement with literature data of the activation energy of adatom mobility on Si(100), Si(110), and Si(111) surfaces (no literature data of the activation energy for adatom diffusion on Si(113) is published). The existence of positive Schwoebel-barriers [25] at step edges may enhance the surface roughening, as adatoms can not diffuse down a step at low adatom energy due to this barrier. The formation of stacking faults then occurs on {111}-planes, once the surface is facetted. Therefore, the limiting factor for epitaxy at low temperatures is the surface adatom mobility.

2.2   Structural defects in silicon

Defects in semiconductors may be classified according to their dimension: Point defects are *zero dimensional* defects. The most simple examples of this class are self-interstitials and vacancies. Also impurity-atoms on interstitial and substitutional sites and small complexes of impurities, sometimes in conjunction with interstitials or vacancies are denoted as point defects. Dislocations, are *one-dimensional* defects, while stacking faults, twins, and grain boundaries are *two-dimensional* defects. Precipitates of impurity atoms may form *three dimensional* defects in semiconductor materials.

In general, a high number of structural defects changes the electronic and optical properties of semiconductors. Obviously, the introduction of dopant impurities has a major influence on the conductivity. Also, the incorporation of rare earth metals in silicon is used to enable optical emissions of the otherwise indirect and therefore ineffective optical semiconductor [43]. However, most of the defects present in silicon are detrimental to the performance of devices, and huge efforts have been and are undertaken in order to minimize defects in crystal growth and device processing. The research on defects in silicon, as well as on defect engineering for silicon devices has resulted in a vast number of publications. However, there is still a high number of ongoing research projects on defects, as a complete understanding of the microscopic structure and interactions of defects is still lacking. In the following a brief presentation of the literature data on defects in bulk and thin film silicon is given, that is of importance for the analysis and discussion of defects in low temperature epitaxial films.

2.2.1   Extended defects

Dislocations and stacking faults are the two most important types of extended defects in epitaxial films [44]. There are two main dislocation types [45]: (i) edge dislocations and (ii) screw dislocations. In epitaxial films, dislocations are generated in several ways. Any distortion of the surface structure, e.g. particles or moulds on the substrate surface, may result in the formation of dislocations when these structures are overgrown. Also, if there is a mismatch in the lattice constants of the substrate and the epitaxial film, the resulting

stress is reduced by the formation of dislocations [46]. And finally, any dislocation that is present in the substrate will be continued in the epitaxial film.

At dislocations, the distorted lattice structure represents a preferred gettering site for impurities. Dislocation core states (dangling bonds), as well as decoration of dislocations with impurities might result in electronic defect levels in the band gap with a high recombination activity [47] (see also chapter 2.2.2).

Stacking faults represent an irregularity in the stacking sequence of the crystal lattice. No broken bonds remain at stacking faults, except for the partial dislocations bordering the stacking fault. Nevertheless, stacking faults might be associated to shallow electronic levels in the band gap [48,49]. For epitaxial growth, the formation of stacking faults has an enormous impact on the crystalline quality, as it is pointed out in chapter 2.1.4.

2.2.2 Optically active defects

In principle, a perfect, clean, direct band gap semiconductor should not emit any luminescence except light corresponding to the band gap energy [50]. At low temperatures excess electrons and holes, generated by an external excitation, form excitons which give rise to luminescence slightly below the band gap energy. In the case of an indirect semiconductor, recombination requires the participation of a phonon. The resulting photon energy is therefore reduced by the phonon energy, leading to a broad spectrum of free exciton luminescence typical for a specific semiconductor (intrinsic luminescence). If the semiconductor is not clean or perfect, free carriers can be captured by acceptors, donators, or other impurities and defects [51]. Radiative decay of excitons captured in traps gives rise to impurity or defect specific luminescence features [52]. Figure 2.5 shows a typical PL spectrum of low phosphorus doped (1×10^{15} cm^{-3}) Czochralski-grown silicon (CZ-Si) that exhibits lines corresponding to the phonon assisted extrinsic and intrinsic recombination radiation bands as reported in literature [51]. All of the observable peaks are identified with lines from intrinsic or phosphorus doped silicon within a deviation of $\Delta h\nu = 0.001$ eV. It should be noted, that photoluminescence in general is not a quantitative technique because of the competition of radiative and non radiative recombination mechanisms.
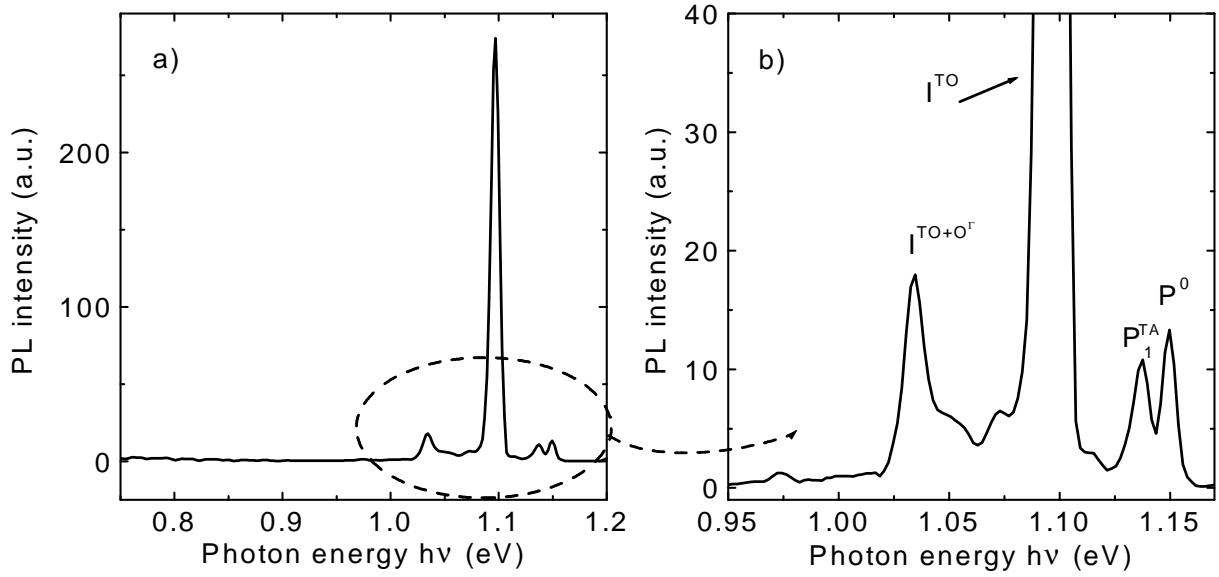
Figure 2.5: Photoluminescence spectrum of low phosphorus doped $(1 \times 10^{15} \ cm^{-3})$ CZ-silicon, recorded at $T_{PL} = 12$ K, an excitation power of ≈ 3 W/cm^2, and a slit-width of 1 mm. a) The observed peaks above 1.0 eV correspond to the phonon-assisted recombination of free or bound excitons. b) Identification of the phonons involved for the main PL lines: I^{TO} - intrinsic transversal optical, $I^{TO+O^{\Gamma}}$ - intrinsic TO + Brillouin zone center phonon, P^0 and P_1^{TA} - phosphorus related recombination (after [51]).

Defect free intrinsic and doped silicon

A study of intrinsic and doped silicon PL features was published in [51]: The main intrinsic lines are at 1.097, 1.032, 1.137, and 1.074 eV, with an intensity ratio of 1 : 0.07 : 0.035 : 0.016. These lines correspond to the phonons participating in the recombination process, in particular the transversal acoustical (TA) at 18.4 meV, the transversal optical (TO) at 58.0 meV and the zone center phonon O^{Γ} at 64.4 meV [53]. If silicon is doped with either phosphorus or boron, the main lines are found at 1.092 and 1.150 eV in the case of P, and 1.092, 1.132, and 1.028 eV for B. In defect free intrinsic, and phosphorus- and boron-doped silicon, no PL lines are observed below 0.968 eV, and therefore any luminescence at lower energies may be attributed to defects or impurities. This part of a PL-spectrum

further on will be referred to as defect-luminescence, while the luminescence above 0.968 eV will be assigned as band-to-band-luminescence (BtB-luminescence).

Upon doping of Si with either boron or phosphorus the sharp bound exciton spectra smear out to broad peaks associated with excitons bound to multiple acceptors or donators for doping densities greater than $1 \times 10^{17} \mathrm{cm}^{-3}$ [54]. Sauer [55] described a broadening of the lines upon higher doping levels in boron as well as in phosphorus doped silicon. As explanation this author offered either the formation of electron hole droplets (EHD) or bound multiple-exciton complexes. The EHD gives rise to luminescence around 1.086 eV, but is only observed when the excitation intensity is above a certain threshold [56]. The intensity of the peak then increases linearly with the excitation power.

Dislocation-related PL

Bound exciton states at dislocations can originate either from dislocation bonds, impurities, or defects in dislocation cores, from impurity clouds and intrinsic point defects in the vicinity of the dislocations or from long range strain fields of dislocations [47,57].

Recombination radiation connected with dislocations in silicon has been observed for the first time by Drozdov et al. [58]. At T=4.2 K, the dislocation radiation corresponds to a series of lines with energies of 0.812, 0.875, 0.934, and 1.000 eV at the maxima. These are the so called D-lines, enumerated D1 to D4, respectively.

D-line luminescence has been identified with dislocations in plastically deformed bulk silicon by Sauer et al. [59]. However, no PL-intensity is observed from undecorated dislocations [60,61].

Photoluminescence after implantation and irradiation

Broad luminescence bands in the range between 0.8 and 1.05 eV were observed by Weman et al. in boron doped silicon after reactive-ion etching (RIE) and plasma etching using deuterium [62]. After RIE treatment they observed a band peaking at 0.9 eV and related this band to extended defects caused by the dry etching process. They also carried out an additional plasma hydrogenation treatment, that resulted in broad peaks around 0.92,

0.94, and 0.96 eV, and a weak structure centered around 0.85 eV.

A set of five photoluminescence lines (0.772 ... 0.745 eV) formed through nitrogen-carbon interactions has been studied by Dörnen et al. [63]. Samples have been implanted with N, N plus C, Ar, and C at doses of 5×10^{14} cm^{-2}.

In CZ-Si, a prominent PL spectrum arises after irradiation by high energy electrons (1.5 – 2.0 MeV). The defect at 0.79 eV, also known as C-line, is associated with the presence of oxygen and carbon in the samples [64]. This defect possesses several phonon replicas at photon energies of 0.771, 0.747, 0.730, 0.724, and 0.717 eV [65].

Another defect line, the so called P-line, is very similar in energetic position and local mode energies to the C-line and also associated to the presence of oxygen in silicon [66–68]. Further, the authors of [66] noted, that P-line luminescence was observed in irradiated CZ-Si. The center of the P-line is at 0.767 eV, and phonon replicas are found at 0.749, 0.724, and 0.705 eV [69]. Additionally, a luminescence line at 0.926 eV, labeled H-line, is directly correlated in intensity with the P-line [66,68].

The so-called G-line (0.97 eV) has been observed in electron and neutron irradiated float zone material and is associated with carbon in the bulk [68,70].

The C, P, and H-lines are only observed in CZ-Si after a thermal treatment at 450°C and are closely related to the thermal donor concentration. Thermal treatment below 400°C and above 500°C results in significant lower H and P-line luminescence and thermal donor concentration [68].

Other defect centers at 1.018 eV [71] (labeled W) and 1.040 eV [71,72] (labeled X) are created by radiation damage, especially by bombardment with neutrons or ions [52].

In lithium-doped silicon, the so called Q and S-lines at 1.045 eV and 1.082 eV are observed after irradiation with 2 MeV electron irradiation [73]. The intensity of the S-line depends on the carbon concentration. The Q-lines are around 1.045 eV and the S-lines around 1.082, although reported S-lines also include higher energies (1.108, 1.105, 1.101, 1.093, 1.091, 1.088, 1.086, 1.070 eV).

Photoluminescence from epitaxial films

Lightowlers *et al.* studied films from molecular beam epitaxy deposited at temperatures below 800°C by means of photoluminescence [74,75]. They observed very broad luminescence around the D-lines, especially around 0.8 eV, which they termed a continuum underlying the D-line luminescence. The dislocation density in this case was 1×10^4 cm^{-2}. They also mentioned a defect complex of N-Al that gives rise to the so called A-line at 1.12235 eV.

Epitaxial films deposited by MBE at 500°C, doped with As by ion-beam doping yields material with high point defect densities, while at higher deposition temperatures $T_{dep} > 650$°C no defects in the band gap were observed [76]. The ion energy in this experiment was in the range of 500 eV. The authors did not observe the D-lines associated with dislocations and therefore assigned a broad background PL below 0.89 eV to point defects caused by low adatom mobility at low growth temperatures. They also performed DLTS measurements and discovered two deep level electron traps at 0.51 and 0.06 eV below the conduction band at a level around 10^{14} cm^{-3} in films grown at 500°C.

Ni et al. [77] showed that broad sub band gap photoluminescence is observed, if an acceleration voltage of -1000 V is applied to the substrate during low temperature MBE at $T_{dep} = 420$°C. A similar effect was observed with floating substrate bias. Only with 0 V bias no sub band gap photoluminescence was detected.

Noël et al. investigated MBE silicon doped by B$^+$-ions during growth [54]. They observed at low deposition temperatures $T_{dep} = 500$°C a peak at 1.040 eV, that they labeled I3 and related it to the defects observed in [78] from irradiation defects. However, they even observed a small signature of I3 in undoped samples and concluded, that the adatom mobility is too low at 500°C to obtain defect free growth, and the I3 is a result of point defects or point defect complexes.

Robbins et al. reported about PL from MBE films deposited at 850°C. They observed mainly FE and BE (free and bound excitons) luminescence, but also the G-line at 0.97 eV after irradiating the samples with 20 keV electrons, which they attributed to a carbon-complex being present in the films due to a graphite susceptor [79]. This complex anneals

at 300°C. They also reported increased electron hole droplets at around 1.081 eV upon increasing laser power from 40 to 150 mW.

A broad PL peak around 0.8 eV is observed in SiGe and pure silicon films deposited on a strained Si-buffer layer at $T_{dep} = 800$°C by low pressure chemical vapor deposition (LPCVD) [80]. The strain in the buffer layer results from a mesa-structure of the substrate, formed for the growth of self-ordered Ge-islands.

Table 2.1 gives a comprehensive summary of defect lines identified in silicon.

2.2.3   Deep level defects

Thermal donors

Thermal donors (TD) are created in oxygen rich silicon, e.g. CZ-Si in contrast to FZ-Si, upon heat treatment in the range from 300°C to 500°C [84], resulting in increased conductivity due to the formation of donor-type states in the band gap. The formation rate has a maximum at about 450°C [85]. The maximum concentration of the TDs at 450°C is proportional to the third power of the interstitial oxygen concentration [86]. The thermal donors are states in the band gap that arise from different types of oxygen-aggregates. At least 16 different species of thermal donors with energy levels in the range of E_C- 0.07 eV and E_C- 0.15 eV have been reported [87,88]. It has been shown, that thermal donors are passivated by hydrogen [89,90]. The formation kinetics and the microscopic model are still under discussion [91] and are summarized by Wada [92]. Some models see the core of the defect to consist of chains of oxygen interstitials aligned along the <110> direction, while some other models relate the TDs to silicon self interstitials formed through oxygen dimers [84].

So called "new oxygen donors" appear in CZ-silicon after long heat treatments in the temperature range from 650°C to 800°C [93]. The defects are associated with SiO_x-precipitates and show a broad defect distribution in the upper half of the band gap. Additionally, a sharp PL peak at 0.903 eV is detected.

Table 2.1: *Photoluminescence lines from radiative recombination centers in silicon and their origin or identification.*

main line	phonon replica	name	identification	reference
	energy $h\nu$ (eV)			
0.812		D1		[58,59]
0.875		D2		
0.934		D3	dislocations, decorated	
1.000		D4		
0.745	0.758, 0.761, 0.767, and 0.772	N	nitrogen-carbon interaction	[63]
0.767	0.749, 0.724, and 0.705 eV	P	oxygen-rich silicon, after heat treatment	[66,67,69]
0.926		H	oxygen-rich silicon, after heat treatment	[66,68]
0.79		C	carbon and oxygen related, after irradiation	[64,65]
0.97		G	carbon related, after irradiation	[68,70]
1.040		I3	after ion or neutron irradiation and annealing	[72]
1.045		Q	lithium-doped Si, after	[73]
1.082		S	2 MeV electron irradiation	
1.122		A	isoelectronic trap, carbon, Al-doping	[75,81]
broad peak around 0.8		0.8-peak	strain in the bulk	[80,82,83]

Interstitial defects

Silicon containing oxygen, carbon, and Group III or Group V impurities shows a wide spectrum of defect states associated with interstitial and substitutional complexes of these impurities. The formation and reactions of these complexes depend on the temperature treatment and the impurity concentration [94]. Most of these defect reactions take place in the annealing temperature range of $T \leq 400°C$. Only the B_iB_s (i = interstitial, s = substitutional) complex is stable above $T = 400°C$, which shows a hole trap at $E_t = 0.30$ eV, as determined by DLTS.

Metallic impurities

Among the metallic impurities, the transition metals are the most intensively studied due to their importance for semiconductor device fabrication. Metallic impurities in silicon may form interstitial or substitutional point defects, complexes with silicon or other impurities, precipitate or agglomerate at lattice imperfections. Transition metals such as Cu, Co, and Ni have high solubility and diffusivity in silicon, even at room temperature. A review for Cu, Co, and Ni in silicon is given in [95], including a variety of defect levels in the band gap reported after indiffusion of the metals. Almost 20 energy levels in the band gap of silicon are associated with iron [96]. In epitaxial thin films, metallic impurities such as Ni, Fe, and Cr can arrive form the chamber walls or components such as thermocouples. Copper may be introduced by unintentional sputtering from the crucible or the water cooling tubes. These metals have a highly detrimental influence on the device performance of solar cells [95] and microelectronics, and therefore great effort is put into avoiding metallic contamination during device processing [97].

2.2.4 Recombination mechanisms

In semiconductors, there is a steady thermal excitation or *generation* of carriers, i. e. an electron is lifted to the conduction band and leaves a hole in the valence band [98]. This process is expressed by the thermal generation rate G_0. The opposing process, the *recombination* of these carriers, is described by the equilibrium recombination rate U_0. In

order to maintain thermodynamic equilibrium, it holds that

$$U_0 = G_0, \tag{2.2}$$

and the equilibrium concentration of electrons and holes at a certain temperature is given by [99]

$$n_0 = N_C \exp(-\frac{E_C - E_F}{kT}) \tag{2.3}$$

$$p_0 = N_V \exp(-\frac{E_F - E_V}{kT}) \tag{2.4}$$

with the effective density of states for the conduction band N_C and the valence band N_V. The values of n_0 and p_0 are connected via the Fermi level and therefore not independent: The product of both amounts to the square of the intrinsic carrier concentration $n_0 p_0 = n_i^2$.

The thermal generation rate G_0 depends on the absorption properties of the semiconductor, in particular on the band gap energy E_g, whereas the equilibrium recombination rate R_0 is proportional to the carrier concentrations

$$R_0 = B n_0 p_0, \tag{2.5}$$

with the material dependent radiative recombination constant B. In the case of crystalline silicon, an indirect semiconductor, B has a rather small value of 1×10^{-14} cm^3/s, [100] in contrast to direct semiconductors which have a higher radiative recombination constant, e. g. B (GaAs) $= 3 \times 10^{-10}$ cm^3/s [101]

Any perturbation of the thermal equilibrium of a semiconductor, such as illumination with photon energies above E_g, results in generation of excess carriers, i. e. $np \geq n_i^2$ with a generation rate G. These excess carriers recombine via three basic recombination mechanisms: (i) radiative recombination, (ii) Auger recombination, and (iii) recombination via defects as described by the Shockley Read Hall statistics (SRH) [102,103]. Under steady state conditions, i. e. the generation rate is constant, it holds that the net recombination rate U is given by

$$U = G. \tag{2.6}$$

The net recombination rate is the total recombination minus the equilibrium recombination rate U_0, and it follows that $U = 0$ for $\Delta n = n - n_0 = 0$.

In the following the net recombination rate will be given for the basic recombination processes in the case of negligible electric fields, the absence of carrier traps, and under the condition of equal excess carrier concentrations: $\Delta n = \Delta p$. The carrier lifetime τ is then given by

$$\tau = \frac{\Delta n}{U}. \tag{2.7}$$

After termination of the generation, the thermodynamic equilibrium is restored by a characteristic decay of excess carriers $\Delta n(t)$, described by

$$\frac{d\Delta n(t)}{dt} = -U(\Delta n(t)). \tag{2.8}$$

In general the net recombination rate depends on the doping level of the semiconductor (n_0, p_0), and the injection level Δn.

Radiative recombination

Radiative recombination is the inverse process to the absorption of light. An electron and a hole recombine under emission of a photon, in general with an energy corresponding to the band gap. This fundamental recombination process is unavoidable, even in the most perfect and clean semiconductor. As an electron and a hole are required for the recombination process, the net rate of radiative recombination U_{rad} is proportional to the number of electrons and holes

$$U_{rad} = B(np - n_0 p_0), \tag{2.9}$$

and with $n = n_0 + \Delta n$, $p = p_0 + \Delta p$, and charge neutrality $\Delta n = \Delta p$ it follows that

$$U_{rad} = B(n_0 + p_0)\Delta n + B(\Delta n)^2. \tag{2.10}$$

According to equation 2.7, the radiative lifetime τ_{rad} is given by

$$\tau_{rad} = \frac{1}{B(n_0 + p_0) + B\Delta n}. \tag{2.11}$$

In the limit of low injection levels $\Delta n \ll n_0 + p_0$, τ_{rad} is injection independent and inversely proportional to the doping concentration $(n_0 + p_0)$

$$\tau_{rad} = \frac{1}{B(n_0 + p_0)}. \tag{2.12}$$

In the limit of high injection $\Delta n \gg n_0 + p_0$ the doping concentration is negligible and τ_{rad} is inversely proportional to Δn

$$\tau_{rad} = \frac{1}{B\Delta n}. \tag{2.13}$$

In a direct band gap semiconductor with no defects, radiative recombination is the dominant recombination mechanism at low doping levels.

Auger recombination

Auger recombination describes the recombination process of an electron with a hole, whereby the excess energy is transferred to a third carrier, i.e. an electron or a hole. However, this recombination becomes only important for high dopant concentrations. The net Auger recombination rate U_{Aug} can be calculated by

$$U_{Aug} = C_n(n^2 p - n_0^2 p_0) + C_p(np^2 - n_0 p_0^2), \tag{2.14}$$

with the Auger coefficients C_n and C_p, which are insensitive to dopant concentration. The Auger coefficients of Si are measured to $C_n = 2.8 \times 10^{-31}$ cm^{6}s^{-1} and $C_p = 1 \times 10^{-31}$ cm^{6}s^{-1} [104,105]. The Auger recombination lifetime τ_{Aug} for n- and p-type material can be deduced from equation 2.7 using $\Delta n = \Delta p$:

$$\tau_{Aug} = \frac{1}{C_n n^2 + C_p n\Delta n} \qquad \text{for n-type} \tag{2.15}$$

$$\tau_{Aug} = \frac{1}{C_p p^2 + C_n p\Delta n} \qquad \text{for p-type} \tag{2.16}$$

For the two limiting cases of high and low injection these equations can be simplified: At low injection levels $\Delta n \ll n_0 + p_0$ it holds that $n = n_0$ and equation 2.15 becomes

$$\tau_{Aug} = \frac{1}{C_n n_0^2} \qquad \text{for n-type} \tag{2.17}$$

(for p-type respectively) and therefore only depends on the dopant level via n_0. Under high injection conditions τ_{Aug} becomes injection dependent and can be written as

$$\tau_{Aug} = \frac{1}{(C_n + C_p)(\Delta n)^2}. \tag{2.18}$$

At low doping levels below $N_{D/A} \approx 1 \times 10^{18}$ cm^{-3}, Coulombic interactions must be taken into account, which enhance the probability for band to band Auger recombination. This effect, called enhanced Auger recombination, reduces the intrinsic lifetime of silicon and is the limiting process for ultra pure silicon doped above $N_{D/A} \approx 1 \times 10^{15}$ cm^{-3} [106,107]. A useful approximation of the Auger-lifetime at low doping concentrations and low injection conditions at 300 K for p-type is given by Schmidt [108]:

$$\tau_{Aug} = \frac{2.374 \times 10^{24}}{N_A^{1.67}}. \tag{2.19}$$

Recombination via band gap states

Electronic states in the band gap are present either due to intentionally doping, e.g. for pn junction formation and optoelectronic purposes, or due to defects in the bulk material. The kinetics of the recombination are described by the Shockley Read Hall statistics (SRH), proposed independently by Shockley and Read [102], and Hall [103]. The excess energy may be released by several possible mechanisms [109]: Similar to band to band recombination, radiative and Auger recombination occur. In addition, cascading– and multi–phonon–processes take place, where the energy is lost either by the carrier dropping through a series of closely spaced levels, emitting one phonon during each step [110], or by vibronic coupling to the lattice and excitation of local phonons [111].

The SRH-theory is based on a two-step model, where an electron from the conduction band and a hole from the valence band are captured or 'trapped' successively in the defect level E_t (often called 'trap' level). The efficiency of the capture and emission processes of carriers from and to the trap are determined by the capture cross sections σ_n and σ_p for electrons and holes, respectively, as pictured in figure 2.6. In thermal equilibrium the rates of carrier capture and emission are equal. The SRH-recombination rate U_{SRH}, i.e. the net rate of electron–hole recombination is given by

$$U_{SRH} = \frac{v_{th}\sigma_n\sigma_p N_t(np - n_i^2)}{\sigma_n(n + n_1) + \sigma_p(p + p_1)} \quad , \tag{2.20}$$

where v_{th} is the thermal velocity of the carriers, and the SRH-densities n_1 and p_1

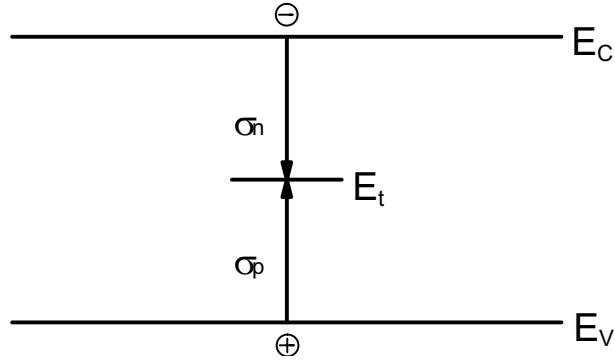$$n_1 = N_C \exp(-\frac{E_C - E_t}{kT}) \quad , \qquad p_1 = N_V \exp(-\frac{E_t - E_V}{kT}) \tag{2.21}$$

Figure 2.6: Two-step recombination via a defect level E_t. Electrons and holes are captured successively into the trap level. The efficiency of the capture processes is determined by the capture cross sections σ_n and σ_p , respectively.

are the numbers of electrons and holes in the conduction and valence band, respectively, in the case in which the Fermi level falls at E_t.

With $n = n_0 + \Delta n$, $p = p_0 + \Delta p$, $\Delta n = \Delta p$ and using equation 2.7, the Shockley-Read-Hall lifetime τ_{SRH} is given by

$$\tau_{SRH} = \frac{\tau_{n0}(p_0 + p_1 + \Delta n) + \tau_{p0}(n_0 + n_1 + \Delta n)}{p_0 + n_0 + \Delta n}, \qquad (2.22)$$

where the capture time constants are given by $\tau_{n0,p0} = (N_t \sigma_{n,p} v_{th})^{-1}$. From equation 2.22 it is obvious that τ_{SRH} depends on the injection level Δn, the doping level (via n_0 and p_0), the defect density N_t, and in particular on the defect level E_t via n_1 and p_1. The highest recombination, and hence the lowest carrier lifetime τ_{SRH}, results from defect levels with E_t close to the center of the band gap, i.e. $E_t \approx E_i$.

Surface recombination

Figure 2.7 illustrates the situation at the semiconductor surface. Unsaturated 'dangling' bonds of the surface atoms result in a large density of defect states N_S, the so called surface states. In most cases these surface states have a quasi continuous distribution in energy $N_S(E)$, depending on the surface reconstruction or adsorption of other species, such as oxygen or metallic contaminations. For the calculation of the surface recombination rate
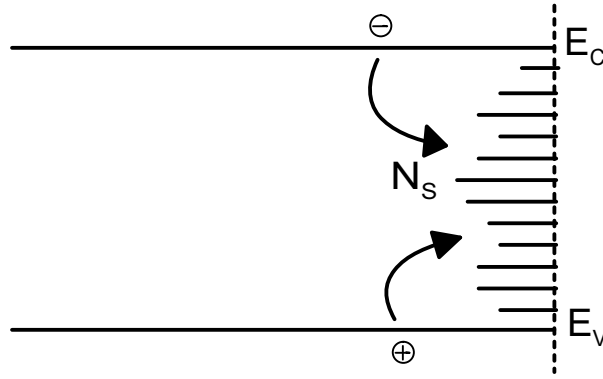
Figure 2.7: Illustration of the recombination via continuous surface states N_S result-
ing from dangling bonds of the distorted semiconductor lattice.

U_S the recombination via the surface states is evaluated by applying SRH-statistics (see
equation 2.20) integral to the surface defects under the assumption, that no interaction
between the states occurs. Depending on the densities of electrons n_S and holes n_p at the
surface, U_S is given by

$$U_S = \int_{E_V}^{E_C} \frac{v_{th}\sigma_n(E)\sigma_p(E)N_S(E)(n_S p_S - n_i^2)dE}{\sigma_n(E)(n_S + n_1(E)) + \sigma_p(E)(p_S + p_1(E))}. \qquad (2.23)$$

Instead of a "surface lifetime", a surface recombination velocity S is defined by

$$S = \frac{U_S}{\Delta n_S}, \qquad (2.24)$$

where Δn_S is the injection level at the surface. The surface recombination velocity shows
a complicated dependence on the injection level Δn_S, the doping concentrations n_0 and
p_0, and the capture cross sections $\sigma_{n,p}$ [108].

2.3 Structure of silicon surfaces

The surface of a single crystal may be regarded as a large two dimensional defect, where
the translatory symmetry of the crystal is broken. The driving force for the creation of
the real structure of the surface is the minimization of the surface energy. Two factors
contribute to the surface energy: (i) the density of dangling bonds, and (ii) the surface

stress. Surface stress is generated when the surface atoms rebond in order to reduce the number of dangling bonds. Both factors depend on the orientation of the surface. The surfaces with the lowest numbers of dangling bonds per surface area will have the lowest surface energy and consequently be the most stable surfaces[1] [113].

In fact, only very few Si-surfaces are known to be thermodynamically stable surfaces (also called primary or singular surfaces). Among these are the surfaces with low Miller indices (100), (110), (113), and (111) [113,114]. The number of broken bonds and the number of atoms per surface area and the resulting surface energy for these surface orientations is given in table 2.2.

Table 2.2: Number of broken bonds and atoms per area and resulting surface energy for truncated 1 x 1 silicon surfaces. After [113].

surface orientation	atoms per area 1×10^{14} cm^{-2}	broken bonds per area Å^{-2}	surface energy per area eVÅ^{-2}
(111)	16.0	0.080	0.09
(110)	9.6	0.096	0.11
(113)	8.3	0.125	0.14
(100)	6.9	0.139	0.15

The Si(111) surface shows the lowest surface energy because the Si-Si bonds in the bulk are all directed along one of the <111> directions. Indeed, silicon crystals cleave preferentially along {111}-planes under applied stress [113]. If the surface orientation is not exactly along one of these stable surfaces, i. e. a small deviation of only a few degrees, then the surface consists of flat terraces with the stable orientation separated by steps. Those vicinal surfaces orientations have a higher surface energy due to the non-saturated dangling bonds at the step, getting higher with increasing angle to the stable surface. If the angle of the surface orientation to a stable surface gets too high, facetting of the surface

---

[1]A thermodynamically stable surface is represented by a cusp in the Wulff surface energy plot [112].

occurs, i. e. the steps themselves form a stable surface, and the surface then consists of sawtooth-like facets of adjacent stable surfaces [114].

The stable surfaces themselves show certain reconstructions of the surface atoms. The nomenclature is given by the dimensions of a unit cell of reconstructed atoms. A 1×1 surface reconstruction simply means, that no reconstruction of the surface occurs and each atom is exactly at the expected bulk site. In a 2×1 reconstruction, the dangling bonds of two neighboring atoms bond, resulting in a deformation of the surface structure, but reduced dangling bond density. The evolvement of such surface reconstructions depends of the substrate orientation and the temperature.

For epitaxial thin film deposition, the surface structure is of crucial importance for the growth. With the exception of subplantation effects in ion-beam and ion-assisted growth, all CVD and PVD processes are determined by the diffusion of adatoms on the surface and the incorporation of atoms at epitaxial sites, which requires a reordering of the surface reconstruction.

Si(100)

The reconstruction of Si(100) has widely been studied because of its technological importance. Each atom on the truncated Si(100) surface has two dangling bonds. A 2×1 dimerization of the surface atoms reduces the number of dangling bonds [115,116]. All dimers on a terrace of Si(100) are alined in the same direction. However, the dimers are "buckled", i.e. the dimer is asymmetrically bound, one atom is bended closer to the surface, the other one is elevated [117]. This effect is due to a rehybridization of the unoccupied orbitals [118]. The buckling not only affects the bonding structure of the two atoms, but a superstructure of the reconstruction is observed, the so called $c(4 \times 2)$-structure. An important consequence of the 2×1 dimerization is anisotropic adatom diffusion [119].

As surfaces in reality generally show a small miscut to the desired orientation, the surface is formed by terraces separated by steps (even exactly oriented surfaces show steps [120]). According to Chadi, the steps are classified with S (single) for monoatomic steps and D (double) for biatomic steps. A step is labeled S_A or D_A, if the dimers on

the upper terrace are perpendicular to the edge of a straight step and S_B or D_B if the dimers on the upper terrace are parallel to the step edge [121]. For monoatomic steps the direction of the dimer rows is rotated by 90° from one terrace to the next, i.e. S_A and S_B vary alternatively from step to step. On the other hand, the upper and the lower terrace of biatomic steps have the same orientation of the dimers. The steps themselves then might show a reconstruction of the surface atoms, resulting in rebonded and non-rebonded monoatomic and biatomic steps. On Si(100) surfaces with miscut along the [110] direction, biatomic steps in equilibrium are only stable if the miscut angle is at least of the order of 1.5° at a temperature of 500°C [122]. However, step bunching, i.e. the creation of higher steps by several monoatomic steps can occur under certain deposition conditions. Such step bunching might be due to the fact that S_B steps are better sinks for adatoms than S_A steps [123], or to step flow instabilities such as Schwoebel barriers.

The morphology of epitaxial films deposited on Si(100) depends on numerous parameters, such as the deposition temperature, the deposition rate, the miscut angle and the orientation of the miscut. Growth instabilities due to kinetically limited surface processes might result in surface roughening or the formation of ripples in μm thick films, even in step-flow growth mode up to deposition temperatures of 500°C [27].

Si(110)

A 16×2 reconstruction is observed on Si(110) after cooling down to 750°C after a prebake at 1200°C for cleaning. Above 750°C the 16×2 transforms into a disordered 1×1 [124,125].

Si(113)

At room temperature the Si(113) surface is reconstructed by a 3×2 periodicity [126]. This is converted reversibly to a 3×1 reconstruction in the temperature range of 450 to 600°C, and for temperatures above 600°C the 1×1 structure is stable [127].

Si(111)

After cleaving, Si(111) reconstructs in 2 x 1 [128]. However, this reconstruction is
metastable, and the periodicity changes to the stable 7 x 7 after annealing [129]. The
7 x 7 is very complex, consisting of nine dimer bonds, twelve adatoms and a subsurface
stacking fault (Dimer-Adatom-Stacking fault (DAS) reconstruction) [130,131]. Only if the
surface is flat, a metastable 5 x 5 structure can be formed on Si(111) at 330°C. This is a
consequence of the fact, that a reordering from 1 x 1 to 7 x 7 requires mass transport across
the surface from steps due to the difference in the number of atoms contained in the DAS
7 x 7 reconstruction compared to a 7 x 7 area of the truncated bulk. The 5 x 5 transforms
irreversibly to the 7 x 7 for temperatures above 600°C [132].

The stability of the 7 x 7 reconstruction has influence on the epitaxial growth at low
deposition temperatures. Gossmann and Feldman reported reduced structural quality of
Si-films deposited at room temperature on Si(111) compared to deposition on Si(100),
and assigned this difference to the stability of the 7 x 7 reconstruction with its inherent
stacking fault [28].

Chapter 3

Experimental

3.1 Deposition of epitaxial films

3.1.1 Sample preparation

Substrate materials

As monocrystalline substrates we either use 4" (100)- and (111)-oriented wafers (WACKER or FREIBERGER) or (100)-, (111)-, (110)-, and (113)-oriented samples, respectively, that were cut to a size of 25 x 25 mm^2. The cut samples undergo an RCA cleaning sequence [133]. As polycrystalline substrates, block cast BAYSIX-wafers from BAYER AG, Germany are used.

Substrate cleaning

In order to obtain high quality epitaxial growth, the substrate surface is of crucial importance. Any leftover particles, even elements or silicides on the surface may cause defects in the epitaxial films. Therefore the silicon surface has to be free of any contaminations including silicon oxide. An ideal surface would be achieved by cleaving silicon under UHV conditions, which is done for surface investigations. For epitaxy with high throughput and the use of standard wafers, simpler methods have to be applied. These can be divided in-situ and ex-situ methods. Most commonly, ex-situ cleaning consists of wet chemical

treatments such as the RCA method [133], which removes metallic and organic contaminations from the surface by subsequent oxidation- and oxide-removal-processes. In-situ cleaning can be achieved, for example, by a hydrogen plasma or sputtering of the surface.

Silicon oxide removal

A thin 'native' Si-oxide forms on a clean Si-surface, when kept under ambient conditions with oxygen present. Therefore, silicon samples normally are covered with a thin Si-oxide layer, that has to be removed prior to deposition. Similar to substrate cleaning, the silicon oxide removal is either carried out in-situ or ex-situ. When the substrate and the process allow for high temperatures of more than 850°C, thermal oxide removal might be applied. Here the chemical reaction

$$Si(s) + SiO_2(s) \rightleftharpoons 2SiO(g) \tag{3.1}$$

applies, with (s) = solid and (g) = gaseous phase. When a small amount of Si-atoms is provided during this prebake, the equilibrium is shifted to the gaseous SiO side of equation 3.1, and oxide desorption is possible down to temperatures of 700°C [134].

Ex-situ oxide removal is accomplished by a wet chemical etching in diluted hydrofluoric acid (HF). After this treatment, the surface is terminated with hydrogen and remains oxide-free for several minutes under ambient conditions. After installation in an UHV-chamber, growth can be started immediately at the desired deposition temperature without any further high temperature pretreatment. It is noted, that such a final HF-dip before installing the samples in the chamber results in a visible contrast at the surface-epilayer interface in TEM-investigations and was therefore omitted.

3.1.2   Ion assisted deposition

Deposition chamber

As ion assisted deposition is an advanced molecular beam epitaxy method, the deposition system consists of typical elements of a MBE system. The deposition chamber is an ultra

high vacuum chamber *Uni 107 P* from *RIBER* , equipped with a turbo pumped load lock. The upper part of the chamber is water cooled and can be lifted for maintenance purposes by a pneumatic lifter. In the lower part, the pumping system is located. It consist of a titanium sublimation pump, an ion-getter pump and a cryogenic panel, operated with liquid nitrogen. The two parts of the chamber are sealed by either a 540 mm diameter fluoroelastomer (viton) or a silver plated copper gasket. The attainable base pressure is 1×10^{-7} Pa with the viton and 6×10^{-8} Pa with the metal seal. Figure 3.1 shows a schematic drawing of the setup of the IAD-reactor.
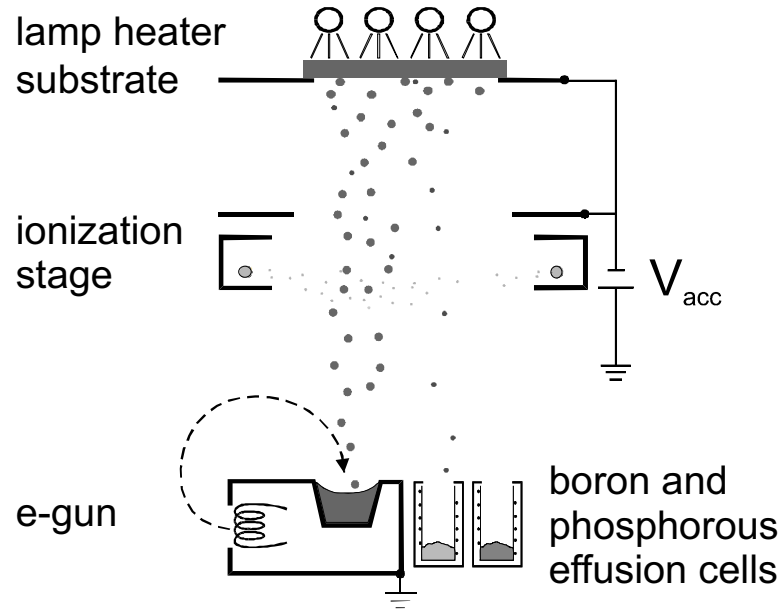

Figure 3.1: Schematic illustration of the ion-assisted reactor setup. An electron beam evaporator (e-gun) serves for the evaporation of ultra pure silicon. In situ doping is possible by the use of boron and phosphorus Knudsen cells. Electrons emitted by a heated tungsten wire in the ionization stage are accelerated towards the center of the chamber, where a fraction of about 1% of the Si-atoms is ionized. This Si^+-ions are accelerated towards the substrate by an applied bias voltage V_{acc}.

Silicon is evaporated from a water cooled copper crucible using an electron gun from AP&T. The deposition rate is limited by the diameter of the molten silicon surface in the

crucible, and therefore on the electron beam current and the distance to the substrate, which accounts to about 30 cm. Deposition rates of up to 0.8 μm/min are achieved in the system, equipped with crucible of 63 cm^3 volume. A polycrystalline Si-feedstock located in the vacuum chamber serves to refill the crucible without opening the chamber. This results in high up-times even for total deposition thicknesses of more than 100 μm. Effusion cells from MBE-KOMPONENTEN allow for in situ doping with boron and phosphorus of the Si-films. Elemental boron is evaporated at temperatures of $1700\ldots1950°$C, phosphorus is decomposed from GaP at temperatures of $760\ldots820°$C. The substrate is heated from the backside up to $820°$C by the use of four halogen lamps. The temperature was calibrated by pyrometer measurements and is controlled during deposition by a thermocouple close to the substrate. Residual gases during deposition are monitored by a BALZERS QMS 422 mass spectrometer. The main fraction during deposition is hydrogen and is of the order of 5×10^{-6} Pa.

Ionization stage

The main difference between IAD and MBE is the toroid-shaped ionizer that is located in between the electron gun crucible and the substrate. The ionizer consists of a resistively heated tungsten wire and several molybdenum-electrodes. Ionization is achieved by the emission of thermal electrons from the glowing tungsten wire, which are accelerated to the center of the ionization stage and ionize there a small fraction (about 1 %) of the evaporated silicon atoms from the e-gun. The energy of the Si$^+$-ions is controlled in the range of 0 to 1000 eV by applying an acceleration voltage to the substrate and to an additional acceleration electrode.

If not mentioned otherwise we use an optimum value of the ion energy of 20 eV, which can also be found in literature on ion-beam epitaxy as the ideal trade off between positive effects of the Si-ions and additional defect generation by ion bombardment [13].

Deposition process

After installing the substrate in the vacuum chamber, a ten minute annealing step at 290°C serves for the desorption of H_2O and CH-adsorbates. Subsequently, all substrates undergo a ten minute in-situ prebake at 810°C for silicon oxide removal. In order to support oxide desorption, silicon evaporation at low rates is initiated during the prebake before cooling down to deposition temperature [134].

3.1.3   Hydrogen passivation

Hydrogen passivation was carried out using an OXFORD PLASMALAB 80+ downstream microwave remote plasma reactor. The downstream area has a diameter of 20 mm. The samples are kept at 380°C during the one hour treatment. The microwave power is 250 W. In order to verify the effectiveness of the hydrogen treatment, some of the samples underwent an equivalent annealing step in nitrogen atmosphere. This annealing had no effect on the point defect densities, as verified by PL. Hence, the observed effects are due to the incorporation of hydrogen in the silicon bulk.

3.2   Characterization of defects

3.2.1   Photoluminescence: Optically active defects

Photoluminescence spectra are recorded using an Ar-ion laser operating at 488 nm, a JOBIN YVON HR460 monochromator equipped with a 600 line/mm grating, and a cooled NORTH COAST germanium detector. The samples are cooled down in a OXFORD cryostat operated by a closed cycle helium refrigerator, that allows to control the temperature down to 11 K. The germanium detector restricts the measurable photon energies to $h\nu > 0.7$ eV. A lock in amplifier serves to evaluate the intensity-signal. The spectra are corrected for transmission of the optical components [135]. Note that this correction becomes important for photon energies below 0.73 eV, resulting in a high measurement error in the energy range of 0.7 eV $< h\nu < 0.73$ eV. The laser power for a standard measurement

is adjusted to 90 mW, focused on a spot with approx. 1 mm diameter, corresponding to a typical excitation energy of 11.5 Wcm^{-2}. The resolution of the spectra is determined by the entrance and exit slit widths of the monochromator, which can be opened up to 1.9 mm. A rotatable sample holder allows for the measurements of up to 6 samples during one session, without changing the optical setup.

In order to compare directly the intensity of the spectra, samples are measured with exactly the same optical setup and laser power. Most of the spectra compared in the figures shown in this work are measured within one session, i.e. without any change of the setup. It is verified that measurements of the same film do not vary more than 10% in intensity if measured in different sessions, even after a long time in between. If not indicated otherwise the spectra are not normalized and show directly the measured intensity with the standard setup.

3.2.2 Deep level transient spectroscopy: Electronically active defects

Deep level transient spectroscopy (DLTS) allows for the characterization of defects in semiconductors by the evaluation of the transient junction capacitance in dependence of the measurement temperature [136]. In a standard measurement, the samples are kept under a reverse bias voltage, resulting in a space charge region width of $W_{j,b}$. A short forward voltage puls serves to change the space charge region width by $-\Delta W_j$. During this puls, the charge state of defect levels in the region of ΔW_j is changed, and consequently the capacitance of the junction C_j as well. After the puls ($t = 0$), the junction capacitance restores its original value with a characteristic transient given by

$$C_j(t) = C_{j,0} \pm \Delta C \exp(e_{p,n}t), \qquad (3.2)$$

with $C_{j,0}$ the junction capacitance under reverse bias and $e_{p,n}$ the emission frequency of holes or electrons to the respective band. The signum of the transient is dependent of the type of the trap, i.e. if the defect level is acting as a majority or minority carrier trap.

The samples under investigation require a one sided abrupt junction. This can be

either achieved by the formation of a Schottky contact or an abrupt pn-junction. The planar size of the junction hereby determines the capacitance of the diodes. The used capacitance bridge only allowed the analysis of diodes with a capacitance $C_{j,0}$ below 1 nF. For the films deposited by IAD this requires diode diameters below 1 mm. In the case of n-type films, a Schottky junction was formed by the evaporation of small gold contacts. In the case of p-type films, neither contacts with gold or titan did result in a satisfying diode characteristic, although Schottky diodes formed on similarly doped reference wafers succeeded. Therefore, in situ doped one sided abrupt n^+p-junction films are used for the analysis of p-type films. A photolithogaphic structuring process was developed, in order to fabricate mesa-diodes with a diameter of ≈ 1 mm.

A SEMITRAP DLS 82 spectrometer serves for the measurement of the DLTS spectra. The spectrometer employs a lock-in technique, with a sampling frequency of 1 MHZ. The configuration of the lock-in amplifier ensures that the repetition frequency of the voltage pulses f_p is directly related to the emission frequency $f_p = e_{p,n}$. During a temperature sweep, a deep level defect results in a peak of the DLTS signal ΔC from the lock-in amplifier. The trap density N_t in the case of a single trap level is directly proportional to ΔC by

$$N_t = N_{D,A} B_{DLTS} \frac{\Delta C}{C_{j,0}}, \tag{3.3}$$

where $N_{D,A}$ is the doping concentration of the material and B_{DLTS} is a proportional constant given by the configuration of the lock-in amplifier. The determination of the defect density of broad defect bands requires a more elaborated evaluation of the respective peak. However, most of the spectra investigated in this work show overlapping peaks, and therefore, the defect density corresponding to the maximum of the peak is given as a rough estimate.

The temperature of the peak maxima vary with the repetition frequency f_p. Several measurements with different f_p are carried out, in order to determine the energetic position of the defect level. This is done by an Arrhenius plot of f_p/T^2 versus the respective temperature of the peak maximum. A fit to the slope of the repetition frequency–temperature points reveals the activation energy of the defect level. The intersection of this slope with

the Y-axis is a measure for the capture cross section of the trap level.

Several mechanisms limit the sensitivity of the method. The detection limit of the trap density is determined by the doping density of the sample, and is of the order of $N_t \approx 1 \times 10^{-3}\ N_{D/A}$. Films deposited by IAD show a typical n–type background doping in the range of $N_{D0} = 5 \times 10^{14} \ldots 1 \times 10^{16}$ cm^{-3}, as revealed by CV-measurements. The background doping is caused by residual phosphorus in the chamber that desorbs from the chamber walls during subsequent deposition processes. It depends on the Si deposition rate and on the chamber status i.e. phosphorus doping level used in previous experiments and chamber wall temperature during deposition. For nominally intrinsic samples, the detection limit is therefore of the order of 1×10^{12} cm^{-3}. For p-type films, the doping level has to exceed the n-type background doping in order to ensure an overcompensation of the background doping. This results in a DLTS detection limit of $N_t \geq 1 \times 10^{13}$ cm^{-3} for p-type films. As a consequence, only films with a defect density above these limits show a signal in DLTS measurements.

The capacitance, as well as the capacitance-voltage measurements (CV) used for the determination of the doping density of the films, are carried out using an impedance analyser of type HP 4192A. Typically, the capacitance is measured at frequencies of 1 kHz to 1 MHz with an amplitude of 50 mV. During the CV measurements, a HP 3487A multimeter serves for the measurement of the voltage drop at the sample.

For the DLTS and Capacitance measurements, the samples are mounted in a liquid nitrogen cooled cryostat, that allows for temperature control in the range of $80 \ldots 420$ K.

3.2.3   Defect etching: Extended structural defects

Preferred wet chemical etching is an important tool in the characterization of extended structural defects in silicon. Etching solutions that contain dicromat-ions ($Cr_2O_7^{2-}$) and hydrofluoric acid (HF) are particularly suited for the demonstration of defects, such as dislocations and stacking faults, because of their high anisotropic etch rate at lattice inhomogeneities. The etching process results in characteristic etch pits for different structural defects [137]. The Secco-etch solution [138] used in this work generates small oval pits at

the surface intersection of dislocations for (100)- and (111)-oriented surfaces. In the case of stacking faults, the partial dislocations associated with the stacking fault show typically a quadratic or triangular form for (100)- and (111)-oriented surfaces, respectively. The density of dislocations is evaluated by counting the number of etch pits n_{ep} or the number of lines, squares or triangles in the case of stacking faults, found on the surface after etching. For this purpose, an optical microscope, equipped with an Nomarski Differential Interference Contrast (NDIC) unit [139] is used. As the accuracy of this method decreases with decreasing number of etch pits, values of $n_{ep} < 1 \times 10^3$ cm^{-2} and $n_{ep} < 1 \times 10^2$ cm^{-2} represent upper limits of the etch pit density for dislocations and stacking faults, respectively. The actual etch pit density may be significantly lower. Typical etching times are in the range of 1 to 3 min.

3.3 Electronic characterization

3.3.1 Quantum efficiency

The quantum efficiency is the ratio of the short circuit current j_{SC} generated by monochromatic light of wavelength λ to the impinging photon flux $\Phi_{ph}(\lambda)$. Two types of the quantum efficiency are distinguished: (i) The external quantum efficiency EQE(λ) is a measure of the whole device including optical and electronic properties. The EQE is defined by

$$EQE(\lambda) = \frac{j_{SC}}{q\Phi_{ph}(\lambda)}, \tag{3.4}$$

where q is the elementary charge. (ii) The internal quantum efficiency IQE additionally takes the reflectance R of the device into account. Here, only the electronic properties and internal reflection determine the quantum efficiency. The IQE is calculated from the EQE by

$$IQE(\lambda) = EQE(\lambda)\frac{1}{1 - R(\lambda)}. \tag{3.5}$$

The measurements of the EQE and the reflectance are carried out in a VARIAN spectrometer equipped with an Ulbricht sphere. These two measurements allow for the determination of the IQE. From the IQE, the minority carrier diffusion length L is deduced,

using the software IQE1D [140]. On the basis of an analytical model under consideration of the optical and electronic transport properties of thin solar cells, this software allows for a least squares fitting of the IQE in order to deduce the device relevant parameters, such as minority carrier diffusion length or surface recombination velocities [141]. This evaluation method gives reliable results for the diffusion length, when the diffusion length L is higher than the space charge region width W_j and not significantly larger than the cell thickness W. In the latter case, the diffusion length of the base material is no more the limiting factor of the device performance, and the accuracy for the determination of L decreases. However, diffusion lengths of the order of the cell thickness have to be regarded as a lower limit of the actual diffusion length of the material only, as the correct value might be even higher [141].

3.3.2 Light beam induced current

For light beam induced current (LBIC) measurements a laser beam of wavelength 780 nm is scanned across the surface of a test solar cell, and the spatial resolved short circuit current generated by the laser beam is detected. As the induced current of a small laser beam, especially in the case of solar cells with a high number of defects, is rather small, the laser beam intensity is modulated and a lock-in technique for recording the short circuit current is used. At this wavelength the laser light has an absorption length of around 10 μm in silicon and is therefore well suited for the characterization of epitaxial thin film solar cells. Locally electric active defects, such as grain boundaries generate a contrast in the LBIC mapping, allowing easy identification. Also for polycrystalline films, the recombination activity of grain boundaries and single grains can be studied. For the latter application, especially for thin films deposited on large grained BAYSIX-wafers, spatial resolutions of 25 μm are applied. However, with careful tuning of the optical setup, measurements with a resolution in the μm range are possible.

Chapter 4

Defects in low temperature epitaxial films on Si(100)

The electronic and mechanical properties of silicon depend to a high extend on the defects present in the material. Photoluminescence and DLTS spectroscopy, as well as defect etching serve to analyze the density of extended structural defects and the density and electronic levels of point defects in the films deposited by MBE and IAD. Since the Si(100)-orientation is the most commonly used wafer-orientation for microelectronic and solar cell applications, and film deposition on such substrates yields the best electronic and structural properties, this chapter only reports on films deposited on (100)-oriented substrates. Deposition on other monocrystalline or polycrystalline substrates will be discussed in chapter 6.

4.1   Extended structural defects

Preferential wet chemical etching, using the etch solution proposed by Secco d'Aragona [138], serves to determine the type and density of structural defects in the films. Table 4.1 compares the density of structural defects in epitaxial thin films deposited on substrates which underwent a certain ex-situ pretreatment with the density in films which are deposited on wafers without any ex-situ pretreatment. It is noted that all substrates

underwent an in-situ annealing step for oxygen removal, see page 37. The ex-situ pre-treatment consists of a cutting step on semiconductor disc saw and a subsequent RCA cleaning [133] of the samples. During the cutting, the wafer surface is covered with an adhesive tape, that is easily removed after UV-light exposure. The density of disloca-tions and stacking faults, as given in table 4.1, is below 1×10^3 cm^{-2}, when epitaxial films are deposited on wafers without ex-situ pretreatment as delivered from the manufacturer (WACKER SILTRONIC). Note that the values for the as delivered (100)-oriented films only represent an upper limit for the defect density due to the detection limit of the analysis method. On some wafers, the extended defect density is estimated to be below 1×10^2 cm^{-2}.

Films deposited on substrates that underwent the ex-situ pretreatment show high dis-location densities above 1×10^4 cm^{-2}. The dislocations most likely originate from particles on the wafer surface [7], that are not completely removed by the cleaning step. It is noted, that old wafers, though stored in original packaging, have a high density of defects vis-ible on the surface (before and after deposition) after Secco etching. This is a result of contamination from the plastic coverage, aging over the years and emitting particles.

Table 4.1: Density of structural defects in films deposited on substrates with and without ex-situ pretreatment, respectively. The films are deposited at $T_{dep} = 460...700°C$ and $r_{dep} = 0.1...0.5$ $\mu m/min$.

Substrate	defect density (cm^{-2})	
pretreatment	dislocations	stacking faults
cutting + RCA	$> 1 \times 10^4$	$< 1 \times 10^2$
no pretreatment	$< 1 \times 10^3$	$< 1 \times 10^2$

As an important result, the density of extended defects is below 1×10^3 cm^{-2}, indepen-dent of the deposition temperature and rate for films deposited on p-type (100)-oriented substrates in the range of $T_{dep} = 460...700°C$ and $r_{dep} = 0.1...0.5$ $\mu m/min$ on wafers

without ex-situ pretreatment. Therefore, epitaxy at low temperatures does not result in higher densities of dislocations or stacking faults. Instead, the density of extended defects is only determined by the surface pretreatment. This also holds for the case of IAD with acceleration voltages up to 100 V. Here, the defect density shows a small increase to values around 2×10^3 cm^{-2}.

4.2   Optically active defects

As stated in the previous chapter, the density of extended defects in the films is low and therefore, film properties are mainly dominated by the presence of point defects, such as interstitials, vacancies, impurities, and their complexes. Photoluminescence as well as DLTS allow for the characterization of thin films in respect to point defects acting as recombination centers or traps for carriers. The density of optically active point defects is determined using photoluminescence while DLTS analyzes electrically active point defects.

Photoluminescence spectra reveal information about radiative recombination of excess carriers only. Non-radiative recombination, such as Auger recombination or SRH-recombination via multi-phonon or cascading processes, are not directly accessible by luminescence methods. However, if non-radiative recombination occurs, the number of excess carriers recombining radiatively is reduced and lower defect and band to band luminescence is observed. Therefore, the total luminescence intensity is a signature of the non-radiative recombination, and in particular the band to band luminescence is a measure of the carrier lifetime.

Deep level transient spectroscopy, on the other hand, is sensitive to the capture process of traps in the depletion layer of pn-junctions or Schottky contacts. The DLTS signal is proportional to the number of traps, and from several DLTS measurements at different repetition rates the energetic level of a trap can be deduced. The information obtained by the combination of these two methods combined gives an insight in the energetic distribution and recombination activity of point defects in the films.

4.2.1 Low temperature epitaxial films

Photoluminescence from intrinsic films

Films that are deposited without the use of the boron and phosphorus effusion cells always show an n-type background doping from residual phosphorus desorbing from the chamber walls. The background doping level depends on previous phosphorus doping processes in the chamber, on the history of the chamber, i.e. the number of previous depositions without phosphorus and on the deposition rate and temperature (see page 37 for a description of the standard deposition process). The background doping level varies in the range of 5×10^{14} cm^{-3} to 5×10^{15} cm^{-3}, as determined from CV-measurements. These films will be referred to as intrinsic films, in contrast to typical phosphorus dopant densities of 1×10^{19} cm^{-3} for emitter formation in solar cells. Figure 4.1 gives an example of an intrinsic film deposited at $T_{dep} = 550°$C and $r_{dep} = 0.1$ μm/min by IAD, compared to luminescence from the low phosphorus doped ($N_D \approx 1 \times 10^{15}$ cm^{-3}) wafer used as substrate for this film. As the film thickness is 3 μm and the absorption length of the laser light used for the PL measurements with $\lambda = 488$ nm is of the order of 1 μm, about 95 % of the luminescence intensity stem from the deposited epitaxial film. Both samples present the typical phonon assisted free- and bound-exciton transitions known from low phosphorus doped silicon (see section 2.2.2) for photon energies above 1.0 eV. However, only the epitaxial film shows luminescence at lower photon energies ($h\nu < 0.8$ eV), corresponding to deep level defect transitions.

Doped epitaxial films

A typical example of photoluminescence from a doped Si-film is given in figure 4.2a). The film was deposited by MBE, i.e. without applied acceleration voltage, and consists of a pn-solar cell structure with a 14 μm thick boron doped base (doping concentration $N_D \approx 1 \times 10^{17}$ cm^{-3}) and a high phosphorus doped emitter with a thickness of ≈ 0.3 μm (doping concentration $N_D \approx 1 \times 10^{19}$ cm^{-3}). In contrast to intrinsic films, several broad peaks around 1.122, 1.102, 1.081, 1.047, and 0.987 eV are observed in the PL spectrum of the doped film. The newly detected peaks are labeled a to e, respectively. This spectrum
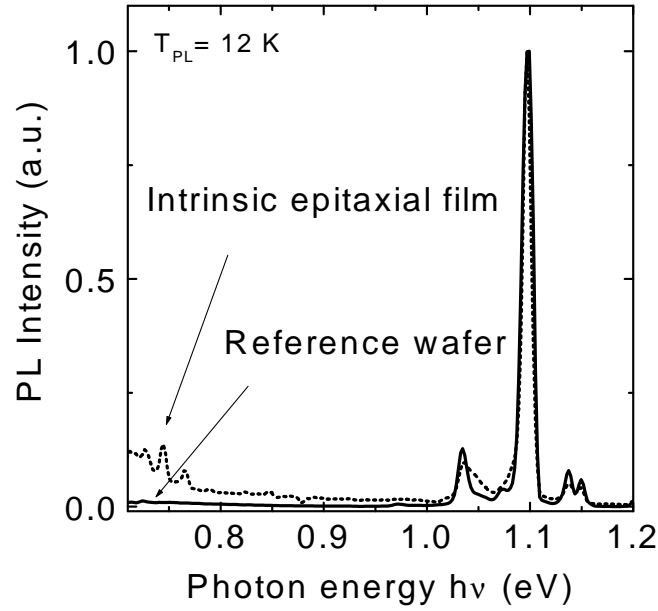
Figure 4.1: Photoluminescence of a 3 μm thin epitaxial film deposited at $T_{dep} = 550°C$ compared to the PL spectrum of the substrate wafer. The absorption length of the Ar-ion laser light ($\lambda = 488$ nm) is about 1 μm, therefore 95 % of the luminescence stem from the epitaxial film. For photon energies above 1 eV the typical phonon assisted free- and bound exciton transitions are observed for both samples. At lower energies the epitaxial film displays luminescence from deep level defects. The spectra are normalized with respect to the intensity of the highest peak.

is recorded with a slit width of 1000 μm, and consequently the spectral resolution is low. A higher resolution spectrum of the same film is given in figure 4.2b). Here the slitwidth is 300 μm, but nevertheless the peaks b, c, and e are still unresolved. Only the a-peak is sharp with a satellite at 1.125 eV. Further reduction of the slitwidth results in too low an intensity.

The **a-peak** and its satellite are identified by the A-line luminescence originating from excitons bound to an isoelectronic trap [81]. The **b-peak** is a superposition of several peaks and only two small features at 1.102 and 1.106 eV are resolved. The **c-peak** at 1.081 eV has no visible substructure around its maximum. This peak may originate from an electron hole droplet (EHD, see chapter 2.2.2). However, experiments with increased
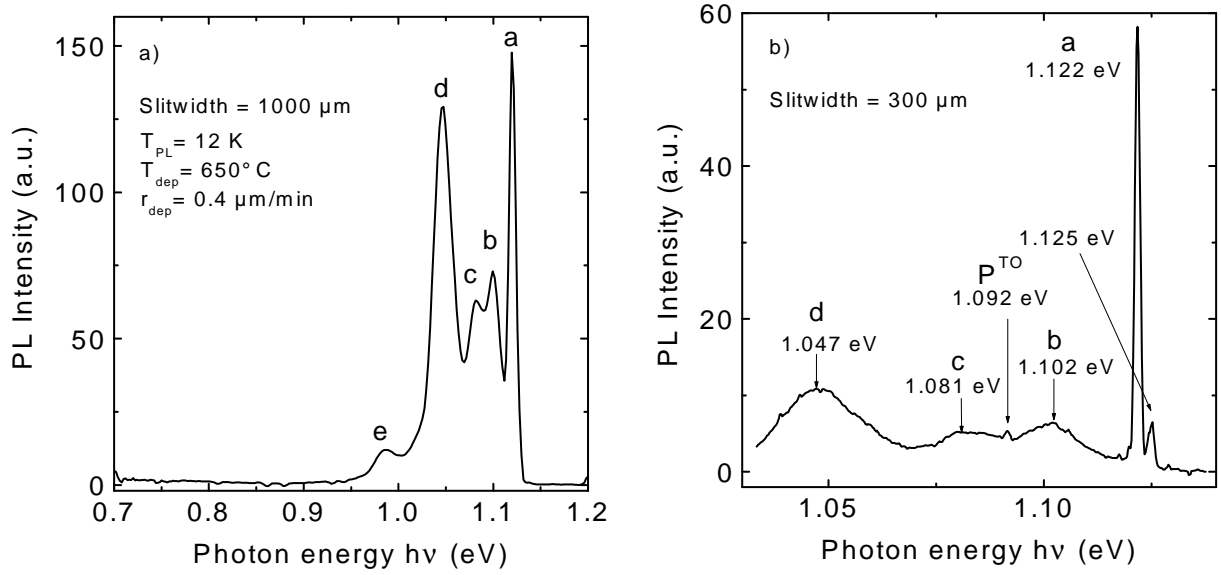
Figure 4.2: a) Total range photoluminescence spectrum of an MBE-film deposited at $T_{dep} = 650°C$ and $r_{dep} = 0.4 \, \mu m/min$. Peaks are observed around 1.122 (a-peak), 1.102 (b-peak), 1.081 (c-peak), 1.047 (d-peak), and 0.987 eV (e-peak). b) Same film measured with smaller slitwidth. The b, c, and d-peaks are still unresolved and reveal a broad substructure. Only the 1.122 eV peak is sharp with a satellite at 1.125 eV. The peak at 1.092 eV is the signature of the phosphorus transversal optical phonon transition P^{TO}.

laser power did not confirm that the c-peak is due to the EHD. Numerous investigations of over 20 IAD- and MBE-films allow the conclusion that the **d-peak** is most likely a superposition of several lines, themselves being rather broad. Numerical fits of the d-peak show three lines at 1.042, 1.047 and 1.052 eV. These peaks might belong to the O^j-system, consisting of thermal donors [142]. It has to be noted here, that the b-, c-, and d-peak almost always appear together. This behavior is similar to the reported Q- and S-lines (see [73]).However, these broad peaks are not observed in the intrinsic epitaxial film shown in figure 4.1. This may be due to a lower residual phosphorus doping level of the intrinsic film, as the electron beam evaporator in this case was running several hours prior to the deposition, in order to remove excess silicon from the crucible.

As expected, the high resolution spectrum shows a PL line at 1.092 eV due to the phosphorus bound exciton (P^{TO}).

MBE films at $T_{dep} = 460°C$

Broad defect luminescence is observed from films deposited by MBE at low temperatures $T_{dep} < 500°C$, as demonstrated in figure 4.3. The defect band below 0.9 eV has a maximum at 0.8 eV and an unresolved substructure with several quasi periodic peaks at $h\nu = 0.878$ eV and a period of $\Delta h\nu \approx 0.017$ eV. Similar broad defect bands around 0.8 eV have been
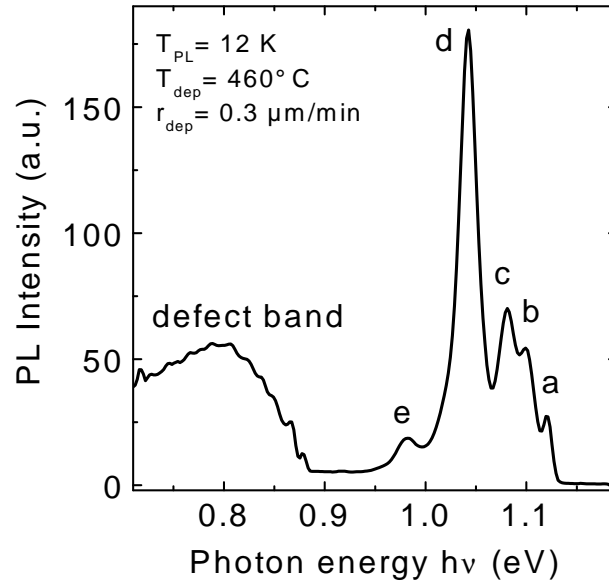
Figure 4.3: Photoluminescence spectrum of a low temperature ($T_{dep} = 460°C$) film deposited by MBE. In addition to PL peaks at high photon energies above $h\nu = 0.95$ eV, a broad defect band with a maximum at 0.8 eV arises.

observed in multicrystalline or implanted samples that show a high level of internal stress or strain [82,83] and in Si grown on strained Si-buffer layers [80].

4.2.2 Defects caused by ion bombardment

Figure 4.4 compares the photoluminescence from a film deposited by IAD ($V_{acc} = 20$ V) at $T_{dep} = 460°C$ and $r_{dep} = 0.3$ μm/min with the PL spectrum of a film deposited by

MBE using the otherwise identical parameters. The most prominent difference is found in the low energy range at 0.767 eV and below. The PL spectrum of the IAD-film shows several discrete peaks at 0.767, 0.749, 0.724, and 0.705 eV, that correspond exactly to the P-line luminescence observed in oxygen rich CZ-silicon after a heat-treatment at around 450°C [66,67,69]. However, the broad defect band around 0.8 eV is present in both films, and the intensity of the high energy peaks b, c, d and e is almost the same as in the case of the MBE-film. The a-peak, still visible as a shoulder in the MBE spectrum, is not present in the PL spectrum of the IAD-film.
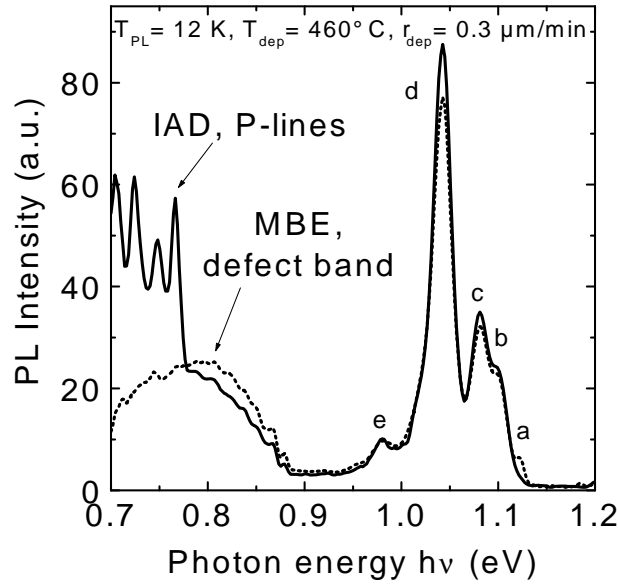

Figure 4.4: *Photoluminescence spectra of two films deposited with (IAD, $V_{acc} = 20$ V) and without (MBE) accelerated Si-ions in the molecular beam. Both films show broad PL intensity around $h\nu = 0.8$ eV. In addition, in the spectrum of the IAD-film P-line luminescence at 0.767 eV is observed. This indicates that Si ions generate the defect center responsible for P-line luminescence.*

The intensity of the P-lines is rising with increased acceleration voltage, as shown in figure 4.5 for a film deposited with $V_{acc} = 100$ V at $T_{dep} = 460$°C in comparison to $V_{acc} = 20$ V. Interestingly, the intensity of the high energy peaks b, c, d, and e is also higher, while the intensity of the defect band around 0.8 eV decreases. Additionally, a small peak

at 0.790 eV appears, identified with the so called "C-line" corresponding to a defect that is often observed after irradiation of silicon and that is associated with carbon and oxygen contamination of the sample [64,65].
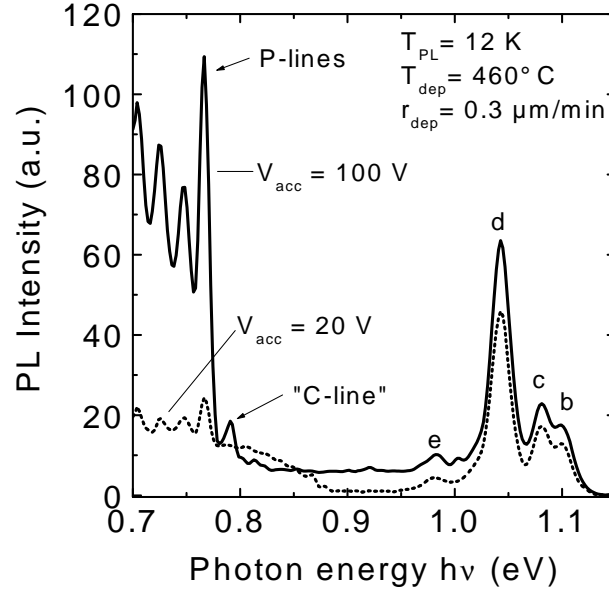

Figure 4.5: The film deposited at higher acceleration voltage V_{acc} = 100 V displays higher P-line intensity compared to the film deposited at V_{acc} = 20 V. At 0.790 eV the so called "C-line" appears, a defect that is often observed after irradiation of silicon and associated with the presence of carbon and oxygen. The b-, c-, d, and e-peaks remain unchanged in their intensity ratios, however, the total intensity in the high energy range of the film deposited with V_{acc} = 100 V is higher.

A closeup with a higher spectral resolution of the low energy range of the IAD-film deposited with V_{acc} = 100 V is given in figure 4.6. These measurements using different slitwidths allow for the identification of smaller peaks, which otherwise only appear as a shoulder of a peak with high intensity in low resolution measurements. In addition to the dominant P-lines, so-called "N-lines", an other thermal donor, are identified at 0.745, 0.758, 0.761, and 0.772 eV [63]. The N-defect has also a component at 0.767 eV, which cannot be distinguished from the main P-line at exactly the same energetic position. This N-defect is associated with the presence of nitrogen and carbon in silicon. In the high
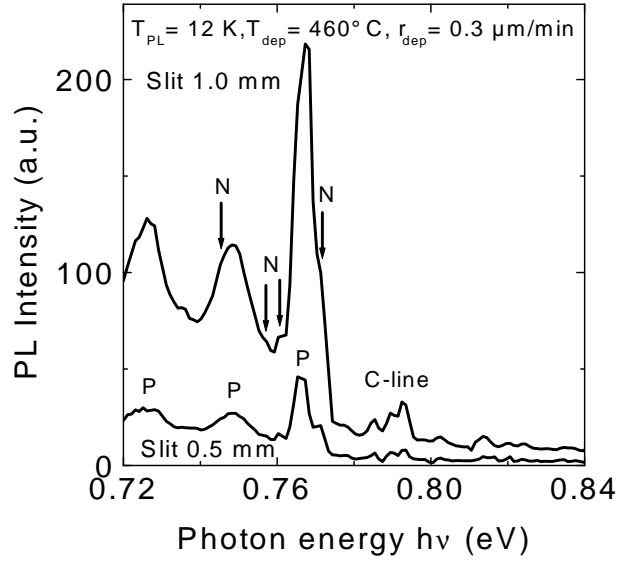
Figure 4.6: Luminescence spectra from a film deposited at T_{dep} = 460°C and r_{dep} = 0.3 μm/min and an acceleration voltage of 100 eV. Measurements with different slitwidths allow for the determination of low intensity peaks. In addition to the dominant P-lines the so-called N-lines, an other thermal donor, are identified at 0.745, 0.758, 0.761, and 0.772 eV. In these high resolution spectra the C-line splits up in a substructure of three lines.

resolution spectra the C-line around 0.790 eV splits up in three single lines.

At higher deposition temperature T_{dep} = 540°C the influence of the Si-ions on the defect luminescence is less pronounced as demonstrated in figure 4.7. Due to the higher temperature, no defect luminescence is observed for the samples deposited with V_{acc} = 20 and 100 V. However, the band to band luminescence (b-, c-, d-, and e-peak) decreases with increasing acceleration voltage indicating decreasing electronic quality of the films. Further increase of the acceleration voltage up to V_{acc} = 1000 V results in broad defect luminescence with a local peak around 0.8 eV.

Table 4.2 gives an overview of the defect peaks observed in MBE and IAD films deposited at T_{dep} = 460°C.

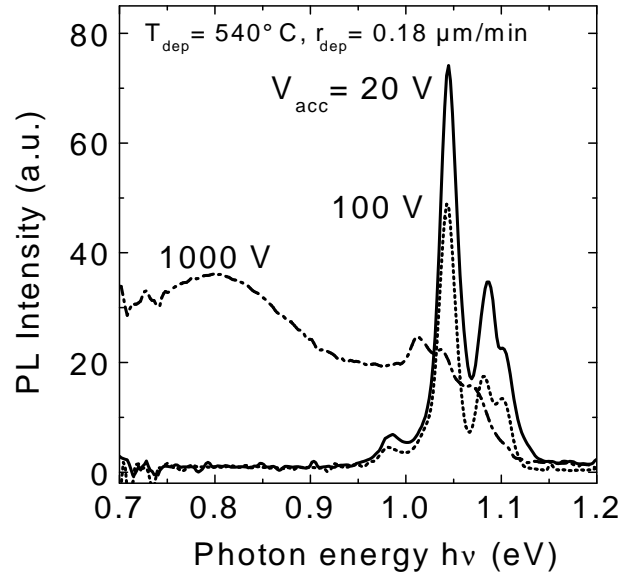*Figure 4.7: Influence of ion energy on the photoluminescence of silicon films deposited at $T_{dep} = 540°C$ and $r_{dep} = 0.18\,\mu m/min$. Due to the relative high deposition temperature no defect luminescence is observed for $V_{acc} = 20$ and 100 V, however, at $V_{acc} = 1000$ V broad defect luminescence occurs due to the high point defect density created by the high energy ions.*

4.2.3 Influence of deposition temperature and rate

Epitaxial growth of thin Si-films is mainly dominated by the adatom mobility on the surface. Hence, the deposition temperature is the key parameter in low temperature deposition. The influence of the deposition temperature on the photoluminescence of films deposited at 460, 550 and 650°C at $r_{dep} = 0.5\,\mu m/min$ is shown in figure 4.8. It can be seen that with increasing deposition temperature, the band to band luminescence also increases. At lower photon energies, only for the film deposited at $T_{dep} = 460°C$ the above mentioned P-line defect luminescence and the broad defect distribution around 0.8 eV is observed.

The dependence of the luminescence on the deposition rate for films deposited at $T_{dep} = 460°C$ is depicted in figure 4.9. At the highest rate $r_{dep} = 0.30\,\mu m/min$, the P-lines are observed, however, the a-peak is not present in the spectrum. The P-line luminescence

Table 4.2: Photoluminescence defect lines observed in a film deposited at $T_{dep} =$ 460°C, $r_{dep} = 0.3$ μm/min and an acceleration voltage of 100 eV see figure 4.6). The energetic positions match within $\pm$ 1 meV the literature values for the specific identified line.

no-phonon line	phonon replicas	name	occurs in	reference
	energy $h\nu$ (eV)			
0.767	0.749, 0.727, 0.708	P	IAD	[66,67,69]
0.792	0.789, 0.785	C	IAD	[64,65]
0.745	0.758, 0.761, 0.772	N	IAD	[63]
defect band	broad around 0.8		IAD and MBE films at low temperatures	
1.122		A	MBE	[81]

decreases with decreasing deposition while the intensity of the a-peak, as well of the broad defect band around 0.8 eV increase. Note that the lowest deposition rate shown here r_{dep} = 0.09 μm/min, equal to 15 Å/s, is still a very high rate for typical microelectronic MBE-applications which are carried out at deposition rates around 1 Å/s.

Thermal treatment

Films deposited at low temperatures 460°C $\leq T_{dep} \leq$ 510°C display defect lines known to originate from thermal donors. These defect lines are mainly the P-line defects, and to a lower extend the N-, and C-lines. Thermal donors are only observed in silicon that is rich in oxygen, carbon and/or nitrogen after a thermal treatment at temperatures in the range of the deposition temperatures used to deposit the present films. Results from literature (see chapter 2.2.3) show that thermal donor defects can be annealed out using a thermal treatment at higher temperatures. This also holds for the IAD films, as it is demonstrated in figure 4.10. After deposition at $T_{dep} = 460°$C the film shows P-line luminescence. After
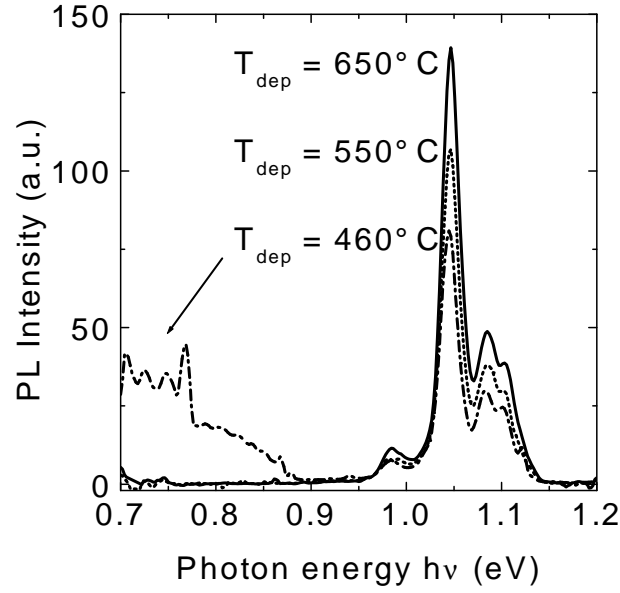
Figure 4.8: Dependence of the photoluminescence intensity on the deposition temperature of thin films deposited at 460, 550, and 650°C at r_{dep} = 0.5 µm/min. Band to band luminescence at photon energies above 1.0 eV increases with increasing deposition temperature. Broad defect luminescence at photon energies below 1.0 eV is only observed for films deposited at low deposition temperature T_{dep} = 460°C.

a thermal treatment for one hour at 650°C in nitrogen ambient, the P-lines disappear, instead, the intensity of the A-line at 1.122 eV increases. The luminescence of the other band to band transitions remains almost constant, as well as the defect band around 0.8 eV whose intensity only weakly decreases. The spectrum after heat treatment resembles that of a film deposited at low temperatures T_{dep} < 510°C by MBE, i.e., the broad peak around 0.8 eV is present without a significant signature of the thermal donor lines. However, this also indicates, that the defects responsible for the peak around 0.8 eV are not annealed out at 650°C after one hour, although this peak is normally not observed for films directly deposited at T_{dep} = 650°C with respective deposition times also below one hour.
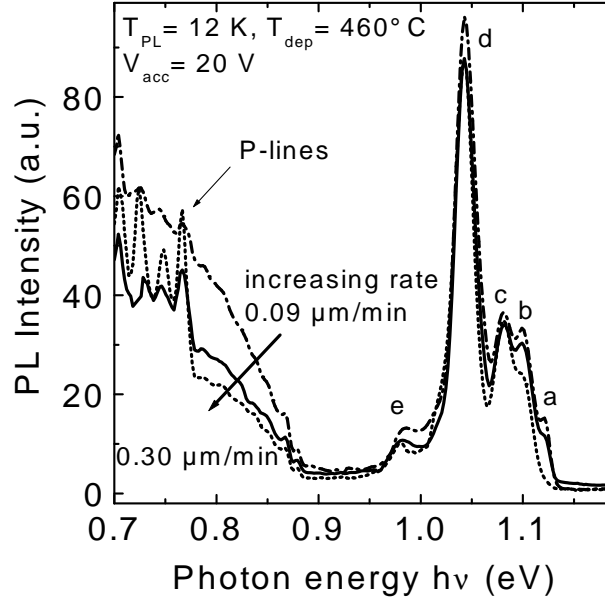
Figure 4.9: Photoluminescence spectra of films deposited at $T_{dep} = 460°C$ at various deposition rates $r_{dep} = 0.09, 0.12,$ and 0.30 μm/min. P-line luminescence is only observed for the films deposited at higher deposition rates 0.12 and 0.30 μm/min. In contrast, the intensity of the A-line at 1.122 eV and the intensity of the broad defect band around 0.8 eV increase with decreasing deposition rate. The intensity of band to band PL (b to e peaks) is nearly independent of the deposition rate.

4.2.4   Hydrogen passivation of defects

The effect of hydrogen treatment on the photoluminescence of a film deposited at T_{dep} = 460°C and r_{dep} = 0.16 μm/min is depicted in figure 4.11. After hydrogenation of the sample for 1 h at a temperature of 360°C using a microwave remote plasma, the P-line luminescence of the as-deposited film is no longer observable and the intensity of the bound exciton (BE^{TO}) has increased. Note, that this film is only weakly boron doped, in the range of $N_A = 1 \times 10^{15}$ cm^{-3}, and therefore the d-peak is less pronounced than in higher doped samples. The defect band around 0.8 eV is not influenced by the hydrogen treatment. In order to demonstrate that the change of the P-line luminescence is due to the hydrogenation, a spectrum of another sample from the same film is shown in figure 4.11, that is annealed in nitrogen ambient, using the same parameters as for the hydrogenation
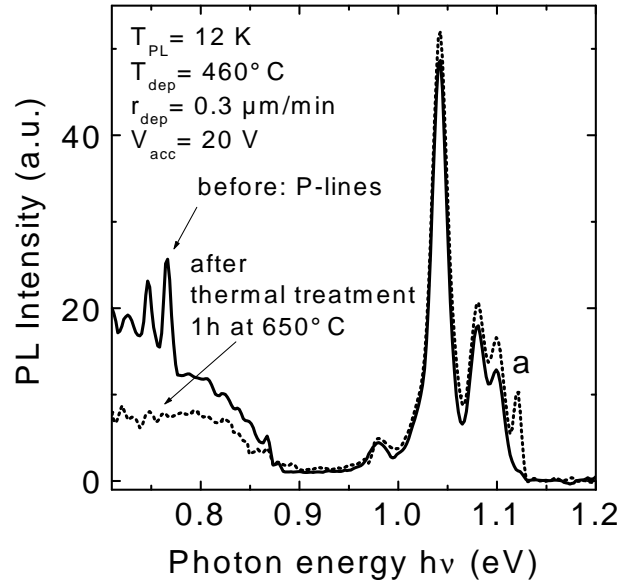
Figure 4.10: After a thermal treatment of a IAD deposited film the P-line luminescence below 0.792 eV is greatly reduced, instead the a-peak at 1.122 eV has risen. The spectrum now resembles to spectra of films deposited by MBE at otherwise unchanged deposition parameters. It is notable that the broad defect band around 0.8 eV is only weakly affected.

(duration: 1 h, $T_{anneal} = 360°C$). Here, no major differences are observed compared to the as-deposited film.

4.2.5 Discussion: Optically active defects

Three major features in the photoluminescence spectra of the low temperature films are distinguished: band to band luminescence for photon energies above 0.98 eV, a broad peak around 0.8 eV and the P, N, and C-lines below 0.8 eV. The results of the photoluminescence investigations are summarized in table 4.3 with the influence of deposition temperature, rate, and ion-bombardment on the intensity of the three features.
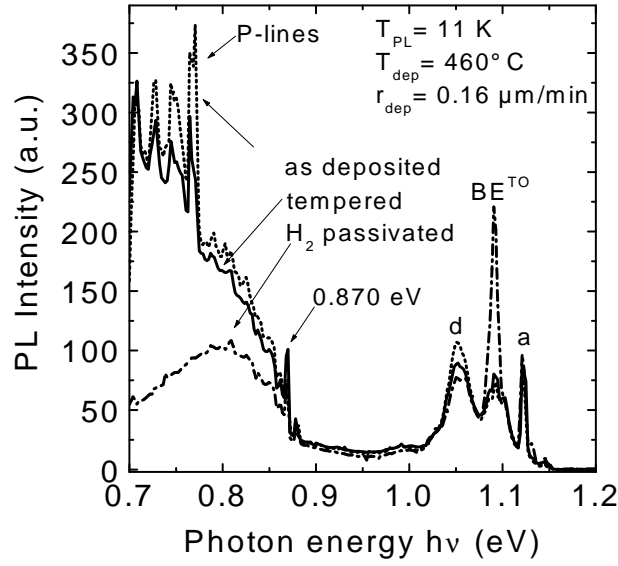
Figure 4.11: Hydrogenation of a film deposited at $T_{dep} = 460°C$ and $r_{dep} = 0.16$ μm/min passivates the P-line defects. Also shown is the photoluminescence of another sample of the same film after one hour annealing at $360°C$ in nitrogen ambient using the same thermal budget as for the hydrogenation. Here, only minor differences to the as-deposited film are detected, thus verifying that hydrogen is responsible for the defect passivation.

Band to band luminescence

A clear identification of the b-, c-, d-, and e-peaks is difficult. They decrease very similarly with increasing PL-measurement-temperature. It is noted, that the intensity of these lines did not show pronounced dependence on the power of the excitation laser light, which excludes electron hole droplet (EHD) formation. In the case of doped films with doping levels above 1×10^{15} cm^{-3}, the d-peak (luminescence around 1.04 eV) is the most prominent line. The intensity of the d-peak depends on the film doping: Intrinsic films, i.e. films deposited without additional P- or B-doping, do not show pronounced intensity around 1.04 eV, while the intensity of this line increases with increasing doping concentration. This is consistent with investigations of Eswaran *et al.*, where a band structure around 1.045 eV was detected in photoluminescence measurements of highly phosphorus doped

Table 4.3: *Major photoluminescence features of low temperature epitaxial films. The photon energy $h\nu$ and the dependence of the PL intensity of the features on the (increasing) deposition temperature T_{dep}, the (increasing) deposition rate r_{dep}, and the ion-bombardment with low energy ions $V_{acc} \leq 100$ V is given.*

PL feature	PL energy $h\nu$	T_{dep}	r_{dep}	ion-bombardment
0.8 eV peak	around 0.8 eV	only 460°C	decreases	weak influence
P, N, and C-line	< 0.8 eV	only 460°C	sharper lines	only in IAD
band to band	> 0.98 eV	increases	no influence	weak increase

silicon [143]. These broad lines appear even at high deposition temperatures of 810°C. Hence, they are more likely a result of the dopant impurities and seem to be related to multiple excitons bound at dopant impurity centers than related to point defects formed by imperfect growth. The electronic quality of the films correlates with the intensity of these lines which supports the thesis that these lines are related to band to band recombination in the case of doped epitaxial films. The use of accelerated ions with $V_{acc} = 20$ weakly increases the intensity of the d-peak. However, the d-peak intensity decreases for $V_{acc} \geq 100$ V. The complex Q- and S-lines, together with their splitting under stress might explain the broad features of the observed b-, c-, and d-peaks as well [73]. However, the Q- and S-lines are only observed in lithium doped films and SIMS measurements did not show lithium in the IAD-films.

Strong A-line PL (a-peak) at 1.122 eV is found in MBE-films, whereas the A-line is suppressed or much weaker when IAD with ion energies of 20 eV or above is used and the deposition rate is above 0.1 μm/min. Luminescence at 1.122 eV was also reported by Weber *et al.* [81]. The authors speculated that the origin of the center is an isoelectric trap where carbon is involved. Isoelectric defects are impurity atoms or clusters, that have the same electronic configuration as the host lattice. For example Ge in Si, where the strain is responsible for the trapping of carriers.

0.8 eV peak

The broad defect band around 0.8 eV may result from imperfect growth at low deposition temperatures, as demonstrated by the temperature dependent PL-measurements in figure 4.8. From similar experiments, not shown in this work, it is obvious that the peak does not appear in the spectra obtained from films deposited at $T_{dep} \geq 510°$C. Nevertheless, the defect band remains even after a 1 h heat treatment at 650°C, and after hydrogen treatment for 1 h at 360°C. A possible explanation for the formation of this defect band is the presence of stress in the films, that can result in such broad luminescence features. A broad peak around 0.8 eV in photoluminescence was observed in silicon samples implanted with either hydrogen or oxygen after a hydrostatic argon ambient pressure treatment with up to 1.5 GPa [83]. The applied stress enhances the emission of the defect luminescence, whereby the origin of the luminescent recombination remains unclear. A similar defect band around 0.8 eV, additional to the D-lines from dislocations, was observed by Mudryi *et al* in multicrystalline silicon for solar cell applications [82]. From the PL measurements the stress in the samples was determined to values around 10 MPa. The band was attributed to gettering of impurities such as carbon and oxygen or self interstitials forming during growth. Additionally, such a broad defect band around 0.8 eV is observed in silicon films deposited at $T_{dep} = 800°$C by LPCVD on strained Si-buffer layers [80]. However, Raman-spectroscopy investigations of IAD-films deposited at $T_{dep} = 460°$C did not reveal stress in the films within the accuracy of the method, which is of the order of $\pm$ 15 MPa.

P, N, and C-line luminescence

The use of accelerated Si ions in the beam is responsible for the formation of thermal donors in films deposited at temperatures around $T_{dep} = 460°$C. This is confirmed by the exactly matching energetic positions of the observed P-, N- and C-lines with literature data, as well as the characteristic annealing of these lines at temperatures of 650°C.

The most intense of these lines in the PL spectra are the P-lines (see page 17). Their intensity increases with increasing ion energy. The N- and C-lines are observed in high resolution spectra as well, albeit with lower intensity. In the literature, these PL lines

are only reported from Si samples which have a high density of either oxygen, carbon or nitrogen, such as CZ-silicon wafers. The formation of complexes with vacancies and/or Si self-interstitials from these impurities is responsible for the observed defect luminescence. Although the concentration of these impurities in films deposited by IAD is below the detection limit of our SIMS-machine, (O^+ 5×10^{18} cm^{-3} [144], C^+ 1.1×10^{18} cm^{-3}, N^+ 1.0×10^{19} cm^{-3} [145]), the defect lines in the PL measurements are most likely caused by these impurities. The occurrence of the sharp P-lines depends on the deposition rate. Only for films deposited with $r_{dep} > 0.1$ μm/min they are clearly observed. At lower deposition rates, the sharp P-lines smear out together with the peak around 0.8 eV into a broad defect distribution below 0,9 eV. A hydrogen passivation treatment at only 350°C results in a significant decrease of the luminescence intensity of the lines from these thermal donors.

4.3 Deep level defects

4.3.1 Defect-bands

The DLTS-spectra of low temperature epitaxial films typically consist of relatively broad overlapping peaks, as depicted in figure 4.12a) for a film deposited at $T_{dep} = 460$°C and r_{dep} = 0.16 μm/min. The film has a low boron doping concentration of $N_A \approx 5 \times 10^{15}$ cm^{-3}. The maxima of the DLTS spectra correspond to majority-carrier traps for the chosen representation, i.e. in this case of a p-type film the peaks A, B, and C represent hole-traps. Minority-carrier traps would appear as minima in the spectra. Each peak corresponds to a distinct defect level. Several spectra recorded at different emission frequencies e_p are used to determine the energetic levels of the defects in the films by plotting the emission frequency versus the inverse sample temperature at the peak maximum in an Arrhenius graph (see figure 4.12b)). Analysis of the three peak maxima is made by fitting Gaussian profiles to the DLTS spectra. The energetic levels of the defects obtained by this method are $E_t - E_V$ = 214 meV $\pm$ 16 meV (A), 412 meV $\pm$ 53 meV (B), and 330 meV $\pm$ 6 meV (C). The given error of the measurement is the error of the linear fit. Obviously, the
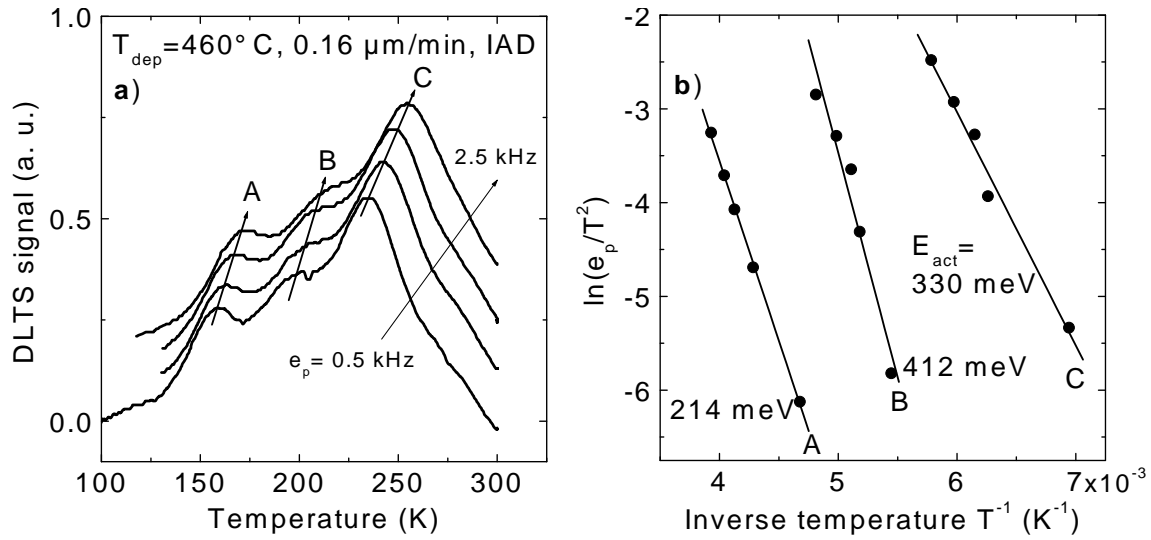
Figure 4.12: a) DLTS-spectra of a p-type sample, recorded at various repetition frequencies e_p. The spectra show three broad, overlapping peaks, representing broad defect distributions in the band gap. For analysis, the temperature of the peak maxima is determined by Gaussian curve fits. b) The Arrhenius plot of the emission frequency e_p versus the inverse temperature of the maxima A, B, and C from a) reveals the defect levels of $E_t - E_V = 214$ meV (A), 412 meV (B), and 330 meV (C).

overlapping of the peaks complicates the determination of the defect level corresponding to peak B, as expressed by the significantly larger error.

An example of an n-type epitaxial film is given in figure 4.13a). The spectrum is normalized to the corresponding defect density. As before, positive peaks are due to majority carrier traps, in this case electron traps. The analysis of the DLTS spectrum reveals an energetic level of peak X of $E_C - E_t = 136$ meV, as represented in figure 4.13b). Although two more peaks Y and Z are visible in this spectrum, their peak position is not clearly detectable for other repetition frequencies, and therefore the energetic position cannot be determined. In other n-type samples only the peak X, at approximately the same temperature and with similar energetic position is detected. The level of 136 meV is in good
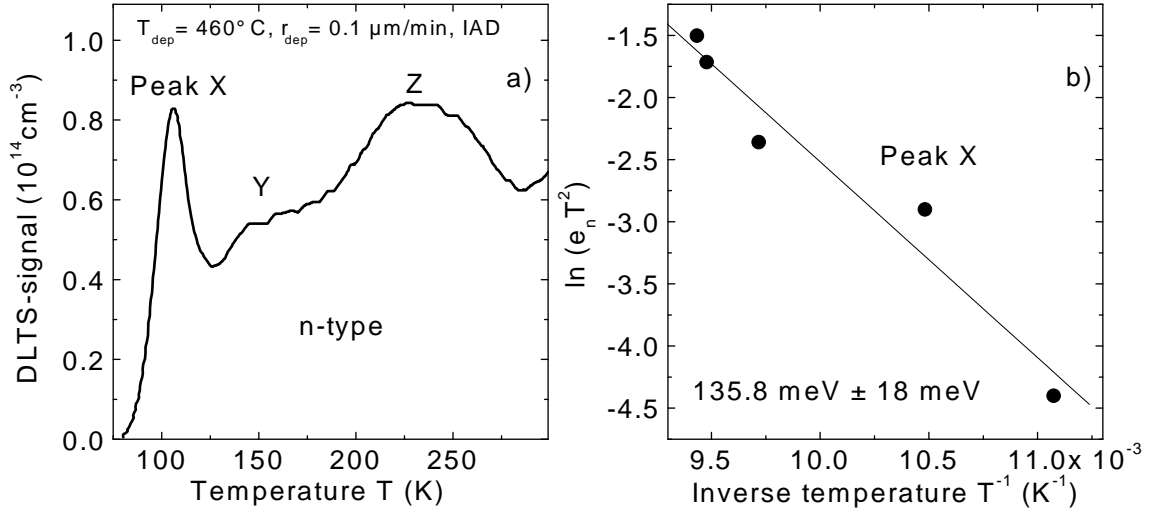
Figure 4.13: a) DLTS-spectrum of an n-type sample. The spectrum is normalized to the defect concentration, and shows a broad defect distribution. b) The Arrhenius plot of the emission frequency e_n versus the inverse temperature of peak X reveals a defect level at $E_C - E_t = 136$ meV. The energetic levels of peaks Y and Z cannot be derived from the spectra.

agreement with values reported in literature for thermal donors in n-type oxygen rich silicon [87,88].

Figure 4.14 summarizes data from DLTS analysis of seven films deposited by IAD (no. 1 to 6) and MBE (no. 7). All films are deposited at $T_{dep} = 460°$C, however, the deposition rate varied in the range of $r_{dep} = 0.1 \ldots 0.5$ μm/min. Note that the DLTS-spectra of all samples show several peaks and that only those that were undoubtedly determined are shown here. Consequently, only very few data points are available. From the available data, defect bands around 120, 200, 250, 350, and 430 meV are deduced. The distinction between the 200 and 250 meV bands is motivated by the data of samples 3 and 4, where two levels in this energy range are found. However, for the 350 and 430 meV bands it is not obvious if there are two bands or only discrete levels, and the suggested assignment to defect bands is only tentative.
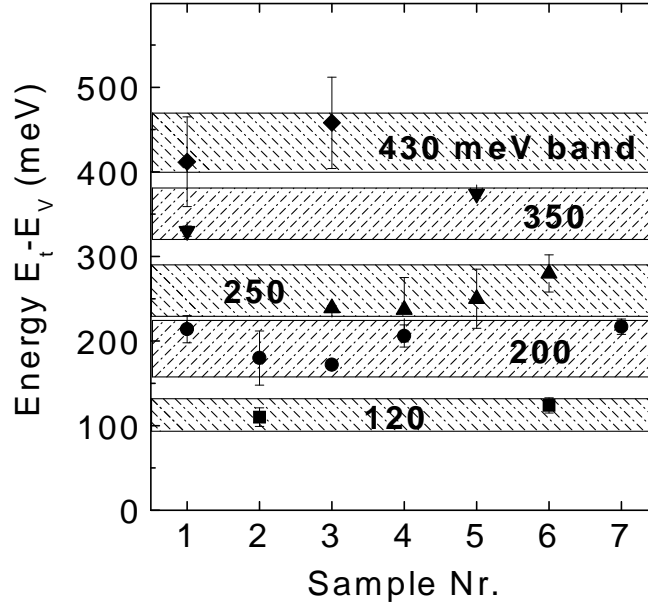
Figure 4.14: Tentative representation of the defect bands in the lower half of the band gap of low temperature epitaxial Si-films. All films are deposited at $T_{dep} = 460°C$ by IAD except for sample no. 7 that is deposited by MBE.

4.3.2   Influence of deposition temperature, rate, and silicon ions

Deposition temperature

Similar to the results from photoluminescence measurements, defect levels were only found in films deposited at $T_{dep} = 460°C$, whereas for higher deposition temperatures $T_{dep} \geq 510°C$ no peaks in the DLTS-spectra are observed. Hence, the defect concentration for films deposited at higher temperatures is below the detection limit of the DLTS-method, which is about 1×10^{13} cm^{-3} for p-type films. A method for the estimation of the defect density from the minority carrier diffusion length of films deposited at $T_{dep} \geq 460°C$ is given in chapter 5.3. There it is found that the defect density decays exponentially with the deposition temperature.

Deposition rate

Figure 4.15 shows the influence of the deposition rate on the deep level defects. Two strong peaks are found for the film deposited at $r_{dep} = 0.12$ μm/min, labeled B and D. These two peaks are still present in the spectrum of the film deposited at $r_{dep} = 0.36$ μm/min, albeit to a much lower extent. The peaks labeled A and C, clearly visible for the higher deposition rate are barely visible for films deposited at the lower deposition rate.
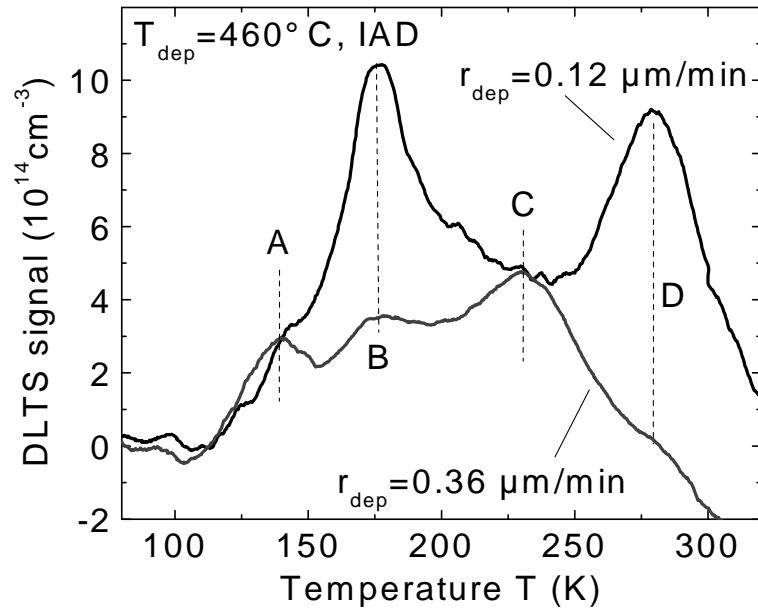

Figure 4.15: Dependence of the DLTS spectra on the deposition rate. Peak B of the film deposited at 0.12 μm/min corresponds to a defect level of $E_t - E_V = 250$ meV and peak D to 374 meV. The density of these two defect levels decreases significantly when the deposition rate is increased to 0.36 μm/min, whereas the peak A of the film deposited at 0.36 μm/min corresponding to $E_t - E_V = 124$ meV and peak C (274 meV) are only weakly affected.

Influence of Si ions

Figure 4.16 depicts the variation of the DLTS spectra when films deposited by IAD are compared to those deposited by MBE. The film grown under Si-ion-bombardment with

$V_{acc} = 20$ V (IAD) shows a higher total intensity of the DLTS signal. In particular the peak C is increased by the use of the Si-ions. Also the peak shape is sharper as that of the MBE-film. In the case of MBE the defect distribution is smeared out, and defect identification becomes difficult. Peak A of the MBE-film corresponds to an energy of 217 meV, peak A and peak C of the IAD-film to 124 meV and 274 meV, respectively.
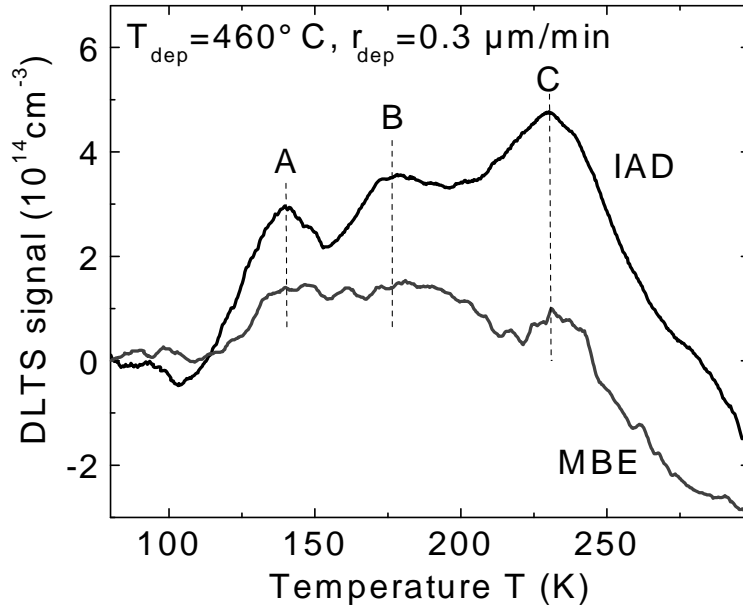

Figure 4.16: Influence of accelerated silicon ions with acceleration voltage $V_{acc} = 20$ V on the DLTS spectra. The defect density is increased by more than a factor of 2 by the use of silicon ions in the beam.

4.3.3 Discussion: Deep level defects

In general, the DLTS spectra of films deposited at $T_{dep} = 460°$C consist of several broad, overlapping peaks. This often hampers the identification of all defect levels present in a single film. The compiled data of defect levels of seven p-type films reveals, that in the lower half of the band gap, a variety of defect levels, or more likely defect bands, are present. The density of each defect level in a single film depends on the deposition rate and the use of accelerated Si-ions. An increase of the deposition rate results in less

pronounced peaks in the DLTS experiments. The use of accelerated Si-ions results in increased density of the trap levels in the DLTS spectra. However, the density of all peaks present in the film is increased, whereas in the PL experiments only the P-lines increased upon increased Si-ion energy. From this results, no clear correlation of the photoluminescence and DLTS results could be established. The n-type samples deposited by IAD typically show a shallow defect level around 0.136 eV below the conduction band. This is in the range of DLTS results for thermal donors reported in literature, where 16 different species with energy levels between $E_C - 0.07$ eV and $E_C - 0.15$ eV are observed [87,88]. Transition metal impurities, such as Cu, Ni, or Fe are known to generate defect levels in the band gap, some of them in the range of the defect bands determined by DLTS in the epitaxial films investigated here [96,146,147]. However, the reported DLTS signals for metallic impurities are much sharper, and the observed dependence of the defect density on the deposition temperature of the films remains unclear. Additionally, dislocations decorated with transition metals show typical D-line luminescence [58,59,148], which is not observed in the epitaxial films, even for dislocation densities up to 1×10^7 cm^{-2}.

4.4 Correlation of carrier lifetime and defect density

4.4.1 Influence of deposition temperature and rate

Test solar cell structures were fabricated to determine the minority carrier diffusion length in the films. Measurements of the internal quantum efficiency allow for the evaluation of the minority carrier diffusion length L, a key parameter for the characterization of the electronic quality of films for solar cell applications. The minority carrier diffusion length L is correlated with the carrier lifetime τ via the diffusion constant D by $L = \sqrt{D\tau}$, and is a direct measure of the electronic quality of the films.

Figure 4.17 shows the dependence of L on the deposition temperature and rate of films deposited by IAD with $V_{acc} = 20$ V. At low temperatures $T_{dep} \leq 510°$C L has a maximum at a deposition rate around $r_{dep} = 0.3$ μm/min. At higher deposition temperatures the
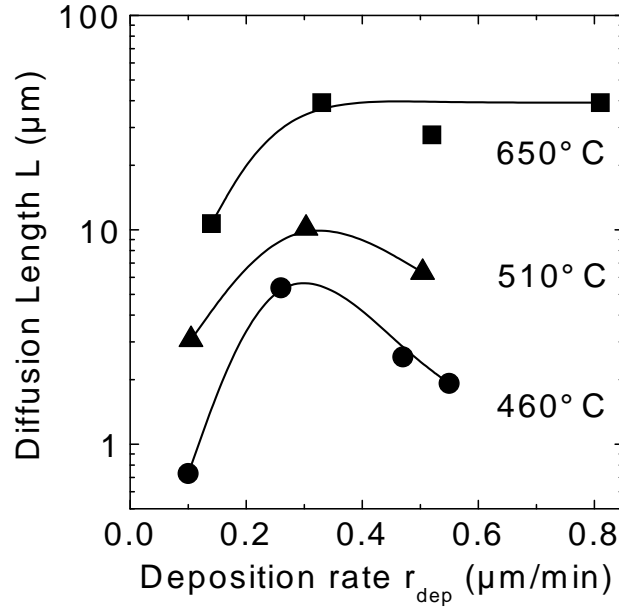
Figure 4.17: Minority carrier diffusion length L as determined by IQE-measurements for films deposited at T_{dep} = 460, 510, and 650°C by IAD. At low temperatures $T_{dep} \leq 510°C$ the diffusion length L has a maximum at a deposition rate $r_{dep} \approx 0.3$ μm/min. At higher deposition temperatures the diffusion length remains at a high value of L $\approx$ 40 μm, even for rates exceeding r_{dep} = 0.3 μm/min. After [7].

diffusion length remains almost constant at a high value of $L \approx 40$ μm, even for rates exceeding $r_{dep} = 0.3$ μm/min, demonstrating the high electronic quality of the epitaxial films.

Figure 4.18 shows the correlation between the diffusion length and the trap density as determined by DLTS as a function of the deposition rate for films deposited at $T_{dep} = 460°C$. The given trap density is the maximum of the peak of the respective defect level in the range of the 200 meV band. All three data points show the highest defect density in their respective DLTS-spectrum. It is found that the maximum of L at ≈ 0.3 μm/min correlates with a minimum in the defect density at approximately the same deposition rate. A possible explanation of this behavior is an interplay of two defect generating mechanisms that depend on the deposition rate during epitaxial growth [149]. On the one hand, the incorporation probability of impurities from the gas phase is the higher the
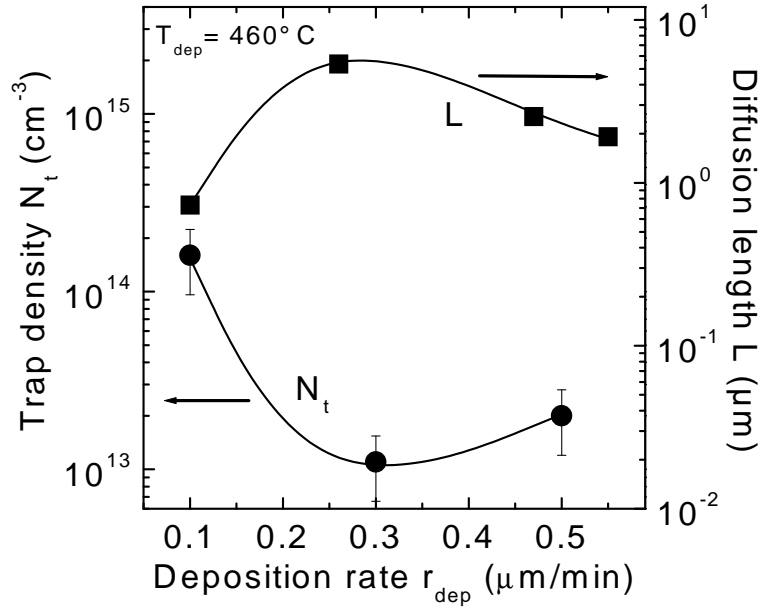
Figure 4.18: Density of point defects and point defect complexes N_t as determined by DLTS and minority carrier diffusion length L of films deposited at $T_{dep} = 460°C$ in dependence of the deposition rate r_{dep}. The diffusion length is determined by the presence of point defects as indicated by the correlation of the minimum of N_t and the maximum of L at deposition rates around $r_{dep} = 0.3$ μm/min. The lines are a guide to the eye.

lower the deposition rate. Thus, films deposited with low deposition rates should show a higher amount of impurities. On the other hand, a high deposition rate reduces the mean free time of the adatoms on the wafer surface, resulting in a higher amount of vacancies and interstitials due to imperfect growth. The latter effect becomes less pronounced at higher deposition temperatures as demonstrated by the curve of the films deposited at $T_{dep} = 650°C$ shown in figure 4.17.

4.4.2 Benefits from accelerated silicon ions

Photoluminescence and DLTS investigations (see chapter 4.2.2 and 4.3.2) have shown, that even moderately accelerated Si-ions with $V_{acc} = 20$ V used during deposition of thin films at low deposition temperatures generate additional defects and increase the

defect density. In this chapter, the influence of the Si-ions on the electronic properties will be studied. Figure 4.19 depicts the dependence of the minority carrier diffusion length L on the acceleration voltage of the Si-ions during deposition at temperatures of T_{dep} = 460°C and 650°C with r_{dep} = 0.3 μm/min for both series. The case of V_{acc} = 0 V corresponds to standard MBE-deposition conditions with grounded substrate. At both deposition temperatures, an increase of the diffusion length with the acceleration voltage is observed.
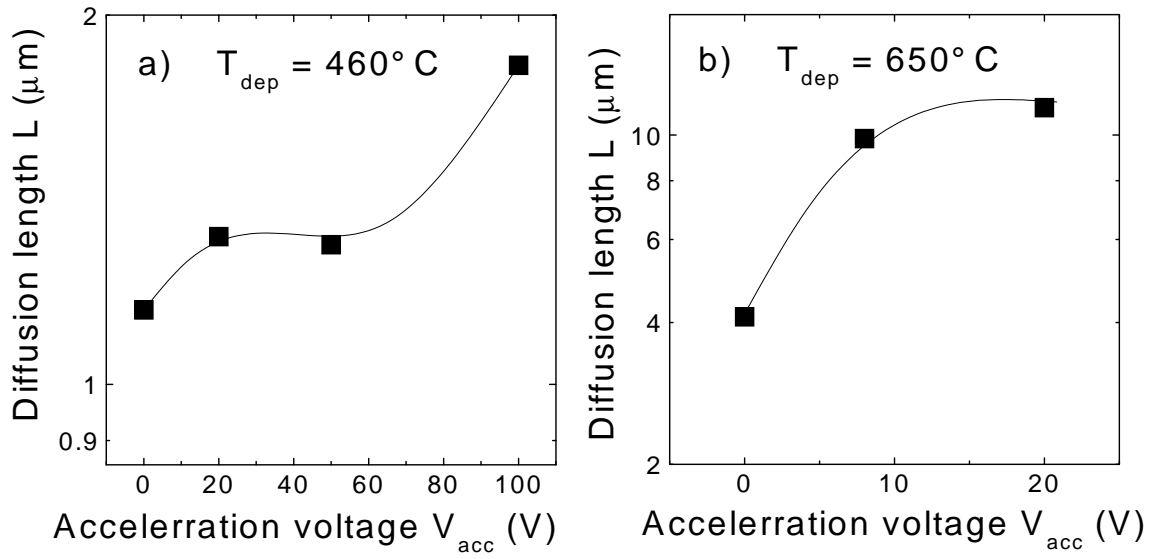
Figure 4.19: Films deposited at a) $T_{dep} = 460°C$ and b) $T_{dep} = 650°C$ with $r_{dep} = 0.3$ μm/min show an increase of the minority carrier diffusion length with increased acceleration voltage.

At T_{dep} = 460°C (figure 4.19a), L increases from 1.15 μm to values around 1.3 μm for applied acceleration voltages of V_{acc} = 20 and 50 V. Further increase of V_{acc} to 100 V results in L = 1,82 μm. This result is in good agreement with the photoluminescence experiments shown in figure 4.5. Although the PL experiments show increased P-line defect density with increased acceleration voltage, the band to band luminescence (peaks B through E), a measure for the electronic quality, also increases.

For the film deposited at T_{dep} = 650°C, displayed in figure 4.19b), L increases from 4.1 μm to 11.4 μm upon increase of V_{acc} from 0 to 20 V. In this series of depositions, no ex-

periments with higher V_{acc} were carried out. However, results from literature on ion-beam deposition [13] and the intensity of the band to band luminescence of experiments with higher acceleration voltages above $V_{acc} = 20$ V, shown in figure 4.7, allow the conclusion, that the electronic quality of films deposited at $T_{dep} = 650°$C decreases for acceleration voltages higher than $V_{acc} \approx 20$ V.

Two test solar cells, deposited at $T_{dep} = 750°$C under MBE and IAD ($V_{acc} = 20$ V) conditions, respectively, show the same conversion efficiency of $\eta = 13.8$ %. The minority carrier diffusion length of these films, obtained by the analysis of the IQE, exceeds in both cases the film thickness of 15 μm and is of the order of $L = 30 \ldots 40$ μm. Therefore, at this relatively high deposition temperature of $T_{dep} = 750°$C, no significant effect of the accelerated Si-ions could be deduced experimentally.

4.5 Discussion: Defect formation in low temperature epitaxy

The photoluminescence and DLTS results presented in this chapter showed a variety of defects in IAD and MBE films deposited at low temperatures. It has to be emphasized here again, that both analysis methods reveal a significant dependence of the point defect density on the deposition temperature. Chapter 5.3 shows that the temperature dependence of the defect density determined from the minority carrier diffusion length of the films exhibits an exponential decay of the defect density with the deposition temperature. Hence, when discussing the defect formation during molecular beam epitaxy, we have to look for defect formation mechanisms, that depend on temperature. These are (i) the adatom mobility, (ii) sticking coefficient of impurities during deposition, and (iii) temperature dependent complex formation, e.g. thermal donors and interstitial defect reactions.

As has been pointed out in chapter 2.1.3, the adatom mobility is clearly one of the dominating parameters for the evolution of film morphology during low temperature epitaxy. The number of structural defects and especially for (100)-oriented films deposited above $T_{dep} = 450°$C the number of vacancies due to imperfect epitaxial growth decreases

with increasing deposition temperature. Surface roughening, e.g. hillocks and ripples are observed even in step flow growth mode at deposition temperatures up to 625°C [27].

The sticking coefficient of impurities generally depends on the coverage and the temperature [150]. Carbon and oxygen related surface adsorbates desorb at temperatures above 1200°C [151] and 850°C [152], respectively. It has to be mentioned here, that the base pressure of the MBE reactor used for this investigations of 1×10^{-9} mbar is about one order of magnitude higher than reported for other MBE-systems. Especially during deposition with high deposition rates the pressure attains values around 1×10^{-7} mbar, where the main species are hydrogen, and to a lesser extend nitrogen. However, for long deposition durations, oxygen and carbon related mass signals are observed in the residual gas by the mass spectrum analyzer. No experimental proof of other impurities, apart from oxygen, carbon, nitrogen and the dopants boron and phosphorus, are observed in the films investigated in this work within the resolution limits of residual gas analysis and SIMS measurements. Hence there is a high probability that the films deposited at low temperatures contain oxygen, carbon, and nitrogen as impurities. Other impurities may be incorporated as well, however there is no direct proof of their presence in the films. As the impinging rate of impurities depends on the partial pressure in the residual gas [153], it is expected, that the density of impurity atoms is inversely proportional to the Si-deposition rate. This hypothesis is confirmed by the results shown in figure 4.18: the diffusion length L increases and the defect density N_t deceases with rising deposition rate for $r_{dep} = 0.1 \ldots 0.3$ μm/min. However, at low deposition temperatures $T_{dep} \leq 510$°C and deposition rates above $r_{dep} = 0.3$ μm/min, the increasing number of defects generated by imperfect growth dominates [149].

The sheer existence of impurities such as oxygen, carbon or nitrogen does not necessarily result in the formation of electrically active complexes. This depends to a great extend on the presence of vacancies and silicon self interstitials, and the temperature treatment of the samples, as demonstrated by numerous investigations on thermal donors and new oxygen donors in CZ-silicon (see chapter 2.2.3). The temperature and passivation characteristics of the observed P, N, and C-line luminescence demonstrate, that these impurities

are active in the films.

Chapter 2.1.2 presents the principle interactions of low-energy ions with the surface of the growing crystal. Experimentally, the comparison of films deposited by IAD and MBE shows, that the additional vacancies, that are created by irradiation with ion energies above 20 eV enhance the formation of thermal donors correlated to P-line luminescence.

As the intensity of the 0.8 eV peak, observed in PL experiments, decreases by the use of accelerated Si-ions, it seems not to be related to the vacancy density. The 0.8 eV peak also is not correlated to the density of extended defects, as this peak is observed in films with structural densities ranging from $n_{ep} = 1 \times 10^3 \text{cm}^{-2}$ to $1 \times 10^6 \text{ cm}^{-2}$. Similar PL-peaks are reported in literature from bulk silicon under stress [82,83] or epitaxial films deposited on strained substrates [80]. Therefore, the 0.8 eV peak might be a result of strain in the films, that is due to imperfect growth at low deposition temperatures.

Despite the increased defect density observed by PL and DLTS in films deposited by IAD, the minority carrier diffusion length L of those films also increases. A possible explanation of the increasing L with increasing ion energy is a gettering effect of carbon and oxygen to the newly created vacancies. The TQE measurements of chapter 5 show, that rather shallow defect levels in the range of 0.16 to 0.21 eV are the dominant recombination centers at room temperature. The respective defect might be a center where oxygen and carbon are involved as well. If additional vacancies are generated by the use of Si-ions, these might act as gettering centers for oxygen and carbon and form thermal donors that are less active recombination centers, and therefore the total recombination is reduced.

Chapter 5

Temperature dependent quantum efficiency – TQE

The investigations of defects in (100)-oriented epitaxial thin films deposited at low temperatures $T_{dep} \leq 650°C$ presented in chapter 4 revealed the presence of a variety of defect levels in the band gap. Photoluminescence as well as DLTS give results on the energetic position of those defect levels, however, they do not allow for an identification of the recombination activity, i.e. the capture of an electron *and* a hole in the defect level. The tailoring of devices requires the analysis of the dominant recombination center in the material under working conditions. As the minority carrier lifetime is the key parameter for solar cell applications, lifetime spectroscopy (LS), i.e., the measurement of the lifetime under varied measurement temperature or injection level, allows for a determination of the dominant recombination centers. However, the conventional measurement techniques for the lifetime, microwave photoconductance decay (MWPCD) and quasi steady state photoconductance (QSSPC) cannot be applied to thin films or processed devices. Therefore, a new method for the temperature dependent extraction of the lifetime that is compatible with thin film solar cells was developed in this work.

In this chapter, first the principles of lifetime spectroscopy are discussed. Subsequently, this chapter introduces temperature dependent quantum efficiency (TQE) measurements as a new lifetime spectroscopy method for completed devices. At the end of the chapter,

TQE is applied to IAD-thin film solar cells and a model for the analysis of the data is developed.

5.1 Lifetime spectroscopy

The major disadvantage of defect analysis methods such as DLTS and photoluminescence is given by the fact, that they do not give clear evidence for the dominating recombination mechanism that leads to device degradation under working conditions. In contrast, the minority carrier lifetime τ is a direct measure of the total recombination process, i.e. the capture of an electron and the capture of a hole in the trap, and analysis of τ using methods that analyse the minority carrier lifetime as a function of temperature (temperature dependent lifetime spectroscopy, TDLS) [154,155] or injection level (injection dependent lifetime spectroscopy, IDLS) [156] allow for the determination of the energetic level of the dominant defects with a high sensitivity. The combination of both, TDLS and IDLS, reveals most of the relevant parameters of the recombination center, such as energetic position, defect density, and capture cross section [157,158].

The analysis of the measured IDLS and TDLS data is based on the Shockley-Read-Hall theory for a single defect level with energy E_t [102,103]. The Shockley-Read-Hall lifetime τ_{SRH} under the assumption that the electron and hole excess carrier densities are equal: $\Delta n = \Delta p$ is given by

$$\tau_{SRH} = \frac{\tau_{n0}(p_0 + p_1 + \Delta n) + \tau_{p0}(n_0 + n_1 + \Delta n)}{p_0 + n_0 + \Delta n}, \tag{5.1}$$

where τ_{n0} and τ_{p0} are the capture time constants and n_0 and p_0 are the equilibrium densities of electrons and holes, respectively. The SRH-densities n_1 and p_1 are given by

$$n_1 = N_C \exp\left(-\frac{E_C - E_t}{k_B T}\right), p_1 = N_V \exp\left(-\frac{E_t - E_V}{k_B T}\right), \tag{5.2}$$

where N_C and N_V are the effective densities of states of the conduction and valence band and E_C and E_V the energies of the conduction and valence band edge, respectively.

In the case of IDLS, the excess carrier density Δn is varied over several orders of

magnitude by light generated electron-hole pairs, and the variation of the SRH-lifetime with Δn is studied.

The analysis of the TDLS will be discussed here in more detail with several simplifications of the SRH-lifetime for the application to p-type silicon films under low injection conditions. Under low level injection (LLI: $\Delta n \ll n_0 + p_0$) the SRH-lifetime simplifies to

$$\tau_{SRH}^{LLI} = \frac{\tau_{n0}(p_0 + p_1) + \tau_{p0}(n_0 + n_1)}{p_0 + n_0}, \tag{5.3}$$

and in the case of a p-type semiconductor ($p_0 \gg n_0$):

$$\tau_{SRH}^{LLI,p} = \frac{\tau_{n0}(p_0 + p_1) + \tau_{p0}n_1}{p_0}. \tag{5.4}$$

At low temperatures, i.e. $p_1 \ll p_0$ and $n_1 \ll p_0$ equation 5.4 yields $\tau_{SRH}^{LLI,p} = \tau_{n0}$ and $\tau_{SRH}^{LLI,p}$ is only slightly temperature dependent via the temperature dependence of the thermal velocity $v_{th}(T) = \sqrt{8kT/\pi m_{tc}^*}$ where m_{tc}^* is the thermal velocity effective mass [159]. Assuming the capture cross section σ_n to be independent of the temperature, the capture time constant τ_{n0} becomes

$$\tau_{n0}(T) = \frac{1}{N_t \sigma_n v_{th}(T)} = \theta^{-1/2} \tau_{n0}^{300K}. \tag{5.5}$$

Using the normalized temperature $\theta = T/300K$ allows to eliminate the temperature dependence in τ_{n0} and refer to a temperature invariant reference lifetime τ_{n0}^{300K}.

At elevated temperatures either p_1 or n_1 dominates equation 5.4, and $\tau_{SRH}^{LLI,p}$ becomes thermally activated with either $E_a = E_t - E_V$ (case A, defect in the lower half of the band gap) or $E_a = E_C - E_t$ (case B, defect in the upper half of the band gap). Under consideration of the temperature dependence of the effective densities of states $N_{C/V}(T) = \theta^{3/2} N_{C/V}^{300K}$ [160], equation 5.4 can be rewritten by

$$\tau_{SRH}^{LLI,p} = \theta \tau_{n0}^{300K} \left[\theta^{-3/2} + \kappa \exp(-E_a/k_B T) \right], \tag{5.6}$$

where either $\kappa = N_V^{300K}/N_A$ (case A) or $\kappa = \tau_{p0}^{300K} N_C^{300K}/(\tau_{n0}^{300K} N_A)$ (case B).

As a consequence, the temperature dependent SRH-lifetime $\tau_{SRH}^{LLI,p}(T)$ only depends on the activation energy E_a, the capture time constant τ_{n0}, and in case B on the ratio

$\tau_{p0}^{300K}/\tau_{n0}^{300K}$. Figure 5.1 depicts the influence of the activation energy E_a of a single re-combination center in the lower half of the band gap (case A) on the lifetime $\tau_{SRH}^{LLI,p}$ scaled by the normalized temperature θ in an Arrhenius representation for simulated data with $p_0 = N_A = 1 \times 10^{16}$ cm^{-3} and $\tau_{n0} = 1$ μs. In the Arrhenius representation, the slope of the scaled lifetime in the high temperature regime is determined by the activation energy only. With increased E_a, the minimum of $\tau_{SRH}^{LLI,p}/\theta$ moves to higher temperatures. The low temperature regime of $\tau_{SRH}^{LLI,p}/\theta$ is a direct measure of the reference lifetime τ_{n0}^{300K}. If the defect level is in the upper half of the band gap (case B), the minimum of $\tau_{SRH}^{LLI,p}/\theta$ would be shifted additionally if $\tau_{p0}^{300K}/\tau_{n0}^{300K} \neq 1$, while the slope at high temperatures and the low temperature regime won't be affected. In the case of $\tau_{p0}^{300K}/\tau_{n0}^{300K} = 1$, a defect level in the upper half could not be distinguished from a defect level in the lower half by means of temperature dependent lifetime spectroscopy.

Rein *et al.* [158] gave an overview of the possibilities and restrictions of lifetime spectroscopy for defect analysis. The higher the activation energy and the higher the doping density, the higher is the temperature at which the minimum of $\tau_{SRH}^{LLI,p}/\theta$ occurs. This may be inconvenient if the measurement setup or the device under investigation are not compatible with high temperatures. As mentioned above, only for $\tau_{p0}^{300K}/\tau_{n0}^{300K} \neq 1$ the conclusion that the trap level is located in the upper half of band gap is possible. If $\tau_{p0}^{300K}/\tau_{n0}^{300K} = 1$, the unambiguous determination whether the defect level is in the upper or lower half of the band gap is not possible by TDLS alone. Here additional information, e.g. from IDLS or DLTS measurements, is necessary.

Dominant recombination process

If several defect levels are present in a sample, the effective lifetime τ_{SRH}^{eff} of the sample is the inverse sum of the single defect related lifetimes $\tau_{SRH}(i)$ under the assumption that each defect may be described by an individual SRH-lifetime [161]

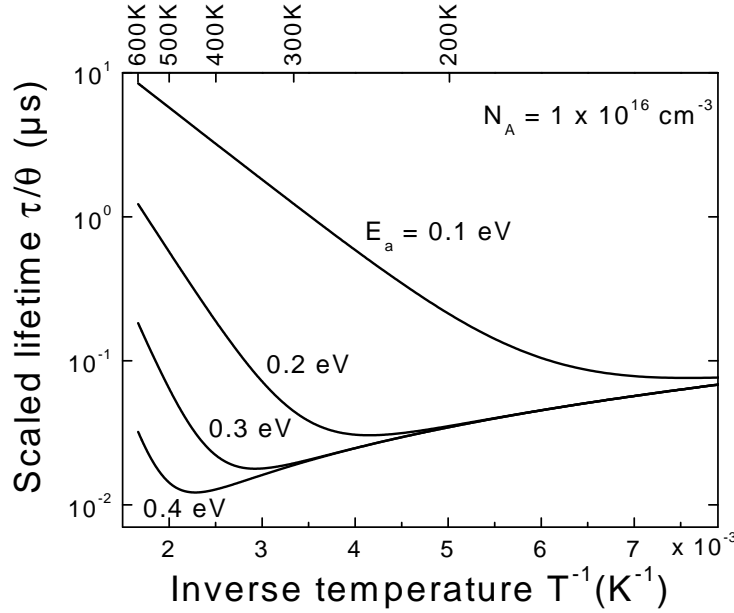$$\frac{1}{\tau_{SRH}^{eff}} = \sum_i \frac{1}{\tau_{SRH}(i)}. \tag{5.7}$$

Figure 5.1: Simulation of the Shockley-Read-Hall lifetime $\tau_{SRH}^{LLI,p}$ divided by the normalized temperature θ of p-type Si with a single defect in the lower half of the band gap, plotted for several activation energies E_a with $p_0 = N_A = 1 \times 10^{16}$ cm^{-3} and $\tau_{n0} = 1$ µs. The higher the activation energy, the higher is the temperature of the minimum in $\tau_{SRH}^{LLI,p}$ and the steeper the slope of the high temperature regime of $\tau_{SRH}^{LLI,p}/\theta$.

Under low level injection and in the case of a p-type semiconductor, using equation 5.6, equation 5.7 can be rewritten by

$$\frac{\theta}{\tau_{SRH}^{eff}} = \sum_i \frac{1}{\tau_{n0}^{300K}(i)} \left[\frac{1}{\theta^{-3/2} + \kappa_i \exp(-E_a^i/k_B T)} \right]. \qquad (5.8)$$

Thus, the defect with the smallest individual lifetime at a given temperature will be the dominating defect at this temperature. As can be seen in figure 5.1, the SRH-lifetime of a single defect level undergoes a minimum at a certain temperature T_{min}, which is determined by the activation energy E_a and the reference lifetime τ_{n0}^{300K}. For very low temperatures $T \ll 300$ K, the defect with the lowest reference lifetime τ_{n0}^{300K} will be the dominant defect. With increasing temperature the recombination activity of defects will decrease according to their activation energies E_a^i. The influence of the E_a on the

recombination activity will be discussed here for the example of a p-type sample with defects in the lower half of the band gap. In this case it holds that $n_1 \ll p_0$ and $n_1 \ll p_1$ and equation 5.4 simplifies to

$$\tau_{SRH}^{LLI,p} = \tau_{n0} \left(1 + \frac{p_1}{p_0} \right), \tag{5.9}$$

where p_1 is exponentially dependent on E_a (see equation 5.2). Figure 5.2 shows the dependence of the ratio p_1/p_0 on the temperature for a typical doping density of thin film solar cells of $p_0 = N_A = 5 \times 10^{16}$ cm^{-3}. Only for values of $p_1/p_0 \ll 1$, the recombination activity of a certain defect level is the highest, i.e. $\tau_{SRH}^{LLI,p}(i) = \tau_{n0}(i)$. Consequently, even a defect level with an activation energy as low as $E_a = 0.2$ eV might be the dominant recombination center at $T = 300$ K, if the respective reference lifetime is lower than that of defect levels with higher activation energies. Figure 5.2 also unveils, that for such high doping levels of $p_0 = 5 \times 10^{16}$ cm^{-3}, the ratio p_1/p_0 of defects with activation energies $E_a \geq 0.3$ eV would be below unity, even at temperatures as high as 450 K. Therefore, if a defect with $E_a \geq 0.3$ eV is the dominant defect, it would not be detectable by a linear increase in the Arrhenius representation of τ/θ for temperatures below 450 K.

In conclusion: if in an Arrhenius representation of τ/θ a linear increase with rising temperature at a given temperature is observed, then the respective defect is the dominant defect level at this temperature. If in the investigated temperature regime no increase with rising temperature is observed, then a defect with an activation energy higher then the maximum observable activation energy may be dominant.

5.2   TQE measurement setup and data analysis

Conventionally, lifetime spectroscopy is carried out using either microwave-detected photoconductance decay (MWPCD) [162] for TDLS or quasi-steady-state photoconductance (QSSPC) [163] for IDLS. These methods require silicon wafers with well passivated surfaces for the analysis of the minority carrier lifetime, and are not applicable to processed devices or thin films. Internal quantum efficiency (IQE) allows for the determination of the minority carrier diffusion length, hence the minority carrier lifetime in processed solar
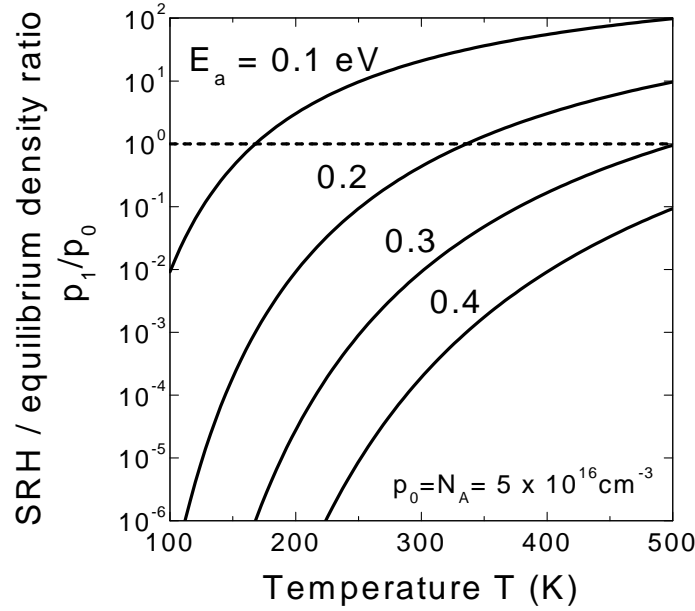
Figure 5.2: Dependence of the ratio of the SRH-density p_1 to the equilibrium density p_0 on the temperature for different trap energies E_t. The equilibrium density p_0 is fixed to a typical value of the doping density $N_A = 5 \times 10^{16}$ cm^{-3} for thin film solar cells. For values of $p_1/p_0 \ll 1$ the corresponding lifetime of the defect is equal to the capture time constant τ_{n0}.

cells, and under certain circumstances also in thin film solar cells. Here, for the first time, temperature dependent quantum efficiency measurements are used as a device specific method of lifetime spectroscopy for thin film solar cells.

Measurement setup

Figure 5.3 shows schematics of the measurement setup for the standard room temperature measurement of the external quantum efficiency EQE (figure 5.3a) and of the setup for temperature dependent EQE measurement (figure 5.3b). In the latter case, the monochromatic light from the monochromator is conducted by an optical fiber to the cryostat that allows for temperature control of the sample in a range of $T_{EQE} = 80 \dots 420$ K. Measurements at room temperature in the standard setup and in the cryostat serve to

generate a calibration file for the corrections of optical losses due to the optical fiber and the viewport of the cryostat.
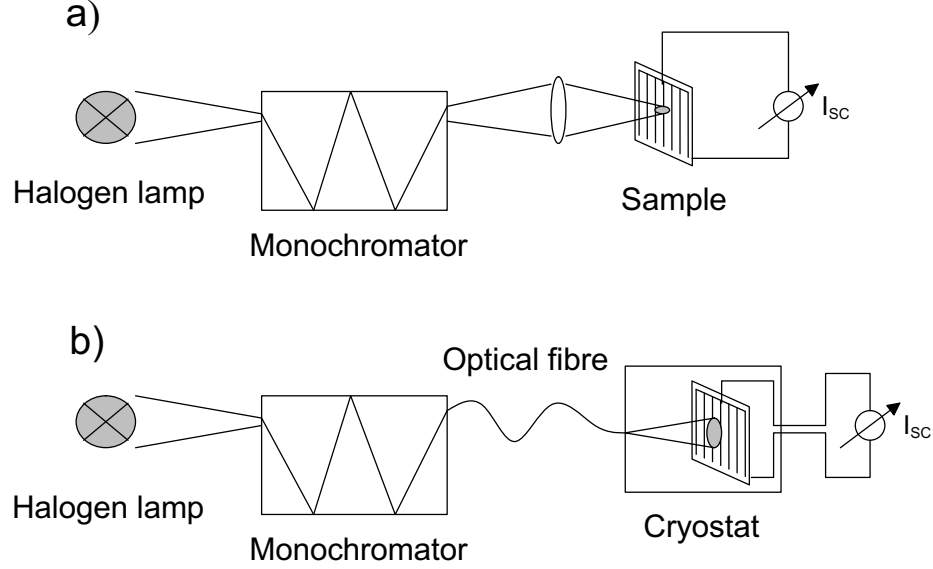

Figure 5.3: Measurement setup for a) the standard room temperature measurement of the external quantum efficiency, and b) for the temperature dependent quantum efficiency. In the latter case, an optical fiber serves to conduct the monochromatic light to the cryostat in which the sample is mounted.

Data analysis

The internal quantum efficiency of the sample is calculated from the EQE and the reflectance, as described in chapter 3.3.1. Figure 5.4 shows an example of the temperature dependent internal quantum efficiency of a thin film Si solar cell. The epitaxial absorber and emitter layer of this solar cell were deposited at $T_{dep} = 460°C$, which results in a high number of point defects (see chapter 4.3). Therefore, the internal quantum efficiency as well as the minority carrier diffusion length of the films are rather low.

There are two factors contributing to a shift of the EQE with the temperature: i) the increase of the carrier lifetime with increased temperature as discussed above, and ii) the increased absorption coefficient α. In order to extract the lifetime from the temperature de-
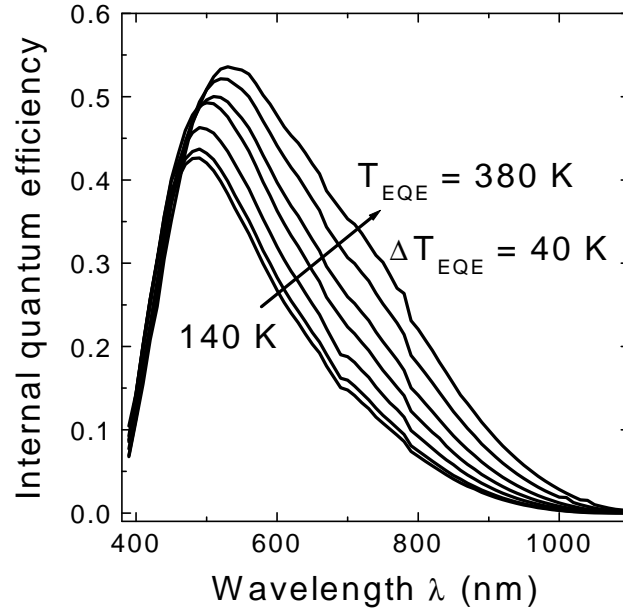
Figure 5.4: Temperature dependent measurements of the internal quantum efficiency IQE of an epitaxial thin film solar cell. The film was deposited at rather low temperature $T_{dep} = 460°C$ and therefore contains a high number of point defects, limiting the maximum IQE value to 0.6. Two major effects cause a shift of the IQE maximum to higher wavelengths with increasing measurement temperature T_{EQE}: i) higher minority carrier lifetime and ii) higher absorption.

pendent quantum efficiency, the analysis software has to take the temperature dependent absorption coefficient into account. This is done following the model of Rajkanan [164] for the temperature dependent absorption coefficient $\alpha(T)$. Under consideration of the possible phonon contributions of energy E_p and the direct as well as different indirect band gaps E_g, $\alpha(T)$ is empirically given by

$$\alpha(T) = \sum_{i,j} C_i A_j \left\{ \frac{[hc/\lambda - E_{gj}(T) + E_{pi}]^2}{[\exp(E_{pi}/k_B T) - 1]} - \frac{[hc/\lambda - E_{gj}(T) - E_{pi}]^2}{[\exp(-E_{pi}/k_B T) - 1]} \right\}$$
$$+ A_d \sqrt{hc/\lambda - E_{gd}(T)} \tag{5.10}$$

where the values of the constants $C_1, C_2, A_1, A_2,$ and A_d are derived from a fit to experimental absorption data and are given in table 5.1. The temperature variation of the bandgaps is given by [165]

$$E_{gi}(T) = E_{gi}(0K) - 7.021 \times 10^{-4}\,\text{eV}\,\frac{T^2}{T + 1108K}. \qquad (5.11)$$

Table 5.1: Constants for the calculation of the temperature dependent absorption coefficient [164].

Quantity	Units	Value
E_{g1} (0)	(eV)	1.17
E_{g2} (0)	(eV)	2.5
E_{gd} (0)	(eV)	3.2
E_{p1}	(meV)	18.27
E_{p2}	(meV)	57.73
C_1		5.5
C_2		4.0
A_1	(cm^{-1} eV^{-1})	323.1
A_2	(cm^{-1} eV^{-1})	7237
A_d	(cm^{-1} eV^{-1})	1.052$\times 10^6$

The temperature dependent model of the absorption coefficient $\alpha_\lambda^{mod}(T)$ is used to generate a temperature and wavelength dependent correction factor $f(\lambda, T) = \alpha_\lambda^{mod}(T)/\alpha_\lambda^{mod}(300)$. The absorption coefficient $\alpha(\lambda, T)$ is then obtained by correcting the experimental room temperature absorption coefficient $\alpha_\lambda^{exp}(300)$ from [166] with the help of $\alpha(\lambda, T) = f(\lambda, T)\alpha_\lambda^{exp}(300)$.

The diffusion length L is derived from IQE measurements by simulation of the IQE using a self-written computer program. This computer program, based on an analytical model for the quantum efficiency [167] (see appendix A), takes the temperature variation

of the absorption, the mobility, the diffusion constants, the band gap, the intrinsic carrier concentration, and the build-in voltage into account. In order to verify the accuracy of the analysis, the results of the room temperature measurements are crosschecked with the computer program IQE1D [140], and found to be in good agreement. The analytical model covers the current generation in the emitter, the space charge region, and the active base of the cell, under consideration of the front and rear surface recombination. In the case of thin film solar cells, deposited on a highly doped substrate, the contribution of the substrate to the total current can be neglected as long as the diffusion length does not exceed the active film thickness. In this case the rear surface recombination of the model corresponds to the recombination at the interface from the epitaxial film to the substrate.

The lifetime τ of electrons in p-type material is calculated from the diffusion length L by

$$\tau_n = \frac{L_n^2}{D_n}. \tag{5.12}$$

The diffusion coefficient D_n for electrons is given by the Einstein relationship

$$D_n(T) = \frac{k_B T}{q} \mu_n(T). \tag{5.13}$$

Herein, the temperature dependence of the electron mobility is given by

$$\mu_n(T) = \mu_n^{300K} \left(\frac{T}{300K} \right)^{-2.3}, \tag{5.14}$$

with μ_n^{300K} being the mobility at room temperature [168,169].

A fit of equation 5.6 to experimental temperature dependent lifetime data allows for the determination of the activation energy E_a, the reference lifetime τ_{n0}^{300K}, and in the case of a defect level in the upper half of the band gap (case B) the ratio $\tau_{p0}^{300K}/\tau_{n0}^{300K}$.

5.3   TQE of epitaxial thin film solar cells

Two-defect model

The temperature dependent lifetime scaled by the normalized temperature θ of a thin film solar cell deposited at $T_{dep} = 510°C$, as deduced from TQE measurements is presented in figure 5.5. The data, when compared to the simulated data shown in figure
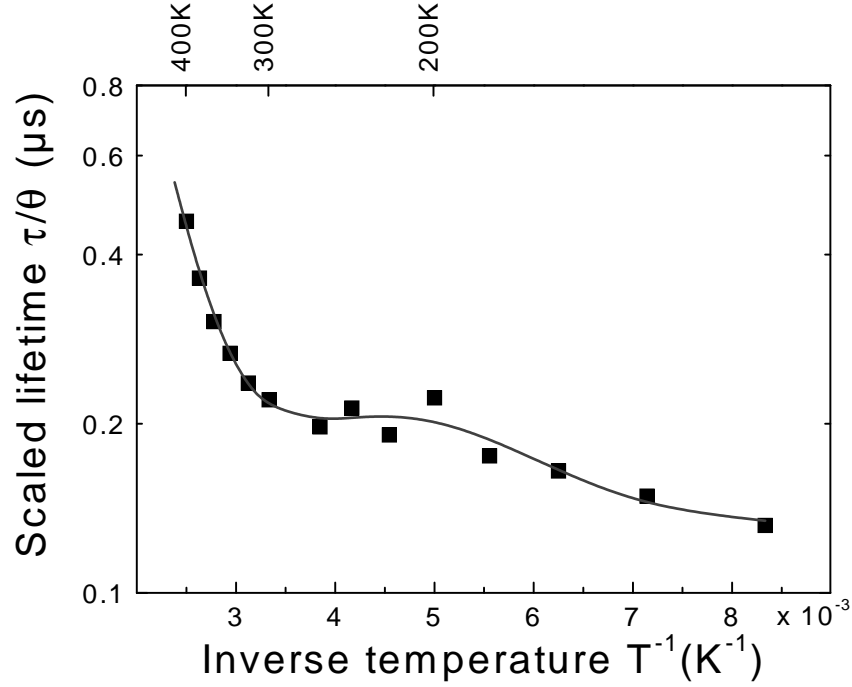
Figure 5.5: *Scaled temperature dependent lifetime τ/θ of a thin film solar cell deposited at $T_{dep} = 510°C$ as deduced from temperature dependent quantum efficiency measurements. The solid line is a fit to the data with a two defect model unveiling activation energies of $E_a^1 = 0.19$ eV and $E_a^2 = 0.07$ eV above the valence band and respective reference lifetimes constants of $\tau_{n01}^{300K} = 0.18$ and $\tau_{n02}^{300K} = 0.03$ μs.*

5.1, demonstrate that not only one single energetic defect level contributes to the total diffusion length. Therefore, a simple two defect model will be developed to simulate the data. This model consists of a superposition of two SRH-traps, following equation 5.8. The DLTS results of p-type films presented in chapter 4.3.1 show several defect levels in the lower half of the band gap. Therefore, for the analysis of thin films solar cells with a p-type base, two defect levels in the lower half of the band gap with activation energies E_a^1 and E_a^2 and respective reference lifetimes $\tau_{n0}^{300K}(1)$ and $\tau_{n0}^{300K}(2)$ are assumed. Using $\kappa = N_V^{300K}/N_A$ (case A), equation 5.8 with two defects reads

$$\frac{\theta}{\tau_{SRH}^{eff}} = \sum_{i=1}^{2} \frac{1}{\tau_{n0}^{300K}(i)} \left[\frac{1}{\theta^{-3/2} + (N_V^{300K}/N_A)\exp(-E_a^i/k_B T)} \right]. \qquad (5.15)$$

Herein, $\tau_{n0}^{300K}(1,2)$, $E_a^{1,2}$, and N_A are the only free parameters. The equilibrium doping density of the films was determined by CV-measurements and found to be $N_A = 5 \times 10^{16}$ cm^{-3} for all investigated samples. A least squares fit of equation 5.15 to the data serves to determine the defect characteristic values of $\tau_{n0}^{300K}(1,2)$ and $E_a^{1,2}$. The fit of the two defect model to the data is represented by the solid line in figure 5.5 with two rather shallow defects with activation energies of $E_a^1 = 0.19$ eV and $E_a^2 = 0.07$ eV above the valence band and respective capture reference lifetimes of $\tau_{n0}^{300K}(1) = 0.18$ and $\tau_{n0}^{300K}(2)$ $= 0.03$ μs. Figure 5.6 compares the scaled lifetime τ/θ of this sample and three other samples which were deposited using various deposition parameters. All four samples show a steep increase of τ/θ with increasing temperature with onset at around 300K. Fitting of the data with the proposed two-defect model, depicted in solid lines, gives very similar results of the activation energies E_a, as listed in table 5.2. This suggests, that the dominating defect remains the same, though deposition rate and temperature are varied. This also demonstrates the advantage of the temperature dependent quantum efficiency, as defects in films deposited at temperatures above 460°C where not resolved by DLTS and photoluminescence measurements.

Additionally, the data was fitted with N_A as a free parameter in order to check the self-consistency of the fits. In this case, the fits reproduced the free carrier densities within a limit of 50% and the trap activation energies were found still consistent.

The dominant defect levels of the samples deposited at $T_{dep} = 460$°C at room temperature are in very good agreement with the results from DLTS measurements of the same films, as shown in figure 5.7. The DLTS-defect level of 0.172 eV of the film deposited at $r_{dep}= 0.3$ μm/min is in good agreement with the TQE-defect level of 0.16 eV. For the film deposited at $r_{dep} = 0.5$ μm/min, two DLTS-defect levels of 0.206 and 0.217 eV might be responsible for the dominant defect level identified by TQE of 0.21 eV. Although the spectra of the film deposited at $r_{dep}= 0.3$ μm/min, as well as of other p-type films also show deeper defect levels, as depicted in figure 4.14, the TQE-measurements demonstrate that the defect levels around 0.2 eV have the major influence on the device performance at room temperature.
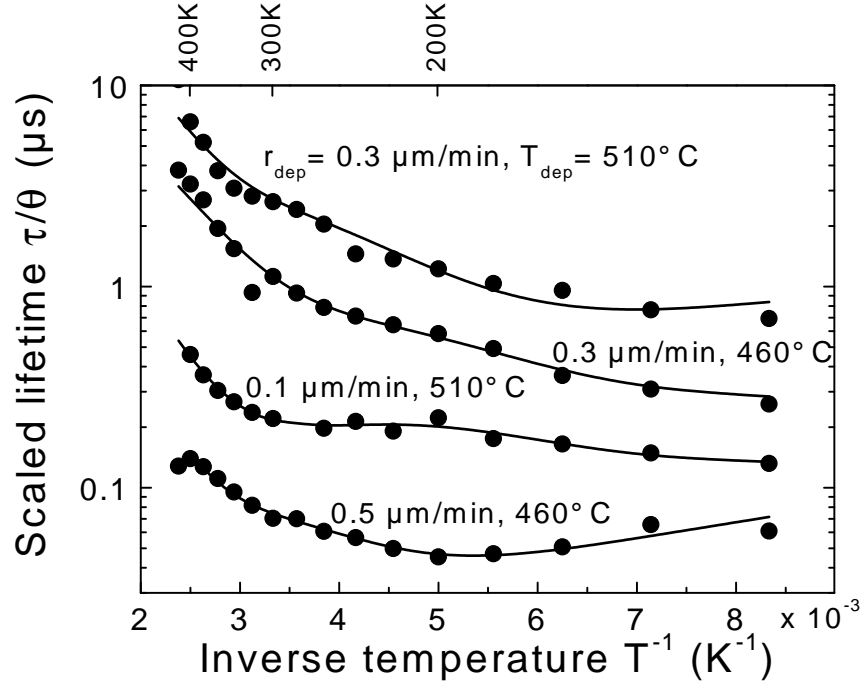
Figure 5.6: Comparison of the temperature dependent lifetime of four epitaxial thin films deposited at various deposition temperatures T_{dep} and rates r_{dep}. The solid lines are fits to the measurement data using the two-defect model. Details of the fits results are given in table 5.2.

Estimation of the defect density

As no direct determination of the defect density for films deposited at temperatures above $T_{dep} = 460°$C is possible by using DLTS, the minority carrier diffusion length, a sensible measure of the electronic quality of the films, can serve to analyse the defect density in the epitaxial films. This is possible if the defect density and the minority carrier lifetime are both known for a single deposition temperature and under the assumption that the dominant recombination mechanism remains the same independent of T_{dep}. The DLTS-results for the film deposited at $T_{dep} = 460°$C and $r_{dep} = 0.3$ μm/min are given in table 5.3. The defect level with $E_t = 0.17$ eV is identified as the dominant defect level at 300 K by the TQE measurements, as stated above. Together with the data from the lifetime-spectroscopy provided in table 5.2, the capture cross section for electrons σ_n is determined

Table 5.2: Fit parameters $\tau_{n0}^{300}(1,2)$ and $E_a^{1,2}$ for the fit of the temperature dependent lifetime displayed in figure 5.6. The trap energies E_a^1 and E_a^2 are similar although the films were deposited at various deposition temperatures and rates. The reference lifetimes $\tau_{n0}^{300}(1,2)$ of the films support the results of chapter 4.4.1, i.e. the lifetime of the films increases with increasing deposition temperature and the highest lifetimes are found at a deposition rate around 0.3 μm/min.

| film deposited at | | E_a^1 | E_a^2 | $\tau_{n0}^{300}(1)$ | $\tau_{n0}^{300}(2)$ |
rate (μm/min)	temperature (°C)	(eV)	(eV)	(μs)	(μs)
0.3	510	0.16	0.07	1.60	0.18
0.3	460	0.16	0.07	0.71	0.06
0.1	510	0.19	0.07	0.18	0.03
0.5	460	0.21	0.11	0.10	0.02

for a doping level of 5×10^{16} cm^{-3} and a minority carrier diffusion length of $L = 5$ μm at $T_{EQE} = 300$ K via

$$\sigma_n = \frac{D_n}{v_{th} N_t L^2} \left[1 + \frac{N_V}{N_A} \exp\left(-\frac{E_t - E_V}{k_B T} \right) \right] \tag{5.16}$$

to be $\sigma_n = 7.9 \times 10^{-13}$ cm^{-2}. For a series of depositions where only the deposition temperature is varied, it may be assumed that the dominant defect responsible for device degradation remains the same. This is supported by the results of the film deposited at $T_{dep} = 510$°C and $r_{dep} = 0.3$ μm/min, as given in table 5.2, which show the same defect levels as the film deposited at $T_{dep} = 460$°C. Under these assumptions and for a given deposition temperature, the measurement of the room temperature minority diffusion length L allows for the determination of the defect density N_t

$$N_t = \frac{D_n}{v_{th} \sigma_n L^2} \left[1 + \frac{N_V}{N_A} \exp\left(-\frac{E_t - E_V}{k_B T} \right) \right] = \frac{A_{def}}{L^2} \tag{5.17}$$

with A_{def} being a characteristic defect constant, fully determined by the doping concentration N_A and the defect parameters σ_n and E_t. For the film deposited at $T_{dep} = 460$°C
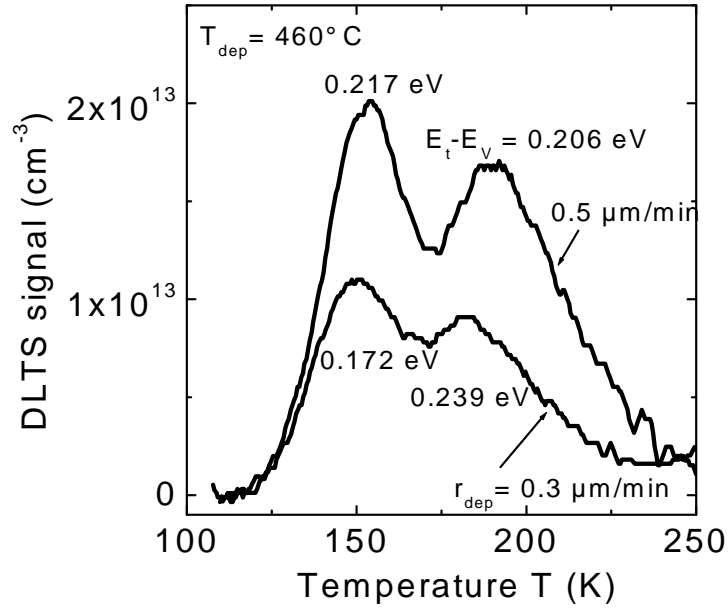
Figure 5.7: Deep level transient spectroscopy reveals several defect levels in p-type films deposited at $T_{dep} = 460°C$. The defect levels around of 0.172 eV of the film deposited at $r_{dep} = 0.3 \, \mu$m/min and the two defect levels around 0.21 eV found for the film deposited at $r_{dep} = 0.5 \, \mu$m/min correspond nicely to the dominant defect centers as determined by TQE-analysis

and $r_{dep} = 0.3 \, \mu$m/min A_{def} is given by $2.16 \times 10^{-6} \, \text{cm}^{-1}$, and for the film deposited at $T_{dep} = 460°C$ and $r_{dep} = 0.5 \, \mu$m/min $A_{def} = 1.47 \times 10^{-6} \, \text{cm}^{-1}$. For these two sample series with deposition rates $r_{dep} = 0.3$ and $0.5 \, \mu$m/min, figure 5.8a depicts the temperature dependence of the room-temperature minority carrier diffusion length on the deposition temperature of the epitaxial film, and figure 5.8b the corresponding calculated defect density. Both sample series show an exponential decay of the defect density with increasing deposition temperature.

5.4 Discussion: TQE method

Temperature dependent quantum efficiency (TQE) is introduced here as a new lifetime spectroscopy method that applies to processed solar cells. This method allows for the

Table 5.3: Energetic position $E_t - E_V$, trap density N_t, and capture cross section σ_p of defects as determined by DLTS in a film deposited at $T_{dep} = 460°C$ and $r_{dep} = 0.3 \, \mu m/min$ by IAD.

peak	$E_t - E_V$ (meV)	N_t (cm^{-3})	σ_p (cm^{-2})
1	172	1.1×10^{13}	1.6×10^{-17}
2	239	1.1×10^{13}	7.4×10^{-17}
3	458	1.1×10^{13}	9.0×10^{-16}

determination of the dominant recombination processes in the absorber material. The analysis of the data requires a thoroughly temperature dependent modeling of the absorption and recombination processes, that is carried out using a newly developed computer program. The advantage of lifetime spectroscopy is the high sensitivity of the method. In contrast to DLTS, the sensitivity is not only determined by the defect density N_t, but the product of defect density and capture cross section $N_t\sigma$. Therefore, defects with high recombination activity, i.e. high values of σ may be detected, though their density may be low. However, if in a combined analysis the same defect levels are identified with DLTS and TQE, all the recombination parameters, activation energy E_A, defect density N_t, and capture cross sections for electrons and holes σ_n, σ_p may be determined. If all the recombination parameters of a film deposited at certain deposition parameters are known, the defect density of films deposited under similar deposition conditions can be estimated from a simple room temperature IQE-measurement under the assumption that the dominant defect remains the same.

The TQE method is here applied to thin epitaxial films, that showed a variety of defect levels as determined by DLTS and PL. In all investigated films a clear activation of the lifetime with the temperature is observed. However, it is not possible to model the data using SRH-statistics with a single energetic level. A two defect model allowed the satisfactory analysis of the data revealing rather shallow defect levels in the range of E_A
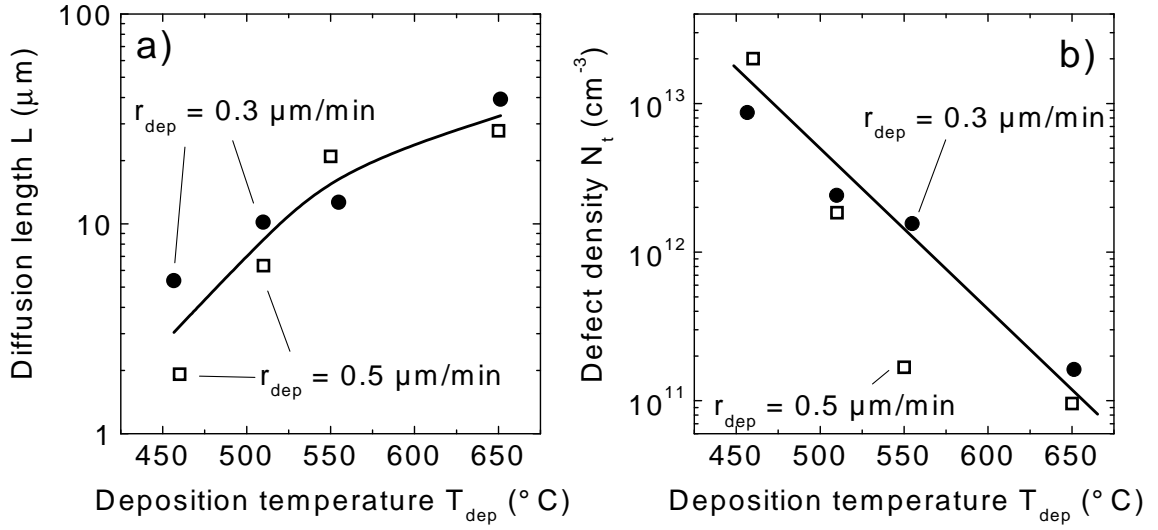
Figure 5.8: a) Dependence of the minority carrier diffusion length on the deposition temperature for samples deposited at deposition rates of 0.3 and 0.5 um/min, respectively. b) The defect density of the samples is calculated by the parameters of the dominant defect determined from the film deposited at $T_{dep} = 460°C$ and the deposition temperature dependent minority carrier diffusion length given in a).

$= 0.16 \ldots 0.21$ eV being the dominant recombination center at room temperature. This finding supports the correlation of the defect density of the 0.2 eV band with the minority carrier diffusion length as given in figure 4.18. The second defect center, found at $E_A = 0.07$ eV in three of the four investigated thin films, is the dominant defect in the low temperature regime $T < 250$ K. This center may be identified with Gallium that shows a shallow acceptor level at 0.07 eV [160]. Gallium may be introduced into the thin films from the decomposition of GaP used in the deposition system for phosphorous doping purpose.

The high sensitivity of the TQE-method is demonstrated by the clear signature of the two defects found in the film deposited at $T_{dep} = 510°C$ and $r_{dep} = 0.3$ μm/min, see figure 5.6. For the same film, neither PL nor DLTS investigations allowed a clear defect determination. However, the TQE-method is limited by the extraction of the diffusion length L from the IQE as for some devices within the necessary temperature range L

either exceeds the thickness of the photovoltaic active base W_b or falls below the width of the space charge region W_j. In both cases the extraction of the bulk diffusion length L from TQE spectra becomes difficult or even ambiguous. However, within the restriction $W_j < L < W_b$, TQE analysis of completed solar cells proves itself as a reliable device-based method for detecting and analyzing recombination centers that limit the diffusion length and, in consequence, the photovoltaic performance of the devices.

Chapter 6

Epitaxial growth on arbitrary substrate orientations

This chapter investigates the formation of defects during low temperature epitaxial growth on non-(100)-oriented substrates and their influence on the electronic properties. First the properties of epitaxial films grown on monocrystalline (111)-, (110)-, and (113)-oriented substrates are discussed, followed by investigations of growth on arbitrarily oriented substrate surfaces. Finally, a classification for the suitability of substrate orientations for low temperature epitaxial growth is given.

6.1 Deposition on monocrystalline Si(111), Si(110) and Si(113)

6.1.1 Extended defects

In contrast to epitaxial growth on (100)-oriented substrates, growth on non-(100)-oriented substrates is dominated by the formation of stacking faults and dislocations. Table 6.1 compares the densities of extended defects in (100)- and (111)-oriented films. The (111)-oriented films show significantly higher densities of extended defects as revealed by Secco etching. This is in accordance with investigations of Oberbeck [7], who found a minimum

Table 6.1: Comparison of the extended defect densities of films deposited on (100)- and (111)-oriented substrates. (100)-films were grown at $T_{dep} = 460\ldots700°C$ and $r_{dep} = 0.1\ldots0.5$ $\mu m/min$, (111)-films at $T_{dep} = 460°C$ and $r_{dep} = 0.3$ $\mu m/min$ on wafers as delivered by the manufacturer without any ex-situ pretreatment.

Substrate	defect density (cm^{-2})	
orientation	dislocations	stacking faults
(100)	$< 1 \times 10^3$	$< 1 \times 10^2$
(111)	3×10^5	7×10^4

of the density of extended defects at around 10^5 cm^{-2} in (111)-oriented films deposited by IAD at $T_{dep} = 650°C$ and $r_{dep} = 0.3$ $\mu m/min$, while (100)-oriented films, deposited in the same run, and which underwent the same ex-situ pretreatment did show significantly lower defect concentrations. Therefore, an influence of the deposition conditions may be excluded and the higher defect density of (111)-films is a result of the different substrate orientation. High-resolution TEM investigations of films deposited below 460°C on Si(100), Si(110), and Si(113) showed that stacking faults nucleate on {111}-planes once the surface gets rough due to the low Si adatom mobility at low deposition temperatures [38]. These investigations also demonstrated that films deposited at low temperatures on Si(111) have an anisotropy of the stacking fault formation. At T_{dep}=355°C, the stacking faults in the defective layer are nearly exclusively nucleating on the {111}-planes parallel to the substrate surface, whereas at $T_{dep} = 450°C$ stacking faults are nearly exclusively nucleating on inclined {111}-planes. In the intermediate range of the deposition temperature, nucleation on both types of {111}-planes is observed. Such an observation may be explained by the 7 x 7 surface reconstruction of the Si(111) surface, which is highly stable under deposition at low temperatures [28]. The 7 x 7 reconstruction already contains a stacking fault that is parallel to the substrate surface [130,131]. If the surface reconstruction is not reordered completely during growth at low temperatures, this stacking fault may still be present in the epitaxial film.

6.1.2 Point defects

Deep level transient spectroscopy measurements of (111)-oriented films deposited at T_{dep} = 650°C give rise to DLTS-signals equivalent to point defect densities of 7×10^{13} cm^{-3}. However, due to broad, overlapping peaks the corresponding energy levels are not resolved. As a result of shunting problems possibly caused by the high density of stacking faults and dislocations, DLTS could not be applied to (111)-oriented samples deposited at lower temperatures $T_{dep} \leq 550$°C.

Photoluminescence investigations of films deposited on (111)-oriented substrates at T_{dep} = 650°C and r_{dep} = 0.5 μm/min, as shown in figure 6.1, reveal a band to band luminescence structure, consistent of the broad B, C, and D-peaks, similar to (100)-oriented films (see chapter 4.2.1). However, with decreasing deposition temperature this band to band luminescence decreases rapidly. At T_{dep} = 460°C only a weak D-peak and weak defect luminescence for photon energies below $h\nu$ = 0.85 eV is observed. Films deposited at lower deposition rates r_{dep} = 0.1 and 0.3 μm/min show equal results. (100)-oriented films deposited in the same run as the above described (111)-oriented samples show P-line luminescence, as the deposition was carried out using accelerated silicon ions with V_{acc} = 20 V. Such lines are not observed for the (111)-oriented films.

Figure 6.2 compares photoluminescence spectra of films deposited at T_{dep} = 650°C on (100)-, (111)-, (110)-, and (113)-oriented substrates by IAD. All spectra have a similar ratio of the band to band luminescence peaks A to E, however, at a significantly different total intensity. It is noted that all films were deposited in the same run and the PL measurements were carried out in the same PL-session without any change of the PL setup. Consequently, the only difference of the films is the surface orientation of the substrate, resulting in the observed differences in the PL properties. Of the samples investigated here, only the (113)-oriented film, which has the highest intensity, shows a small peak at 0.96 eV and broad defect luminescence for photon energies below 0.85 eV. The peak around 0.96 eV might be identified as the G-line found at 0.97 eV after irradiation of carbon rich samples [68,70].

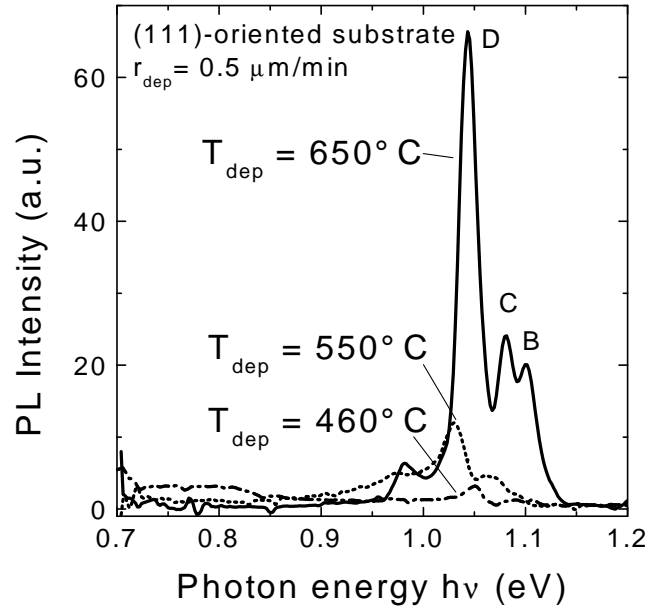It is noted, that no D-line luminescence, associated with decorated dislocations (see

Figure 6.1: Thin films deposited by IAD at $T_{dep} = 650°C$ on (111)-oriented substrates show the typical band to band luminescence with the B, C, and D-peaks also observed for (100)-oriented films. The intensity of this band to band luminescence decreases rapidly with decreasing deposition temperature. At $T_{dep} = 460°C$ weak defect luminescence for photon energies below 0.85 eV is observed.

chapter 2.2.2) is found in (111)-oriented films, although the dislocation density is at least of the order of 3×10^5 cm^{-2} for these films.

In conclusion, the DLTS and photoluminescence investigations unveil only few details about defects in non-(100)-oriented films. The DLTS results reveal, that the point defect density of (111)-films deposited at $T_{dep} = 650°C$ is orders of magnitude higher than for (100)-oriented films deposited in the same deposition run (see chapter 5.3). For such films, the photoluminescence results showed, that the band to band recombination of (113)-, (110)-, and (111)-oriented films is similar to that of (100)-oriented films. Defect structures other than the broad defect distribution below 0.85 eV, that might be comparable to the broad peak around 0.8 eV in (100)-oriented films and the G-line in the spectrum of the (113)-oriented film deposited at 650°C, are not found. Astonishingly, the fact that DLTS and PL do not seem to be suitable for the detection of point defects in non-

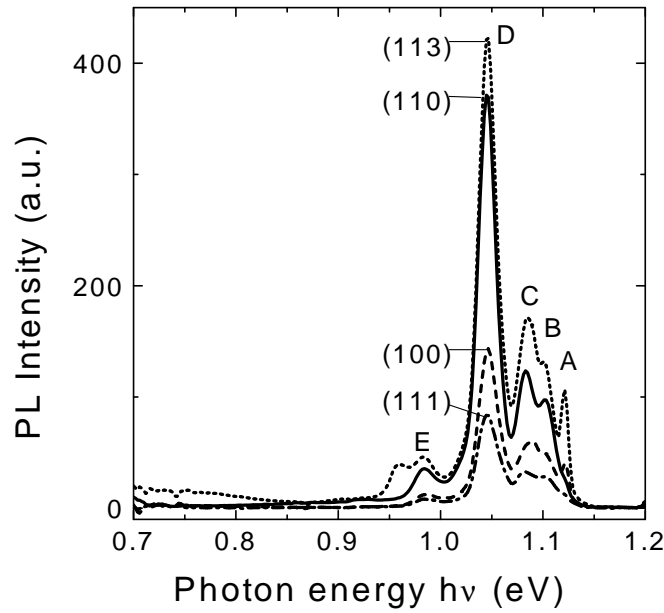*Figure 6.2: Photoluminescence of four films deposited simultaneously by IAD with $T_{dep} = 650°C$ and $r_{dep} = 0.3$ μm/min on (113)-, (110)-, (100)-, and (111)-oriented substrates. All films show similar features with comparable intensity ratios of the A to E peaks. Only the (113)-oriented film shows an additional defect peak at $h\nu = 0.96$ eV and low luminescence intensity for $h\nu < 0.85$ eV.*

(100)-oriented films is most probably a result of the high density of structural and point defects themselves. While the DLTS measurements for films deposited at temperatures below 650°C are hampered by the poor rectifying properties of the diode structures, the photoluminescence intensity of the (111)-oriented films most probably is low because of a high density of non radiative recombination centers.

6.1.3 Electronic properties of (111)-, (110)-, and (113)-oriented films

Figure 6.3 depicts the dependence of the minority carrier diffusion length L on the applied acceleration voltage V_{acc}, i.e ion energy, during ion assisted growth for films deposited at $T_{dep} = 650°C$. At $V_{acc} = 0$ V, this is the case of "normal" MBE, the substrate is

grounded. For (100)-oriented films, L increases with rising ion energy, whereas L of (111)-, (110)-, and (113)-oriented films decreases. Note, that although the minority carrier diffusion length of the non-(100)-oriented films is equal to or even higher than L of the (100)-film at $V_{acc} = 0$ V, the other solar cell parameters, especially the fill factor, and in the case of the (110)-film the open circuit voltage, are significantly lower, most probably as a result of shunts caused by the high density of structural defects in the films. The origin of the detrimental influence of accelerated ions during growth on the electronic properties of non-(100)-oriented films remains unclear up to now, and is unprecedented in the literature.
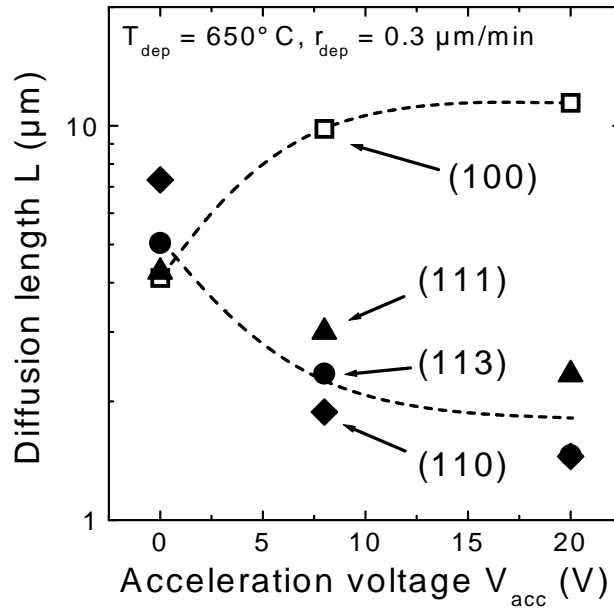

Figure 6.3: The minority carrier diffusion length L increases with applied acceleration voltage V_{acc} in the case of (100)-oriented films. In contrast, films deposited on other substrate orientations, such as Si(111), Si(110), and Si(113) display a decreasing L with increasing V_{acc}. After [7];

Table 6.2 gives an overview of solar cells processed at higher deposition temperatures of $T_{dep} = 750$°C with $r_{dep} = 0.36$ μm/min. The cells have a simple planar cell structure as depicted in figure 6.4, with no light trapping. The active cell consists of an epitaxial film with total thickness of 15 μm including the p-type base with p$^+$-type back surface field

and an n$^+$-type doped emitter. A 75 nm thick SiN-layer serves as antireflection coating and surface passivation layer. The SiN is opened photolithographically for front contact metalization and the backside of the highly boron doped substrate is contacted by an Al layer.

Table 6.2: Solar cell results (not approved) of cells processed at $T_{dep}=$ 750°C on (100)- and (111)-oriented substrates by MBE (V_{acc}=0 V) and IAD (V_{acc}=20 V). The thickness of the active epitaxial film is 15 μm. The cells have a SiN antireflection and surface passivation coating, but no light trapping is applied.

Substrate orientation	V_{acc} (V)	I_{SC} (mA)	V_{OC} (mV)	FF (%)	η (%)
(100)	0	27.5	616	81.2	13.8
(100)	20	27.7	622	79.9	13.8
(111)	0	22.5	452	52.6	5.4
(111)	20	16.7	404	50.1	3.4

Both (100)-oriented films show a relatively high conversion efficiency of η=13.8 % independent of the use of accelerated silicon ions. Simulations with the computer program PC1D [170] and the evaluation of internal quantum efficiency confirm, that the minority carrier diffusion length of the solar cells is at least greater than 30 μm. At this high deposition temperature the influence of the additional kinetic energy of the ions on the properties of the epitaxial layer is negligible as the Si adatoms already have a high mobility due to the high substrate temperature. However, this does not hold for the case of (111)-oriented epitaxial films. Though the performance of the (111)-oriented cells is already inferior compared to (100)-cells in the order of $\eta = 5\%$, all of the solar cell parameters deteriorate if accelerated silicon ions are used.
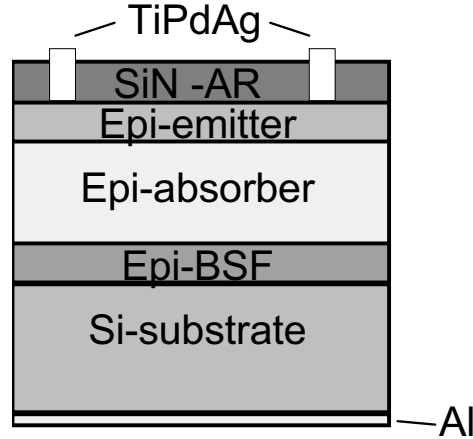
Figure 6.4: Structure of the test solar cells used to compare the influence of accelerated silicon ions and substrate orientation on the electronic properties of epitaxial silicon films deposited at $750°C$ (see table 6.2). The total thickness of the epitaxial film is about 15 μm. The sketch is not to scale.

6.2 Deposition on polycrystalline substrates

6.2.1 Electronic properties of polycrystalline epitaxial films

The results described above, concerning the minority carrier diffusion length and solar cell results of (100)- and (111)-oriented epitaxial films suggest that the substrate orientation has a significant influence on film growth at low temperatures. In order to investigate epitaxial growth on arbitrarily oriented substrates we deposit thin epitaxial films on commercially available polycrystalline silicon substrates (BAYSIX) at $T_{dep} = 650°C$. Figure 6.5 shows light beam induced current (LBIC) measurements of a test solar cell.

The short circuit current generated in different grains by local illumination of the sample using a laser beam varies up to a factor of three. The recombination activity within the grains causes the variation in the short circuit current, as grain boundaries do not show pronounced recombination. Also, the differences in current collection do not stem from a breakdown of epitaxy during growth but from differences in the density of extended and/or point defects in the grains as verified by cross sectional transmission
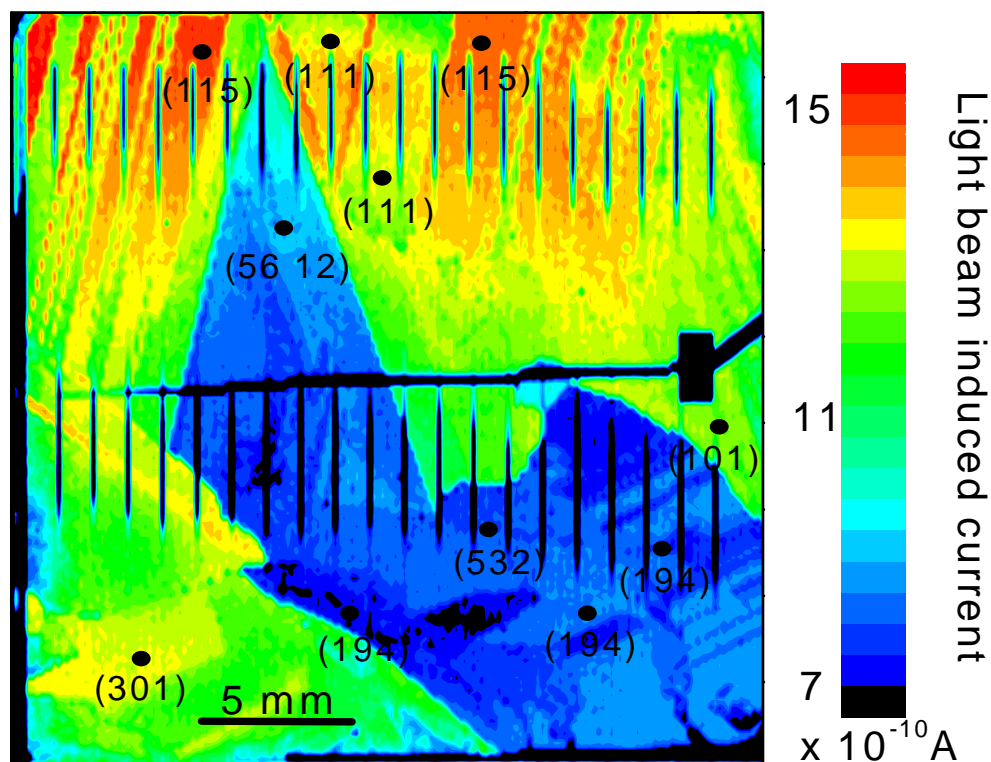
Figure 6.5: Light beam induced current (LBIC) from a solar cell using an epitaxial layer deposited at 650°C. Some of the grain orientations have been determined by electron back-scattering diffraction (EBSD).

electron micrographs (TEM), see figure 6.7. To further investigate the correlation between current collection and grain orientation, the orientation of several grains is determined by means of electron back-scattering diffraction (EBSD) [171] and related to the generated current as detected by LBIC[1]. Table 6.3 summarizes a representative selection of these data, the respective spots on the sample where the measurements were carried out are indicated in figure 6.5.

To interpret the above results, it is important to know that epitaxial growth of silicon at low temperatures is governed by the state of the substrate surface. Commonly, a surface is called stable (or singular) when it forms large, atomically flat terraces of the basal plane

---

[1]I gratefully acknowledge M. Nerding from the University of Erlangen-Nürnberg for carrying out EBSD and TEM-investigations

Table 6.3: *Correlation between grain orientation determined using EBSD and short circuit current as measured by means of LBIC for several grains of an epitaxial film grown on a BAYSIX substrate at $T_{dep} = 650°C$.*

Grain orientation	LBIC current ($\times\ 10 \times 10^{-10}$ A)
(115)	15.1
(110)	12.0
(111)	14.0
(532)	8.6
(321)	7.0
(194)	7.2

after polishing and standard cleaning [114], and is represented by a cusp in the Wulff surface energy plot [112]. Although a complete overview of the stable Si surfaces lacks up to now we may assume that most of the orientations with high Miller indices do not posses a stable, terrace-like surface, but consist of facets of adjacent stable surface orientations, as it is demonstrated for the surfaces ranging from (100) to (111) in Ref. [114]. It is remarkable that those areas of the polycrystalline sample in figure 6.5 which generate high short circuit currents show mostly grain orientations which are known to exhibit flat surfaces (e.g. the (111)-surface). In contrast, areas which generate a low short circuit current density exhibit orientations with high Miller indices.

6.2.2   Classification of silicon surfaces

From the electronic properties of films on mono- and polycrystalline substrates presented above, we may distinguish three different types of substrate orientations (see figure 6.6): i) stable (100)-oriented and vicinal terraced surfaces – type A, ii) stable non-(100)-surfaces (e.g. (111) or (113)) and vicinal terraced surfaces – type B, and iii) faceted surfaces

surface type   electronic quality

A→ (100) + vicinals   high

B→ stable non-(100)   medium
      + vicinals

C→ faceted   low

Figure 6.6: Classification of the suitability of Si surfaces for low temperature epitaxy, according to the resulting electronic quality. Type A - Si(100) surfaces and vicinals - result in highest electronic quality, type B - stable, flat surfaces, such as Si(111) and Si(113), and vicinals - result in reduced (medium) electronic quality by the presence of structural defects, and type C - faceted surfaces with high Miller-indices - result in poor minority carrier properties due to high defect densities.

consisting of adjacent stable surfaces – type C.

As already mentioned above in the section about monocrystalline films, the deposition on type A substrates results in excellent crystallographic and electronic properties compared to films on type B substrates, which show a higher density (1×10^5 cm^{-2}) of structural defects. The highest short circuit current observed in figure 6.5 stems from (115)-oriented grains. Despite their small, only two dimers wide (100)-terraces [114,172], (115)-oriented surfaces therefore belong to type A. Epitaxial growth at low temperatures on type C surfaces seems to produce films of poor electronic quality. This result is most probably due to the generation of a high density of structural defects such as stacking faults, twins, or dislocations at the facetted surface. This is demonstrated by transmission electron micrographs (PHILIPS CM30, operated at 300 kV) as depicted in figure 6.7. Some of the grains show almost no defects in the epitaxial layer, whereas high densities ($\approx 1 \times 10^8$ cm^{-2} partial dislocations associated with stacking faults) of stacking faults

nucleating at the substrate surface are observed for others (the grain orientations are not determined in this case).

Figure 6.7: Transmission electron micrograph (cross section, bright field image) of an epitaxial thin film on polycrystalline substrate. In the two dark appearing grains nucleation of a high density of structural defects on the substrate surface is observed, while the epitaxial growth in the bright grain in the middle starts defect free at the substrate surface.

6.3 Discussion: Low temperature epitaxy for photovoltaic applications

The orientation dependence of the electronic and structural properties of low temperature epitaxial thin films has important consequences on the possible applications. It has been shown, that epitaxial films deposited by MBE $V_{acc} = 0$ V and especially at lower temperatures $T_{dep} \leq 650°$C by IAD on (100)-oriented substrates can result in films of high electronic quality. This is demonstrated by diffusion lengths of more than 30 μm for $T_{dep} \geq 650°$C and solar cell efficiencies of 12.7% [173] and 13.8% for simple thin films solar cells (20 μm and 15 μm film thickness) deposited at $T_{dep} = 650$ and 750°C, respectively. However, the electronic properties of films deposited on non-(100)-oriented substrates suffer drastically from high structural and point defect densities in the films, even at deposition

temperatures as high as 750°C. Additionally, irradiation with accelerated Si-ions during growth has a detrimental influence on the electronic quality.

Oberbeck pointed out, using a simple model of two diodes representing (100)-epitaxial grains and non-(100)-oriented grains, that the solar cell performance of polycrystalline epitaxial cells decreases rapidly with increasing fraction of non-(100)-grains [7].

For the application of low temperature epitaxy to the production of solar cells on polycrystalline seed-layers on glass, there are several severe technological challenges. Most large grained laser-crystallized seed layers show a (111)-preferred orientation of the surfaces normals of the grains [174,175]. However, first results with a relatively high fraction of (100)-oriented grains are published [176]. Assumed, that all grains are (100)-oriented, there is still the question of the surface cleaning and silicon oxide removal prior to deposition at glass compatible temperatures. There are several proposals, among them the in-situ sputtering techniques are the most promising [177]. Finally, the epitaxial film still is poly- or microcrystalline, as the grain size is determined by the seeding layer. Here, hydrogen passivation of grain boundaries might result in enhanced device quality. Taking all these technological difficulties into account, the prospect of epitaxial solar cells on seed-layers on glass remains questionable.

Chapter 7

Outlook

The investigations shown in this work revealed a high density of structural defects in low temperature epitaxial silicon films deposited at temperatures $460°C \leq T_{dep} \leq 650°C$. Dependent on the substrate orientation, the electronic properties are determined by point defects or extended defects for (100)-oriented films and non-(100)-oriented films, respectively. The use of moderately accelerated Si-ions ($V_{acc} \approx 20$ eV) during deposition is favorable for (100)-oriented films: the minority carrier diffusion length L increases with applied acceleration voltage V_{acc}. However, for $V_{acc} \gg 50$ V, the increased defect generation results in decreasing electronic quality of the films. An increase of the fraction of Si-ions in the beam, by a modification of the ionization stage in the deposition chamber, while still using low acceleration voltages $V_{acc} \approx 20$ eV might result in further improved electronic quality of the (100)-oriented films.

The origin of the increased L for (100)-oriented films and decreased L for non-(100)-oriented films upon deposition with Si-ions is only poorly understood so far. Here, the application of the temperature dependent quantum efficiency (TQE), developed in this work, might unveil the dominant recombination mechanism in the non-(100)-oriented films. Furthermore, such investigations might help to clarify the defect reactions initiated by the ion-bombardment for both, (100)- and non-(100)-oriented films.

The hypothesis that the broad peak around 0.8 eV observed in the photoluminescence spectra of films deposited at $T_{dep} = 460°C$ is correlated to strain in the epitaxial films is

based on comparable literature data only. A direct proof of strain or stress in the films by X-ray diffraction or Raman spectroscopy with higher resolution would allow for a verification of this hypothesis.

In order to verify that the defect formation mechanisms discussed in this work are a general phenomena of low temperature epitaxy, investigations of the structural defects of films deposited in other MBE-systems or CVD-based processes should be carried out. With respect to the required film thickness for defect characterization, electron cyclotron resonance CVD [178,179] and hot-wire CVD [180,181] are the most promising candidates for a comparative study due to the high deposition rates of up to 0.3 μm/min reported for both deposition methods.

Concerning the application of low temperature epitaxy to solar cell mass production using the concept of epitaxial thickening of laser crystallized seed layers, the presented results suggest that only epitaxy on large grained seed layers with preferred (100)-surface orientation might be successful. Here, enhanced efforts in the development of the crystallization process for the production of preferred seed layers is required, as well as the development of an applicable surface cleaning and oxide-removal process with low thermal budget, that is compatible with the substrate material.

Appendix A: Analytical model of the quantum efficiency

The model for the calculation of the internal quantum efficiency (IQE) is based on the model for the calculation of the external quantum efficiency given in [167]. The model assumes an abrupt pn-junction solar cell with constant doping on each side. The given contributions of the emitter (n-type), the space charge region (SCR) and the base (p-type) are the solutions of the continuity and current density equations.

The width of the junction or space charge region (SCR) W_j is given by

$$W_j = \sqrt{\frac{2\epsilon_0\epsilon_r(N_A + N_D)V_{bi}}{qN_AN_D}},\tag{1}$$

with V_{bi} the build in voltage. The value x_j denotes the width of the neutral emitter, i.e. the emitter thickness W_e minus the fraction of the SCR width in the emitter

$$x_j = W_e - W_j\frac{N_A}{N_A + N_D}.\tag{2}$$

The value H' denotes the width of the neutral base, i.e. the base thickness W_b minus the fraction of the SCR in the base

$$H' = W_b - W_j\frac{N_D}{N_A + N_D}.\tag{3}$$

The front surface recombination of the cell is given by S_p, the rear surface recombination by S_n. The diffusion coefficient is denoted by $D_{n,p}$ and the minority carrier diffusion length by $L_{n,p}$, for electrons and holes respectively. The absorption coefficient is denoted by α.

Emitter contribution

$$IQE_{emitter} = \frac{\alpha L_p}{\alpha^2 L_p^2 - 1}$$

$$\times \left\{ \frac{(R_p + \alpha L_p) - \exp(-\alpha x_j)[R_p \cosh(x_p) + \sinh(x_p)]}{R_p \sinh(x_p) + \cosh(x_p)} - \alpha L_p \exp(-\alpha x_j) \right\}, \quad (4)$$

where $R_p = S_p L_p / D_p$ and $x_p = x_j / L_p$.

Base contribution

$$IQE_{base} = \frac{\alpha L_n}{\alpha^2 L_n^2 - 1} \exp[-\alpha(x_j + W_j)]$$

$$\times \left\{ \alpha L_n - \frac{R_n[\cosh(x_n) - \exp(-\alpha H')] + \sinh(x_n) + \alpha L_n \exp(-\alpha H')}{R_n \sinh(x_n) + \cosh(x_n)} \right\}, \quad (5)$$

where $R_n = S_n L_n / D_n$ and $x_n = H' / L_n$.

Space charge region contribution

(Under the assumption, that no recombination in the SCR occurs.)

$$IQE_{SCR} = \exp(-\alpha x_j)[1 - \exp(\alpha W_j)] \quad (6)$$

IQE

The total IQE finally is the sum of the equations 4, 5, and 6

$$IQE = IQE_{emitter} + IQE_{base} + IQE_{SCR}. \quad (7)$$

Abbreviations and symbols

Abbreviations

BAYSIX	block cast silicon from Bayer AG, Germany
BE	bound exciton
CV	capcitance–voltage
CVD	chemical vapor deposition
CZ-Si	Czochralski-grown silicon
DAS	dimer-adatom-stacking fault
DLTS	deep level transient spectroscopy
EBSD	electron back scattering diffraction
ECR-CVD	electron cyclotron resonance chemical vapor deposition
EHD	electron hole droplet
EQE	external quantum efficiency
FE	free exciton
HWCVD	hot wire chemical vapor deposition
IAD	ion-assisted deposition
IBD	ion-beam deposition
IBSD	ion-beam sputter deposition
IDLS	injection dependent lifetime spectroscopy
IQE	internal quantum efficiency
LBIC	light beam induced current
LLI	low level injection
LPCVD	low pressure chemical vapor deposition
LPE	liquid phase epitaxy

MBE	molecular beam epitaxy
MWPCD	microwave-detected photoconductance decay
PL	photoluminescence
PECVD	plasma enhanced chemical vapor deposition
PVD	physial vapor deposition
RIE	reactive ion etching
SIMS	secondary ion mass spectrometry
SPE	solid phase epitaxy
SRH	Shockley-Read-Hall
TDLS	temperature dependent lifetime spectroscopy
TEM	transmisson electron micrograph
TQE	temperature dependent quantum efficiency
UHV	ultra high vacuum
XTEM	cross sectional transmisson electron micrograph

Symbols

A_{def}	characteristic defect constant
B_{DLTS}	DLTS proportional constant
C_n (C_p)	electron (hole) Auger coefficient $(\text{cm}^6\text{s}^{-1})$
C_j	junction capacitance (pF)
D	diffusion coefficient (cm^2/s)
$e_p, (e_n)$	emisson frequency of holes (electrons) (Hz)
E_a	TQE activation energy (eV)
E_{act}	DLTS activation energy (eV)
E_C	conduction band energy (eV)
E_F	Fermi energy (eV)
E_g	band gap (eV)
E_i	intrinsic Fermi level (eV)
E_t	defect or trap level (eV)
E_V	valence band energy (eV)
f_p	repetion frequncy (Hz)
$f(\lambda, T)$	correction factor for the absorption coefficient
FF	fill factor (%)
G	gerneration rate $(\text{cm}^{-3}\text{s}^{-1})$
G_0	thermal gerneration rate $(\text{cm}^{-3}\text{s}^{-1})$
h	Planck's constant $(6.626 \times 10^{-34} \text{ Js})$
h_{epi}	critical epitaxial thickness (nm)
$h\nu$	photon energy (eV)
I_{PLbtb}	band to band photoluminescence intensity
I_{SC}	short circuit current (mA)
j_{SC}	short circuit current (mAcm^{-2})
k_B	Boltzmann constant $(1.38 \times 10^{-23} \text{ JK}^{-1})$
L	carrier diffusion length (μm)
L_{eff}	effective carrier diffusion length (μm)
m_{tc}^*	thermal velocity effective mass
n	electron concentration (cm^{-3})
n_0	equilibrium electron concentration (cm^{-3})
n_1	Shockley-Read-Hall electron concentration (cm^{-3})
n_i	intrinsic carrier concentration (cm^{-3})
$n_S, (p_S)$	surface electron (hole) concentration (cm^{-3})
Δn	excess electron concentration (cm^{-3})
Δn_S	excess surface electron concentration (cm^{-3})

N_A (N_D)	aceptor (donator) dopant concentraion (cm^{-3})
N_C (N_V)	effective density of states in the conduction (valence) band (cm^{-3})
N_C^{300K} (N_V^{300K})	effective density of states in the conduction (valence) band at room temperature (cm^{-3})
N_S	density of defect states at the surface (cm^{-2})
N_{D0}	background doping density (cm^{-2})
N_S	density of surface states (cm^{-2})
N_t	trap density (cm^{-3})
p	hole concentration (cm^{-3})
p_0	equilibrium hole concentration (cm^{-3})
p_1	Shockley-Read-Hall hole concentration (cm^{-3})
Δp	excess hole concentration (cm^{-3})
q	elementary charge (1.6×10^{-19} C)
r_{dep}	deposition rate ($\mu\text{m/min}$)
R	reflexion
S	surface recombination velocity (cm/s)
t	time (s)
T	temperature (K or °C)
T_{dep}	deposition temperature (°C)
T_{EQE}	external quantum efficieny measurement temperature (K)
T_{PL}	photoluminescence measurement temperature (K)
U	net recombination rate ($\text{cm}^{-3}\text{s}^{-1}$)
U_0	equilibrium recombination rate ($\text{cm}^{-3}\text{s}^{-1}$)
U_{Aug}	Auger recombination rate ($\text{cm}^{-3}\text{s}^{-1}$)
U_{rad}	radiative recombination rate ($\text{cm}^{-3}\text{s}^{-1}$)
U_S	surface recombination rate ($\text{cm}^{-2}\text{s}^{-1}$)
U_{SRH}	Shockley-Read-Hall recombination rate ($\text{cm}^{-3}\text{s}^{-1}$)
v_{th}	thermal velocity of the charge carriers (cm/s)
V_{acc}	acceleration voltage (V)
V_{OC}	open circuit voltage (mV)
W	film thickness (μm)
W_b	thickness of the photovoltaic active base (μm)
W_j	space charge region width (μm)
$W_{j,b}$	space charge region width under bias voltage (μm)
α	absorption coefficient (cm^{-1})
Φ_{ph}	photon flux ($\text{cm}^{-2}\text{s}^{-1}$)

η	conversion efficiency (%)
κ	$= N_V^{300K}/N_A$ (case A), $= \tau_{p0}^{300K} N_C^{300K}/(\tau_{n0}^{300K} N_A)$ (case B)
λ	wavelength (nm)
$\mu_n,(\mu_p)$	electron (hole) mobility (cm^2/Vs)
μ_n^{300}	electron mobility at room temperature (cm^2/Vs)
ν	frequency (s^{-1})
θ	normalized temperature ($T/300K$)
σ_n (σ_p)	elctron (hole) capture cross section (cm^2)
τ	carrier lifetime (s)
$\tau_{n0},(\tau_{p0})$	time constant for electron (hole) capture (s)
$\tau_{n0}^{300K},(\tau_{p0}^{300K})$	electron (hole) reference lifetime (μs)
τ_{eff}	effective carrier lifetime (s)
τ_{Aug}	Auger carrier lifetime (s)
τ_{rad}	radiative carrier lifetime (s)
τ_{SRH}	Shockley-Read-Hall lifetime (s)
τ_{SRH}^{LLI}	Shockley-Read-Hall lifetime under low level injection (μs)
$\tau_{SRH}^{LLI,p}$	Shockley-Read-Hall lifetime under low level injection in p-type material (μs)

Publication list

1. *Thin Film Solar Cells on Glass by Transfer of Quasi-Monocrystalline Si Films*
   R. B. Bergmann, T. J. Rinke, T. A. Wagner, and J. H. Werner
   in Techn. Dig. Int. PVSEC11 (Sapporo, 1999) p. 541-542.

2. *Ion-Assisted Deposition of Silicon Epitaxial Films with High Deposition Rate using Low Energy Silicon Ions*
   L. Oberbeck, T. A. Wagner, and R. B. Bergmann,
   Mat. Res. Soc. Symp. Proc. 609, A7.1.1 (2000).

3. *Thin Film Solar Cells on Glass Based on the Transfer of Monocrystalline Si Films*
   R. B. Bergmann, T. J. Rinke, T. A. Wagner, and J. H. Werner,
   Solar Energy Materials and Solar Cells 65, 355-361 (2001).

4. *High-Quality, Low-Temperature Epitaxial Si Films Deposited at Very High Deposition rate*
   R. B. Bergmann, L. Oberbeck, and T. A. Wagner,
   J. Cryst. Growth 225, 335 (2001).

5. *High-rate Deposition of Epitaxial Layers for Efficient Low-Temperature Thin Film Epitaxial Silicon Solar Cells*
   L. Oberbeck, J. Schmidt, T. Wagner, and R. B. Bergmann,
   Progr. Photovolt. Res. Applic. 9, 333-340 (2001).

6. *Intra Grain Defects - Limiting Factor for Low Temperature Polycrystalline Silicon Films*
   T. A. Wagner, L. Oberbeck, R. B. Bergmann, and J. H. Werner,
   Solid State Phenomena 80-81, 95-100 (2001).

7. *Orientation-Dependence of Low Temperature Epitaxial Silicon Growth*
   T. A. Wagner, L. Oberbeck, M. Nerding, H. P. Strunk, and R. B. Bergmann,
   Mat. Res. Soc. Symp. Proc. 664, A22.3 (2001).

8. *Low Temperature Epitaxial Silicon Films Deposited by Ion-Assisted Deposition*
   T. A. Wagner, L. Oberbeck, and R. B. Bergmann,
   Mat. Sci. Eng. B 89, 319 (2002).

9. *The Single - Poly Crystalline Instability in Silicon Growth by Ion Assisted Deposition at Low Temperatures*

M. Nerding, S. Christiansen, L. Oberbeck, T. A. Wagner, R. B. Bergmann, J. H. Werner, and H. P. Strunk,
J. Appl. Phys. 93, 2570 (2003).

10. *Low-temperature Epitaxy on Polycrystalline Silicon-Substrates*
T. A. Wagner, L. Oberbeck, R. B. Bergmann, M. Nerding, H. P. Strunk, and J. H. Werner,
Solid State Phenomena (2003), in print.

11. *A simple method to extract the diffusion length from the output parameters of solar cells - application to polycrystalline silicon*
K. Taretto, U. Rau, T. A. Wagner, and J. H. Werner,
Solid State Phenomena (2003), in print

12. *Flexible monocrystalline Si films for thin film devices from transfer processes*
C. Berge, T. A. Wagner, W. Brendle, C. Craff Castillo, M. B. Schubert, and J. H. Werner,
Mat. Res. Soc. Symp. Proc. 769, H2.7.1-H2.7.6 (2003).

13. *Temperature-Dependent Quantum Efficiency Analysis of Recombination Centers in Silicon Thin-Film Solar Cells*
T. A. Wagner and U. Rau,
in Proc. 3rd World Conf. Photovolt. Energy Conv. (2003), in print.

14. *Analysis of Recombination Centers in Epitaxial Silicon Thin-Film Solar Cells by Temperature dependent Quantum Efficiency Measurements*
T. A. Wagner and U. Rau,
Appl. Phys. Lett. 82, 2637 (2003).

References

[1] A. Slaoui, J. Poortmans, and M. Caymax, in *Growth, Characterization and Electronic Applications of Si-based Thin Films*, edited by R. B. Bergmann (Research Signpost, Trivandrum, India, 2002), p. 147.

[2] G. Masini, L. Colace, and G. Assanto, Mat. Sci. Eng. B **89**, 2 (2002).

[3] U. König, in *Properties of Silicon Germanium and SiGe:Carbon*, edited by E. Kasper and K. Lyutovich (emis datareview series no. 24, Short Run Press Ltd., Exeter, 2000), p. 319.

[4] R. B. Bergmann and J. H. Werner, Thin Solid Films **403-404**, 162 (2002).

[5] R. B. Bergmann, R. M. Hausner, N. Jensen, M. Grauvogl, L. Oberbeck, T. J. Rinke, M. B. Schubert, C. Zaczek, R. Dassow, J. R. Köhler, U. Rau, S. Oelting, J. Krinke, H. P. Strunk, and J. H. Werner, in *Proc. 2nd World Conf. On Photovolt. Energy Conv.*, edited by J. Schmidt, H. A. Ossenbrink, P. Helm, H. Ehmann, and E. D. Dunlop (E. C. Joint Res. Centre, Luxembourg, 1998), p. 1260.

[6] S. Oelting, D. Martini, D. Bonnet, in: L.Guimaraes, W. Palz, C. Dereyff, H. Kiess and P. Helm, in 11th *E. C. Photovoltaic Solar Energy Conference* (Harwood Academic Publishers, Chur, 1992), p. 491.

[7] L. Oberbeck, *Ionenassistierte Deposition von Siliciumschichten*, Ph.D thesis (in German), University of Stuttgart, Germany, 2001.

[8] R. B. Bergmann, *Kristallisation von Silicium auf Glas: Schlüsseltechnologie für die Photovoltaik*, professorial dissertation (in German), University of Freiburg, Germany 1997.

[9] G. L. Olson and J. A. Roth, Materials Science Reports **3**, 1 (1988).

[10] H. O. Pierson, *Handbook of chemical vapor deposition* (Noyes, Park Ridge, 1992).

[11] L. Oberbeck, T. A. Wagner, and R. B. Bergmann, Mat. Res. Soc. Symp. Proc. **609**, A7.1.1 (2000).

[12] D. K. Herman and H. Sitter, *Molecular Beam Epitaxy* (Springer-Verlag, Heidelberg, 1996), p. entire issue.

[13] J. W. Rabalais, A. H. Al-Bayati, K. J. Boyd, D. Marton, J. Kulik, Z. Zhang, and W. K. Chu, Phys. Rev. B **53**, 10781 (1996).

[14] L. Oberbeck and R. B. Bergmann, Vacuum Solutions **18**, 31 (2000).

[15] G. Eifler, E. Kasper, K. Ashurov, and S. Morozov, J. Vac. Sci. Technol. A **20**, 945 (2002).

[16] J. E. Greene, S. A. Barnett, J.-E. Sundgren, and A. Rockett, in *Ion Beam Assisted Film Growth*, edited by T. Itoh (Elsevier, Amsterdam, 1989), Chap. 5, p. 101.

[17] M. V. R. Murty and H. A. Atwater, Phys. Rev. B **45**, 1507 (1992).

[18] M. Kitabatake and J. E. Greene, J. Appl. Phys. **73**, 3183 (1993).

[19] K. J. Boyd, D. Marton, J. W. Rabalais, S. Uhlmann, and T. Frauenheim, J. Vac. Sci. Technol. A **16**, 444 (1998).

[20] K. J. Boyd, D. Marton, J. W. Rabalais, S. Uhlmann, and T. Frauenheim, J. Vac. Sci. Technol. A **16**, 463 (1998).

[21] R. Ditchfield and E. G. Seebauer, Phys. Rev. Lett. **82**, 1185 (1999).

[22] W. Shindo and T. Ohmi, J. Appl. Phys. **79**, 2347 (1996).

[23] N.-E. Lee, G. Xue, and J. E. Greene, J. Appl. Phys. **80**, 769 (1996).

[24] M. Mundschau, E. Bauer, W. Telieps, and W. Swiech, Surf. Sci. **223**, 413 (1989).

[25] R. Schwoebel and E. Shipsey, J. Appl. Phys. **37**, 3682 (1966).

[26] S. Heun, J. Falta, and M. Henzler, Surf. Sci. **243**, 132 (1991).

[27] C. Schelling, *Growth and characterization of self-organized and "organized" Si and $Si_{1-x}Ge_x$ nanostructures*, Ph.D thesis, Johannes-Kepler-University Linz, Austria, 2000.

[28] H.-J. Gossmann and L. C. Feldman, Phys. Rev. B **32**, 6 (1985).

[29] H. Jorke, H.-J. Herzog, and H. Kibbel, Phys. Rev. B **40**, 2005 (1989).

[30] D. J. Eaglesham, H.-J. Gossmann, and M. Cerullo, Phy. Rev. Lett. **65**, 1227 (1990).

[31] W. J. Varhue, J. L. Rogers, and P. S. Andry, Appl. Phys. Lett. **68**, 349 (1996).

[32] N.-E-Lee, G. A. Tomasch, and J. E. Greene, Appl. Phys. Lett. **65**, 3236 (1994).

[33] D. J. Eaglesham, J. Appl. Phys. **77**, 3597 (1995).

[34] M. V. R. Murty, H. A. Atwater, A. J. Kellock, and J. E. E. Baglin, Appl. Phys. Lett. **62**, 2566 (1993).

[35] M. E. Taylor, H. A. Atwater, and M. V. R. Murty, Thin Solid Films **324**, 85 (1998).

[36] A. I. Nikiforov, B. Z. Kanter, and O. P. Pchelyakov, Thin Solid Films **336**, 179 (1998).

[37] M. Bauer, M. Oehme, and E. Kasper, Mat. Sci. Eng. B **89**, 263 (2002).

[38] M. Nerding, S. Christiansen, L. Oberbeck, T. A. Wagner, R. B. Bergmann, J. H. Werner, and H. P. Strunk, J. Appl. Phys. (2003), in print .

[39] J. Platen, B. Selle, I. Sieber, S. Brehme, U. Zeimer, and W. Fuhs, Thin Solid Films **381**, 22 (2001).

[40] J. Thiesen, H. M. Branz, and R. S. Crandall, Appl. Phys. Lett. **77**, 3589 (2000).

[41] C. H. Seager and R. A. Anderson, Appl. Phys. Lett. **53**, 1181 (1988).

[42] M. V. R. Murty and H. A. Atwater, Phys. Rev. B **49**, 8483 (1994).

[43] S. Coffa, A. Polman, and R. N. Schwartz, *Rare Earth Doped semiconductors II*, Mat. Res. Soc. Symp. Proc. **422**, entire issue (1996).

[44] S. Mahajan and K. S. S. Harsha, *Priciples of Growth and Processing of Semiconductors* (McGraw-Hill, Singapore, 1999), p. 268ff.

[45] J. Friedel, *Dislocations* (Pergamon Press, London, Oxford, 1964), p. 18ff.

[46] D. L. Smith, *Thin Film Deposition: Priciples and Practice* (McGraw-Hill, Singapore, 1995), p. 279.

[47] J. Weber, Solid State Phenomena **37-38**, 13 (1994).

[48] E. R. Weber and H. Alexander, J. Physique Colloq. **C4**, C4 319 (1983).

[49] N. Letho, Phys. Rev. B **55**, 15601 (1997).

[50] P. Y. Yu and M. Cardona, *Fundamentals of Semiconductors: Physics and Materials Properties* (Springer, Berlin, 1996), p. 339.

[51] P. J. Dean, J. R. Haynes, and W. F. Flood, Phys. Rev. **161**, 711 (1967).

[52] G. Davies, Physics Reports **176**, 83 (1989).

[53] M. A. Vouk and E. C. Lightowlers, J. Phy. C **10**, 3689 (1977).

[54] J.-P. Noël, N. L. Rowell, and J. E. Greene, J. Appl. Phys. **77**, 4623 (1995).

[55] R. Sauer, Solid State Commun. **14**, 481 (1974).

[56] R. B. Hammond and R. N. Silver, Phys. Rev. Lett. **42**, 523 (1979).

[57] J. Friedel, *Dislocations* (Pergamon Press, London, Oxford, 1964), p. 427ff.

[58] N. A. Drozdov, A. A. Patrin, and V. D. Tkachev, JETP Lett. **23**, 597 (1976).

[59] R. Sauer, J. Weber, J. Stolz, E. R. Weber, K.-H. Küsters, and H. Alexander, Appl. Phys. A **36**, 1 (1985).

[60] V. Higgs, E. C. Lightowlers, G. Davies, F. Schaeffler, and E. Kasper, Semicond. Sci. Technol. **4**, 593 (1989).

[61] E. C. Lightowlers and V. Higgs, Phys. Stat. Sol. **138**, 665 (1993).

[62] H. Weman, J. L. Lindström, G. S. Oehrlein, and B. G. Svensson, J. Appl. Phys. **67**, 1013 (1990).

[63] A. Dörnen, G. Pensl, and R. Sauer, Phys. Rev. B **35**, 9318 (1987).

[64] K. Thonke, G. D. Watkins, and R. Sauer, Solid State Comm. **51**, 127 (1984).

[65] J. Wagner, K. Thonke, and R. Sauer, Phys. Rev. B **29**, 7051 (1984).

[66] N. S. Minaev and A. V. Mudryi, Phys. Status Solidi **68**, 561 (1981).

[67] J. Weber and R. Sauer, Mater. Res. Soc. Symp. Proc. **14**, 165 (1983).

[68] N. Magnea, A. Lazrak, and J. L. Pautrat, Appl. Phys. Lett **45**, 60 (1984).

[69] J. Wagner, A. Dörnen, and R. Sauer, Phys. Rev. B **31**, 5561 (1985).

[70] K. P. O'Donnell, K. M. Lee, and G. D. Watkins, Physica B **116**, 258 (1983).

[71] V. T. Tkachev and A. V. Mudryi, Inst. Phys. Conf. Ser. **31**, 231 (1977).

[72] Z. Ciechanowska, G. Davies, and E. C. Lightowlers, Solid State Commun. **49**, 427 (1984).

[73] E. C. Lightowlers, L. T. Canham, G. Davies, M. L. W. Thewalt, and S. P. Watkins, Phys. Rev. B **29**, 4517 (1984).

[74] E. C. Lightowlers, Semicond. Sci. Technol. **5**, 1161 (1990).

[75] E. C. Lightowlers, M. J. Gregson, V. Higgs, S. T. Davey, C. J. Gibbings, and C. G. Tuppen, Materials Science Forum **38-41**, 379 (1989).

[76] N. L. Rowell, D. C. Houghton, J.-P. Noël, and J. E. Greene, Thin Solid Films **184**, 69 (1990).

[77] W.-X. Ni, G. Hansson, J. Cardenas, and B. Svensson, Thin Solid Films **321**, 131 (1998).

[78] R. B. Young and N. R. Rowell, Proc. SPIE **1145**, 80 (1989).

[79] D. J. Robbins, R. A. A. Kubiak, and E. H. C. Parker, J. Vac. Sci. Technol. B **3**, 588 (1985).

[80] L. Vescan, T. Stoica, and B. Holländer, Mat. Sci. Eng. B **89**, 49 (2002).

[81] J. Weber, W. Schmid, and R. Sauer, Phys. Rev. B **21**, 2401 (1980).

[82] A. V. Mudryi, A. I. Patuk, I. A. Shakin, A. G. Ulyashin, R. Job, W. R. Fahrner, A. Fedotov, A. Mazanik, and N. A. Drozdov, Solar Energy Materials and Solar Cells **72**, 503 (2002).

[83] A. Misiuk, H. B. Surma, I. V. Antonova, V. P. Popov, J. Bak-Misiuk, M. Lopez, A. Romano-Rodriguez, A. Barcz, and J. Jun, Solid State Phenomena **69-70**, 345 (1999).

[84] H. Bender and J. Vanhellemont, in *Handbook on Semiconductors*, edited by S. Mahajan (Elsevier, Amsterdam, 1994), Vol. 3B, p. 1637.

[85] C. S. Fuller and R. A. Logan, J. Appl. Phys. **28**, 1427 (1957).

[86] W. Kaiser, H. L. Frisch, and H. Reiss, Phys. Rev. **112**, 1546 (1958).

[87] L. C. Kimerling and J. L. Benton, Appl. Phys. Lett. **39**, 410 (1981).

[88] W. Götz, G. Pensl, and W. Zulehner, Phys. Rev. B **46**, 4312 (1992).

[89] N. M. Johnson and S. K. Hahn, Appl. Phys. Lett. **48**, 709 (1986).

[90] D. I. Bohne and J. Weber, Phys. Rev. B **47**, 4037 (1993).

[91] Y. J. Lee, J. von Boehm, M. Pesola, and R. M. Nieminen, Phys. Rev. B **65**, 85205 (2002).

[92] K. Wada, Phys. Rev. B **30**, 5884 (1984).

[93] G. Pensl, M. Schulz, W. Bergholz, and J. L. Hutchison, Appl. Phys. A **48**, 49 (1989).

[94] L. C. Kimerling, M. T. Asom, J. L. Benton, P. J. Drevinsky, and C. E. Caefer, Mater. Sci. Forum **38-41**, 141 (1989).

[95] A. A. Istratov, C. Flink, H. Hieslmair, T. Heiser, and E. R. Weber, Appl. Phys. Lett. **71**, 2121 (1997).

[96] A. A. Istratov, H. Hieslmair, and E. R. Weber, Appl. Phys. A **69**, 13 (1999).

[97] K. Graff, *Metal impurities in silicon device fabrication* (Springer, Berlin, 1995), p. entire issue.

[98] M. S. Tyagi, *Introduction to Semiconductor Materials and Devices* (Wiley-Interscience, New York, 1991), p. 69.

[99] S. M. Sze, *Physics of Semiconductor Devices 2nd Edition* (Wiley-Interscience, New York, 1981), p. 17.

[100] W. Gerlach, H. Schlangenotto, and H. Maeder, phys. stat. sol. (a) **13**, 277 (1972).

[101] R. J. Nelson and R. G. Sobers, J. Appl. Phys. **49**, 6103 (1978).

[102] W. Shockley and W. T. Read, Phys. Rev. **87**, 835 (1952).

[103] R. N. Hall, Phys. Rev. **87**, 387 (1952).

[104] J. Dziewior and W. Schmid, Appl. Phys. Lett. **31**, 346 (1977).

[105] J. D. Beck and R. Conradt, Solid State Commun. **13**, 93 (1973).

[106] A. Hangleiter and R. Häcker, Phys. Rev. Lett. **65**, 215 (1990).

[107] R. Häcker and A. Hangleiter, J. Appl. Phys. **75**, 7570 (1994).

[108] J. Schmidt, *Untersuchungen zur Ladungsträgerrekombination an den Oberflächen und im Volumen von kristallinen Silicium-Solarzellen*, Ph.D thesis (in German), University of Hannover, Germany, 1998.

[109] A. Hangleiter, *Rekombination und Korrelation intrinsicher elektronischer Anregungen in Halbleitern*, professorial dissertation (in German), University of Stuttgart, Germany, 1992, Habilitationsschrift, Universität Stuttgart.

[110] M. Lax, Phys. Rev. **119**, 1502 (1960).

[111] T. N. Morgan, Phys. Rev. B **28**, 7141 (1983).

[112] C. Herring, in *Structure and Properties for Solid Surfaces*, edited by R. G. Gomer and C. S. Smith (University of Chicago Press, Chicago, 1953), Chap. 1.

[113] J. Dabrowski and H.-J. Müssig, *Silicon Surfaces and Formation of Interfaces* (World Scientific, Singapore, 2000), p. 49.

[114] A. A. Baski, S. C. Erwin, and L. J. Whitman, Surface Science **392**, 69 (1997).

[115] R. M. Tromp, R. J. Hamers, and J. E. Demuth, Phys. Rev. Lett. **55**, 1303 (1985).

[116] S. Kitamura and M. Iwatsuji, Jap. J. Appl. Phys. **35**, L668 (1996).

[117] W. S. Yang, F. Jona, and P. M. Marcus, Solid State Commun. **43**, 847 (1982).

[118] D. J. Chadi, Phys. Rev. Lett. **43**, 43 (1979).

[119] C. Roland and G. H. Gilmer, Phys. Rev. B **46**, 13428 (1992).

[120] R. M. Tromp and M. C. Reuter, Phys. Rev. Lett. **68**, 820 (1992).

[121] D. J. Chadi, Phys. Rev. Lett. **59**, 1691 (1987).

[122] J. Dabrowski and H.-J. Müssig, *Silicon Surfaces and Formation of Interfaces* (World Scientific, Singapore, 2000), p. 172.

[123] Y. W. Mo and M. G. Lagally, Surf. Sci. **248**, 313 (1991).

[124] Y. Yamamoto, surfr. Sci. **313**, 155 (1994).

[125] T. Ichinokawa, H. Ampo, S. Miura, and A. Tamura, Phys. Rev. B **31**, 5183 (1985).

[126] B. Z. Olshanetzky and V. I. Mashanov, Surf. Sci. **111**, 414 (1981).

[127] J. Dabrowski and H.-J. Müssig, in *Proc. of the 23rd International Conference on the Physics of Semiconductors*, edited by M. Scheffler and R. Zimmermann (World Scientific, Singnapore, 1996), p. 795.

[128] J. J. Lander, G. W. Gobeli, and J. Morrison, J. Appl. Phys. **34**, 2298 (1963).

[129] R. E. Schlier and H. E. Farnsworth, J. Chem. Phys. **30**, 917 (1959).

[130] K. Takayanagi, Y. Tanishiro, M. Takahashi, and S. Takahashi, Surf. Sci. **164**, 367 (1985).

[131] K. Takayanagi, Y. Tanishiro, M. Takahashi, and S. Takahashi, J. Vac. Sci. Technol. A **3**, 1502 (1985).

[132] J. Dabrowski and H.-J. Müssig, *Silicon Surfaces and Formation of Interfaces* (World Scientific, Singapore, 2000), p. 73.

[133] W. Kern and D. A. Puotinen, RCA Rev. **6**, 187 (1970).

[134] D. C. Streit and F. G. Allen, J. Appl. Phys. **61**, 2894 (1987).

[135] S. Klein, *Wasserstoff und Ultraschallbehandlung von polykristallinem Silicium*, diploma thesis (in German), Institut für Physikalische Elektronik, University of Stuttgart, Germany, 1999.

[136] D. V. Lang, J. Appl. Phys. **45**, 3023 (1974).

[137] H. Rauh, *Wacker's Atlas for Characterization of Defects in Silicon* (Wacker Siltronic AG, Burghausen, Germany).

[138] F. S. d'Aragona, J. Electrochem. Soc. **119**, 948 (1972).

[139] G. Nomarski and A. R. Weill, Bul. Soc. Franc. Miner. Cryst **77**, 840 (1954).

[140] R. Brendel and R. Plieninger, in *Technical Digest 9th International Photovoltaic Science and Engineering Conference* (Arisumi Printing, Japan, 1996), p. 223.

[141] R. Plieninger, *Rekristallisierte Siliciumschichten für Solarzellenanwendungen*, Ph.D thesis (in German), University of Stuttgart, Germany, 1998.

[142] L. Jayanathan, G. Davies, and E. C. Lightowlers, Phys. Rev. B **52**, 10923 (1995).

[143] M. Eswaran, B. Bergersen, J. A. Rostworowski, and R. R. Parsons, Solid State Commun. **20**, 811 (1976).

[144] G. Bilger, private communication.

[145] R. G. Wilson, F. A. Stevie, and C. W. Magee, *Secondary ion mass spectrometry: a practical handbook for depth profiling and bulk impurity analysis* (Wiley-Interscience, New York, 1989), p. Appendix F.

[146] A. A. Istratov and E. R. Weber, Appl. Phys. A **66**, 123 (1998).

[147] A. A. Istratov, H. Hieslmair, and E. R. Weber, Appl. Phys. A **70**, 489 (2000).

[148] W. Staiger, G. Pfeiffer, K. Weronek, A. Höppner, and J. Weber, Material Science Forum **143-147**, 1571 (1994).

[149] R. B. Bergmann, L. Oberbeck, and T. A. Wagner, J. Cryst. Growth **255**, 335 (2001).

[150] G. A. Somorjai, *Introduction to surface chemistry and catalysis* (Wiley-Interscience, New York, 1994), p. 336.

[151] Y. Ota, J. Elektrochem. Soc. **124**, 1795 (1977).

[152] E. Kasper, M. Bauer, and M. Oehme, Thin Solid Films **321**, 148 (1998).

[153] D. K. Herman and H. Sitter, *Molecular Beam Epitaxy* (Springer-Verlag, Heidelberg, 1996), p. 5.

[154] F. Shimura, T. Okui, and T. Kusama, J. Appl. Phys. **67**, 7168 (1990).

[155] Y. Kirino, A. Buczkowski, Z. J. Radzimski, G. A. Rozgonyi, and F. Shimura, Appl. Phys. Lett. **57**, 2832 (1990).

[156] J. Schmidt, C. Berge, and A. G. Aberle, Appl. Phys. Lett. **73**, 2167 (1998).

[157] H. Bleichner, P. Jonsson, N. Keskitalo, and E. Nordlander, J. Appl. Phys. **79**, 9142 (1996).

[158] S. Rein, T. Rehrl, W. Warta, and S. W. Glunz, J. Appl. Phys. **91**, 2059 (2002).

[159] R. G. Humphreys, J. Phys. C **14**, 2935 (1981).

[160] S. M. Sze, *Physics of Semiconductor Devices 2nd Edition* (Wiley-Interscience, New York, 1981), p. 21.

[161] R. H. Bube, *Photoelectronic Properties of Semiconductors* (Cambridge University Press, Cambridge, 1992), p. 68.

[162] K. L. Luke and L.-J. Cheng, J. Appl. Phys. **61**, 2282 (1987).

[163] R. A. Sinton and A. Cuevas, Appl. Phys. Lett. **69**, 2510 (1996).

[164] K. Rajkanan, R. Singh, and J. Shewchun, Solid State Electronic **22**, 793 (1979).

[165] Y. P. Varshni, Physica **34**, 149 (1967).

[166] M. A. Green, *High Efficiency Cells* (Trans Tech Publications, Aedermannsdorf, Switzerland, 1987), p. 228.

[167] H. J. Hovel, in *Solar Cells*, edited by R. K. Willardson and A. C. Beer (Academic Press, New York, 1975), Vol. 11, p. 18f.

[168] F. J. Morin and J. P. Maita, Phys. Rev. **96**, 28 (1954).

[169] M. A. Green, J. Appl. Phys. **67**, 2944 (1990).

[170] D. A. Clugston and P. A. Basore, in *26th IEEE Photovoltaic Specialists Conference* (IEEE, Piscataway, 1997), pp. 207–210.

[171] J. A. Venables and C. J. Harland, Phil. Mag. **27**, 1193 (1973).

[172] W. Ranke, Phys. Rev. B **41**, 5243 (1990).

[173] L. Oberbeck, J. Schmidt, T. A. Wagner, and R. B. Bergmann, Prog. Photovolt: Res. Appl. **9**, 333 (2001).

[174] M. Nerding, R. Dassow, S. Christiansen, J. R. Köhler, J. Krinke, J. H. Werner, and H. P. Strunk, J. Appl. Phys. **91**, 4125 (2002).

[175] P. Lengsfeld, S. Christiansen, M. Nerding, M. Rebien, W. Henrion, I. Sieber, and N. H. Nickel, Solid State Phenomena **80-81**, 181 (2001).

[176] M. Nerding, S. Christiansen, G. Esser, U. Urmoneit, A. Otto, and H. P. Strunk, Mat. Res. Soc. Symp. Proc. **685E**, D.11.4.6 (2001).

[177] J. H. Comfort, L. M. Garverick, and R. Reif, J. Appl. Phys. **62**, 3388 (1987).

[178] S. J. DeBoer, V. L. Dalal, G. Chumanov, and R. Bartels, Appl. Phys. Lett. **66**, 2528 (1995).

[179] E. Conrad, L. Elstner, W. Fuhs, W. Henrion, P. Müller, J. Poortmans, B. Selle, and U. Zeimer, in *14th European Photovoltaic Solar Energy Conference*, edited by H. A. Ossenbrink, P. Helm, and E. Ehmann (Stephens & Assoc., Bedford, 1997), p. 1441.

[180] J. Thiesen, E. Iwaniczko, K. M. Jones, A. Mahan, and R. S. Crandall, Appl. Phys. Lett. **75**, 992 (1999).

[181] H. Seitz and B. Schroder, Solid State Comm. **116**, 625 (2000).

Curriculum Vitae

Persönliche Angaben

Name:	Thomas Alexander Georg Wagner
Geburtsort:	Nürnberg
Geburtstag:	10. Januar 1971
Familienstand:	Ledig

Schulbildung

1977 - 1981:	Grundschule Altdorf
1981 - 1990:	Leibniz-Gymnasium Altdorf
05.1990:	Abitur

Ersatzdienst

1991 - 1992:	Bayerisches Rotes Kreuz Nürnberger Land, Rettungsdienst

Studium

1992 - 1995:	Physikstudium an der Universität Bayreuth
10.1994:	Vordiplom Physik
1995 - 1996:	Physikstudium an der Université J. Fourier Grenoble
1996 - 1998:	Physikstudium an der Universität Bayreuth
09.1998:	Diplom Physik
	Diplomarbeit "Ordnungsphänomene in quaternären Borcarbiden"
09.1998-12.1998	wissenschaftlicher Mitarbeiter am Lehrstuhl Experimentalphysik V der Universität Bayreuth

Promotion

Seit 15.2.1999	Promotion am Institut für Physikalische Elektronik der Universität Stuttgart

Acknowledgement

It is a pleasure to thank the many people who made this thesis possible. Especially I would like to express my gratitude to ...

Prof. Jürgen H. Werner for accepting me at his institute, his continuous support, and providing excellent working conditions during my thesis,

Prof. Jörg Weber for kindly accepting to report on my thesis,

Dr. Ralf Bergmann for his continuous guidance and scientific supervision and the inspiration and enthusiasm he provided throughout my research work,

Dr. Markus Schubert for his constant encouragement and support and the introduction to the "secrets" of project management,

Dr. Uwe Rau for the fruitful work on the TQE and the many discussions and questions he knew the answers to,

Dr. Lars Oberbeck for the close and successful cooperation in the epitaxy-lab, the many long discussions about technology and defects, and for his encouragement and help during my thesis,

Titus Rinke for all his tips and tricks concerning solar cell processing and for sharing his technological knowledge,

Dr. Melanie Nerding from the University of Erlangen for the excellent cooperation, her accurate measurements, and the interesting discussions that were not confined to work issues,

Dr. Sergei Ostapenko and Dr. Igor Tarasov from the University of South Florida for the kind invitation to their institute and the introduction to photoluminescence,

Dr. Steffen Knack from the Technical University of Dresden for DLTS measurements and discussions,